NORTHWESTERN UNIVERSITY

Computational Electron Microscopy for the Characterization of
Soft, Hard, and Hybrid Materials

A DISSERTATION

SUBMITTED TO THE GRADUATE SCHOOL
IN PARTIAL FULFILLMENT OF THE REQUIREMENNTS

for the degree

DOCTOR OF PHILOSOPHY

Field of Materials Science and Engineering

By

Karl Hujsak

EVANSTON, ILLINOIS

March 2019

ABSTRACT

Connecting structure and function in nanoscale engineered materials and devices relies on the analysis of the fundamental arrangement of matter, frequently under dynamic conditions. The demand to image structures at fundamental length scales has touched inorganic materials, biology, and frequently hybrid hard/soft materials with unique phenomena driven by heterogeneous components. Electron microscopy has been at the core of imaging and interrogating structures at this scale for many decades. Improvements in hardware and digital control have pushed the boundaries on the information measurable from modern systems. Operating as an 'electron scattering' experiment the ability to push copious amounts of current into small volumes has exacerbated the sensitivity of many materials to radiative damage. Thus, developing new autonomous methods of imaging which rely on advanced computation or machine learning is playing a larger role in the reliable and high-speed imaging of next-generation materials. Such methods potentially allow an investigator to image materials dynamically in ways not previously possible, partly due to the reduction in area doses and partly due to drastic time-savings.

In Chapter 1, the major advances in electron microscopy over the last few years are highlighted, as well as outstanding challenges in the reliable characterization of dose sensitive materials. Novel methods based on a hybrid hardware-software approach are highlighted, as well as advances modeling the process of image formation for effective signal restoration. A high-level background to Compressive Sensing is offered, as well as practical discussions on the likelihood

of successful implementation in electron microscopy. Expanding on this, Chapter 2 discusses the practical implementation of a coupled hardware/software approach to general imaging of radiation sensitive materials, particularly where multiple measurements will be made. Chapter 3 further advances this topic by placing control of the microscope directly in the hands of an autonomous machine learning platform, which efficiently plans out the application of dose within the column for maximum information retrieval. The work shifts gears slightly in Chapter 4 for a discussion of a novel crystalline orientation mapping tool enabled by advances in image processing, as well as its potential as a non-destructive method for understanding complex defect structures. Finally, Chapter 5 will discuss future directions and potential expansions on the preliminary work discussed in this thesis. The consistent theme of this work is the practical application of statistical learning and computation to enable new ways of interrogating structures, particularly with an eye towards reducing the time or integrated electron dose for key information. In many cases, it will be shown that considerably superior methods are available with simple innovations for almost no cost, and the future of electron microscopy will likely be at the interface of hardware and software, as data management and acquisition increasingly become core to the technique.

ACKNOWLEDGMENTS

It would be improper to begin this section without acknowledging the continued and unwavering support I have received from thesis advisor, Professor Vinayak P. Dravid. Although I did not always deserve it, I am positive his dedication to his student's success is the major reason I have been able to complete the following work. He has consistently put the wellbeing of his students first and foremost, making one-on-one time a priority for all members of the group. And while I did not always realize it at the time, by pushing me outside my comfort zone I have grown more than I possibly could have imagined before starting at Northwestern. I am deeply indebted to him for accepting me into this group and supporting my myriad interests.

Next, I would like to acknowledge the generous support of my thesis committee, Professor Petford-Long, Professor Wolverton, and Dr. Doga Gursoy. I would also be remiss to fail to acknowledge Dr. Seungbum Hong who played a critical early role on my committee but has since left to pursue a successful career in Korea. It has been a privilege to share the last year of my Ph.D. as part of a larger project with Dr. Gursoy, Professor Aggelos Katsaggelos, and Professor Ollie Cossairt on the uncalibrated tomography problem. Their enthusiasm for imaging and signal processing is infectious and I enjoyed our spirited discussions. I will always appreciate how readily they welcomed my colleagues and I into the collaboration. They truly do a service to interdisciplinary research at Northwestern.

None of this work would have been possible without my colleagues Dr. Benjamin Myers, Eric Roth, and long-time friend Yue Li. Surely, without Yue's curiosity and dedication to the pursuit of truth I would never have dreamed to attempt these projects. I will always be grateful for her timely and on-point advice and criticism, especially as co-conspirators on much of this work. Many difficult periods during this thesis were overcome together, and I am very grateful for the strength we have developed in tandem.

Simply put, Dr. Myers and Mr. Roth are the best collaborators anyone could ever hope to work with. None of this work would have gotten off the literal drawing board without their collegial attitudes and willingness to get their hands dirty. They have truly been an inspiration to work with; they encompass a rare combination of work ethic, extreme intelligence, and friendly demeanor. I would strongly recommend any future Dravid group students who might read this work to seek out and heed their advice.

I would also like to acknowledge my collaborators at the Air Force Research Laboratory and Purdue University for welcoming me during my extended stay at Wright Patterson. I will always be especially grateful to Dr. Claretta Sullivan and Dr. Larry Drummy for welcoming me so kindly into RXAS. Dr. Krishnamurthy Mahalingam and Bob Wheeler are also owed thanks for spending their valuable time arranging instruments and training me. Without them I would not have accomplished half of these results. I'm also indebted to Dr. Jeff Simmons and the group of Professor Charlie Bouman, in particular Dilshan Godaliyadda, for helpful discussion.

In a similar vein I would also like to thank Dr. Bernhard Schaffer for lengthy discussions on the intricacies of Digital Micrograph. His friendliness and willingness to share information without reservation saved me much frustration. Dr. Joe Nabity was also essential, as he shared critical information regarding the modification of the NPGS lithography system on which Chapter 2 is based.

I was very lucky during my time at Northwestern to enjoy the friendship of many of my cohort and others from the greater community. They have made this time especially meaningful and I will carry many memories forward with me. In no particular order I'd like to thank Shawn Chen, Amit Kishan, Garrett Lau, Seyoung Cook, Karen DeRocher, Ha-Kyung Kwon, Gavin

Campbell, and Charlotte "you don't know me" Chen. Extra special thanks to Yue Li for putting up with them, and me, for all these years.

Finally, I would like to thank my family for putting me on this path by consistently supporting my interests in science from a very early age. Without their support during my formative years I may never have found myself completing this degree. Truly, much of the credit for this work must be given directly to then, especially since they invested the equivalent of several doctorates raising me.

Karl

December 2018

DEDICATION

This dissertation is dedicated to my parents, Jon and Colleen, for the love and support which put me on this path.

TABLE OF CONTENTS

LIST OF FIGURES

from a Gatan controlled EDAX EDS (1024 channels at 10 eV width) detector of the leftmost inset in image A. 10% of the pixels in the 80x80 image were collected with a one second dwell time per pixel, resulting in a total collection time of 23.6 minutes vs. a conventional full SI acquisition of 2.7 hours. An initial 1% of the pixels was collected randomly. C. Reconstructed discretized spectrum image of the elemental distribution of iron from the scan mask in B. D. Scanning mask collected from the rightmost inset in image A, again tracking the Fe Kα with an 80x80 grid and 10% sampling. E. Reconstructed discretized spectrum image from the mask sampled in D. F. Representative spectrum collected with a 30 second dwell time showing the strong Fe K$_α$ peak that was used for the mapping (2048 channels at 10 eV width)...................................... 153

LIST OF TABLES

CHAPTER 1: INTRODUCTION

1.1 Philosophy and Approach

Materials characterization remains an essential component in the engineering and understanding of larger scale devices and processes. Rapid advances in the quality of hardware and the digitization of most imaging and measuring devices has opened the opportunity for small scale investigators to design new methods of interacting with and probing materials in dynamic environments. To take advantage of this chance to design custom instruments and operations has required the integration of a diverse set of colleagues, from computer science and electrical engineering to more traditional mathematics and statistics. Concepts from operations theory are increasingly being leveraged to design statistical learning methods which can adapt and control experiments on the fly. The fact that phenomena which take place at small length scales often occur at small temporal scales will increasingly require the use of intelligent sampling methods which avoid 'blind' recording of phenomena by a single user.

The goal of this introduction chapter is twofold: first, to give non-imaging experts an introduction to the strengths and challenges of modern electron microscopy and materials characterization, and second, to give traditional microscopists the major takeaways from paradigm challenging concepts from mathematics, particularly Compressive Sensing. Thus, on occasion, mathematical rigor in the description of the electron column or various optimization methods has been substituted for

synthesizing the major points for an application minded audience. Such rigor will be reintroduced in the following chapters when relevant for the major developments and proposals in this thesis.

1.2   A General Introduction to Modern Electron Microscopy

Electron microscopes have emerged as the de-facto imaging technique for the interrogation and understanding of nanoscale structure. Spanning nearly all materials research areas, such as energy storage, energy conversion, semiconductors, and therapeutics, the electron microscope a core tool for the investigation of the connection between fundamental structure and function[1-6]. Having achieved resolution with picometer precision, they surpass the best optical microscopes by several orders of magnitude due to the sub-atomic wavelength of the electron[7, 8]. This resolution advantage comes with several caveats for the nature of the samples; they must be physically and chemically stable in vacuum, liquid or gas and processable into a thin electron transparent film without damage (with the exception of surface sensitive techniques), and resistant to the electron beam[7]. For many materials which exist fundamentally with these properties (nanomaterials, etc.) these criteria are immediately satisfied, but others can be quite challenging to prepare and investigate reliably.
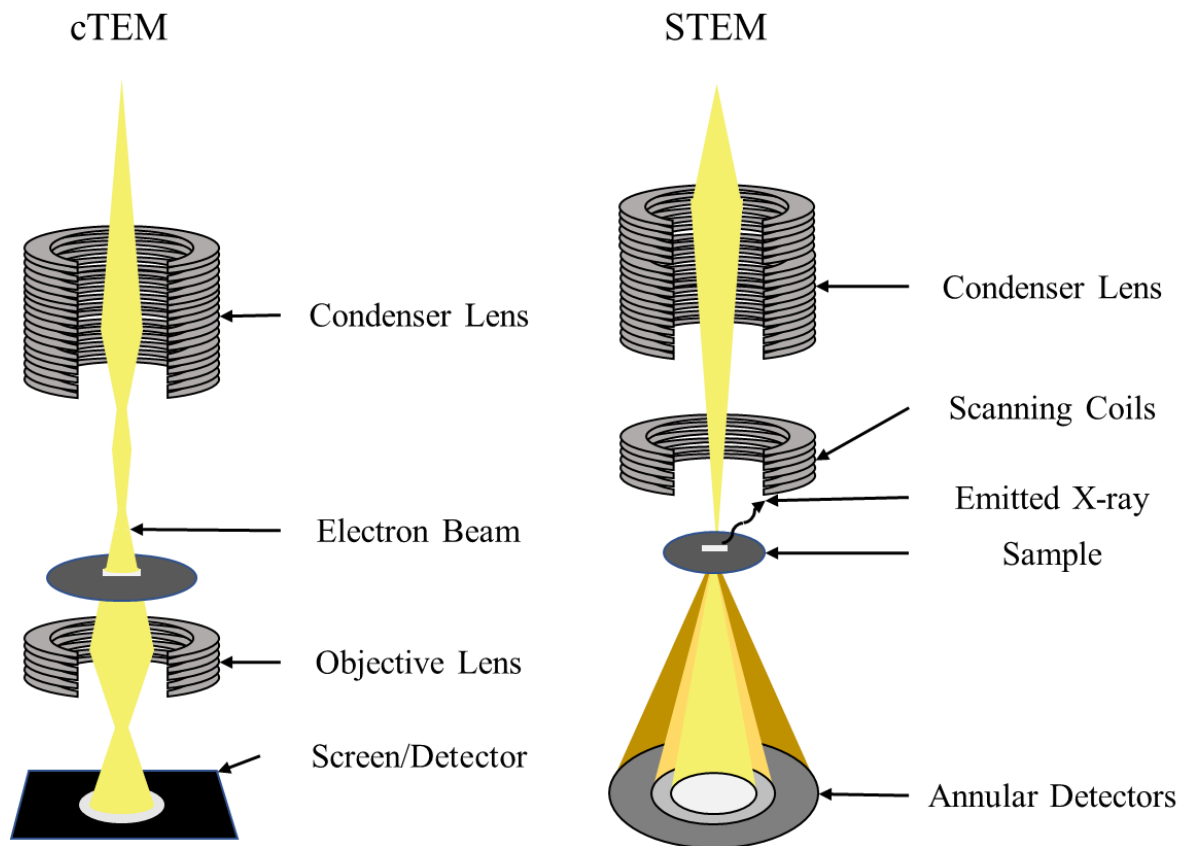
Figure 1.1 A comparison between the two most common operating modes for electron microscopes, parallel probe conventional Transmission Electron Microscopy and Focused/Scanning Transmission Electron Microscopy.

There are two primary operation modes for imaging with an electron microscope: parallel probe or convergent probe. In both modes a source of electrons is accelerated at high voltage (5-300kV) and focused on to a specimen using electromagnetic lenses. In conventional Transmission Electron Microscopy (cTEM), a parallel electron micro- or nano-probe illuminates a small area of

the sample and a pixelated post-specimen detector collects a certain population of transmitted or scattered electrons to form an image. The detector can be placed either in either the imaging or diffraction plane depending on the activation of the post-specimen lenses. Typically, apertures will be placed in the diffraction plane to select electrons which have been scattered by specific crystal planes or the unmodified transmitted electrons. These two aperture positions produce dark field and bright field imaging conditions, respectively. Electrons reaching the detector from either of these two conditions have both amplitude and phase, but detectors are generally only sensitive to the incident intensity. Interpreting cTEM images at high resolution generally requires extensive simulations to understand the frequent contrast reversals that can occur due to this phase component. Some electrons may be emitted back from the specimen valence electrons or reflected primary beam electrons, producing secondary and backscattered electron images.

In Scanning Transmission Electron Microscopy (STEM) a convergent nano- or pico-scale probe is focused on the sample and rastered to form an image[9, 10]. The electrons passing through the specimen, or those backscattered, can be collected at each probe position and integrated on a photomultiplier tube (PMT) to record images. The transmitted electrons in STEM are collected using a series of annular detectors which are segmented to produce different signals[10]. The inner, or axial, detector produces bright field images using those electrons which do not undergo significant scattering. On the other extreme, the High Angle Annular Dark field detector (HAADF) integrates electrons which have been scattered to large angles (Rutherford Scattering)[11]. In HAADF the phase component can be shown to integrate out, resulting in an incoherent imaging

mode where the contrast is pseudo-linearly related to mass[12]. This results in HAADF's more common name, 'Z-contrast imaging', and its simple interpretation compared to cTEM has made it a popular choice in the research community. Since no post-specimen lenses are required to form the image in STEM, it suffers less from the imperfect focusing due to chromatic aberration that can occur in cTEM in thick specimens due to the wide range of energy losses from plural scattering.

While the elastic scattering is generally used for imaging, inelastically scattered electrons carry a significant amount of information about elements present, bonding states, and electronic configurations. Two primary methods will be considered in this thesis: analyzing the energy lost by electrons as they pass through the specimen and the emission of photons due to decay from ionization by the incident electron beam. Both methods are primarily used in STEM mode due to the ability to localize the effect on the sample and produce spatial maps[13].

Incident
Ionizing
Radiation

X-Ray
Emission

K Shell

L Shell

M Shell

Inelastic Scattering of
Incident Electron
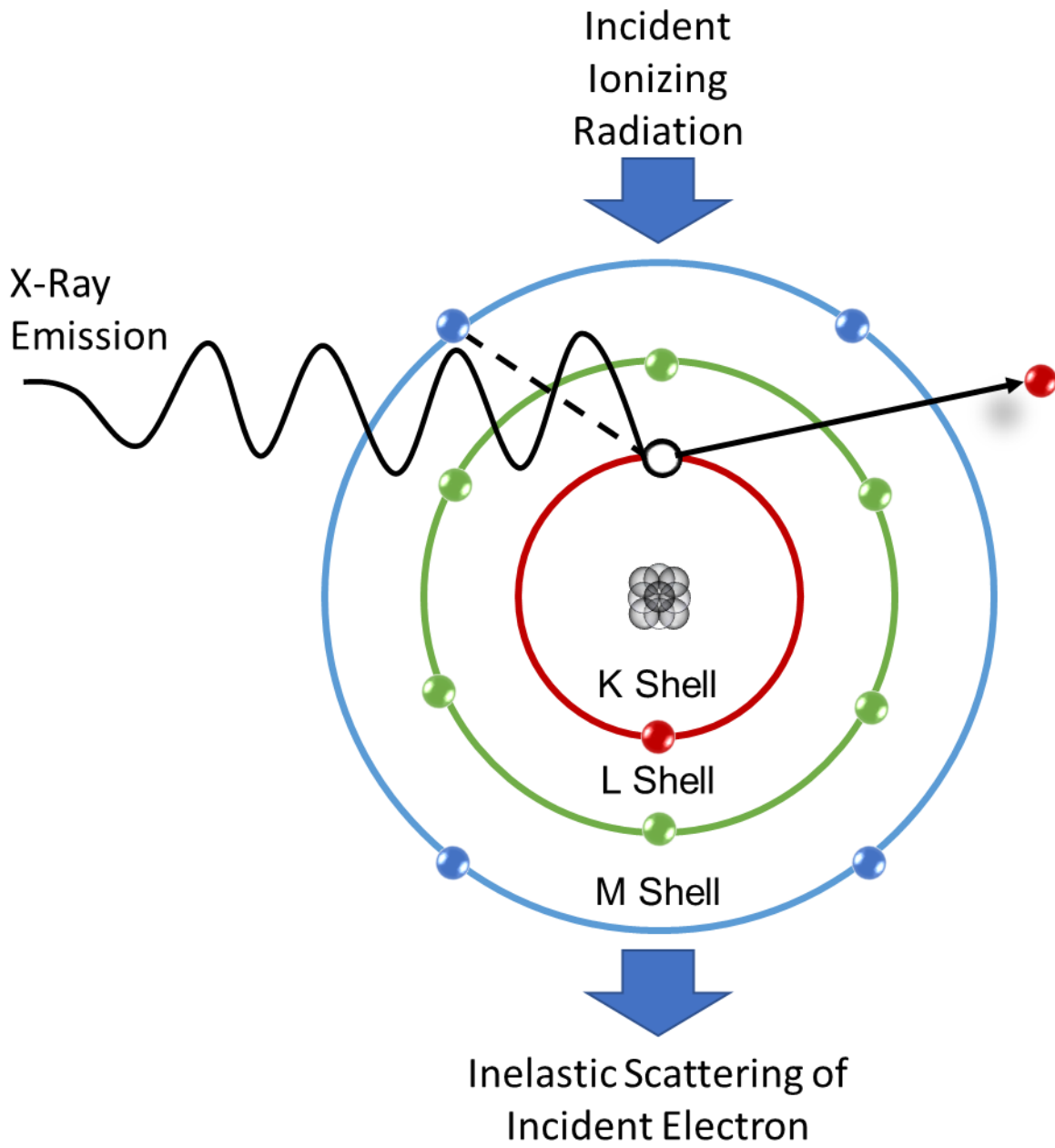
Figure 1.2 Illustration demonstrating the mechanism by which an inelastic scattering event can produce an analytical signal inside the electron microscope. Any high energy electron from the incident beam may participate in an inelastic scattering event that may ionize an inner shell electron. The energy an incident electron loses during this scattering event can be recorded post-specimen, giving EELS spectra. The decay of a valence electron to fill the ionized core-position may result in a characteristic X-ray emission which may be detected by an EDS spectrometer positioned strategically.

Electron Energy Loss Spectroscopy (EELS) sorts the electrons that pass through the specimen by their energies using a magnetic prism. A typical EELS spectrum has a large peak at zero energy, referred to as the zero-loss peak (ZLP), composed of those electrons which have passed through the sample without losing energy. Next, the low-loss region (up to 40 eV beyond) contains plasmon peaks, which results from the free oscillation of electrons in the material. Lastly, a core-loss region contains edges, or 'bumps', corresponding to characteristic energy losses from the ionization of particular core electrons in the atoms of the sample. These edges can be directly connected to the elemental identity of the material at the beam location, and even used to infer the chemical structure[13]. The very long tail of the plasmon peaks results in a considerable background signal which can often obscure the weak core-loss edges at low signal-to-noise ratios. The subtraction of this background is therefore essential and is usually modeled using a power law approximation [14]. Plural scattering can also often obscure core-loss edges, so great pains are often

taken to produce thin specimens. Single point spectra, line-scans, and even volumetric maps are routinely achievable on modern instruments.
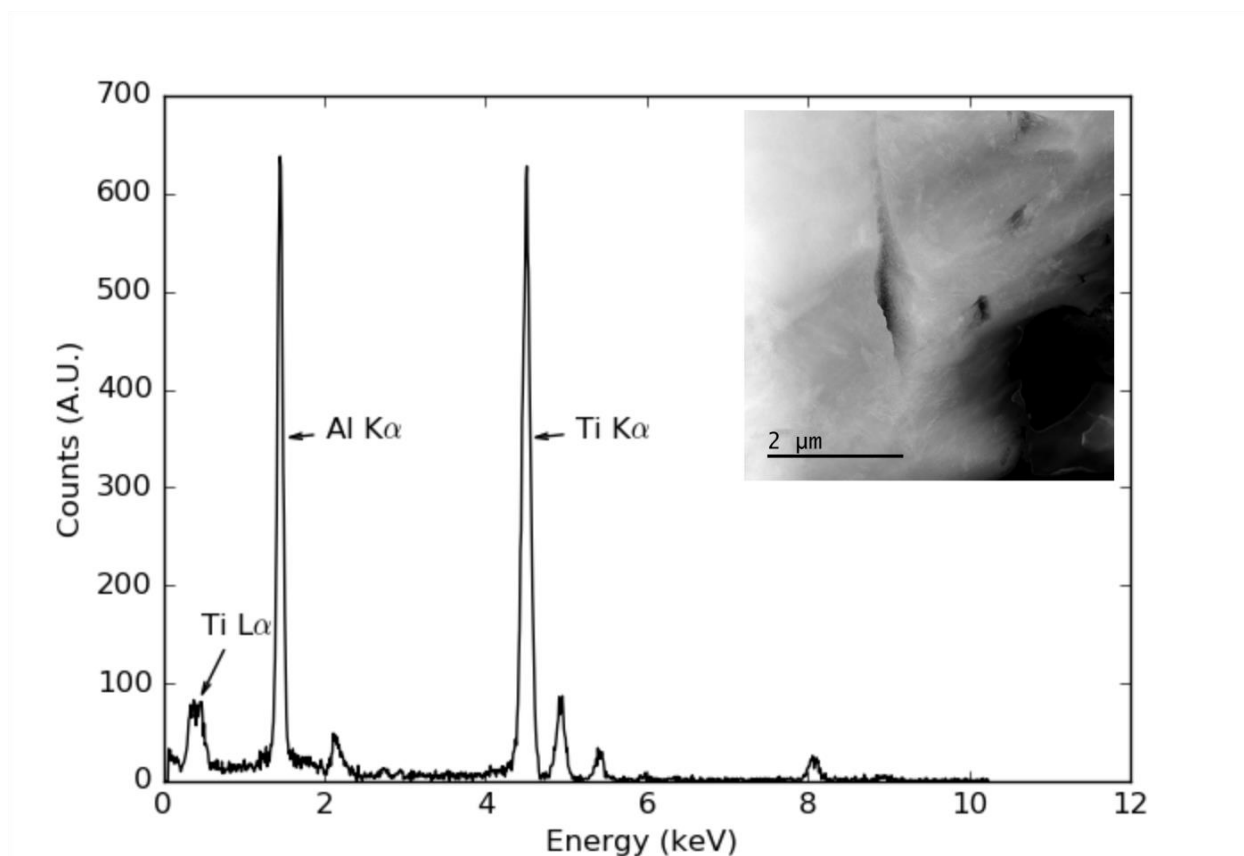
Figure 1.3 Plot of a typical EDS spectrum from a high resolution STEM on a metallic specimen. A region with a precipitate in a Titanium-Aluminum alloy was investigated using an FEI Titan aberration corrected STEM with a single SDD EDS detector. The total dwell time was thirty seconds, giving an appreciable signal-to-noise ratio and easily allows us to distinguish the

characteristic peaks for the two elenents. The inset shows a HAADF image of the region of interest, where a darker precipitate can be seen in the center of the frame. Note that this dwell time is consideravly larger than can be maintained on radiation sensitive materials and can preclude a high pixel density spectral map.

After an ionization event driven by the incident electron beam, a valence electron may decay to occupy the empty core position. This energy produced by this decay results in a characteristic X-ray or an Auger electron, the former which can be recorded by an a strategically positioned X-ray spectrometer in Energy Dispersive X-ray Spectrometry (EDS)[15, 16]. The highly precise nature of the electron decay event results in sharp peaks in an X-ray spectrum which can be connected to the presence of an element. Since most STEM/TEM samples are thin enough to be electron transparent, there is little Brehmsstrahlung radiation resulting in very high signal-to-background spectra[17]. In addition, since X-rays interact with matter much more weakly than electrons, EDS is typically less sensitive to specimen thickness than EELS. However, the poorer energy resolution of EDS compared to EELS precludes the interpretation of fine structure, and the limited accessible area near the specimen results in a very small collection area. This can make EDS acquisitions extremely inefficient, as the X-rays are emitted uniformly in all directions and the detector intercepts a very small segment.
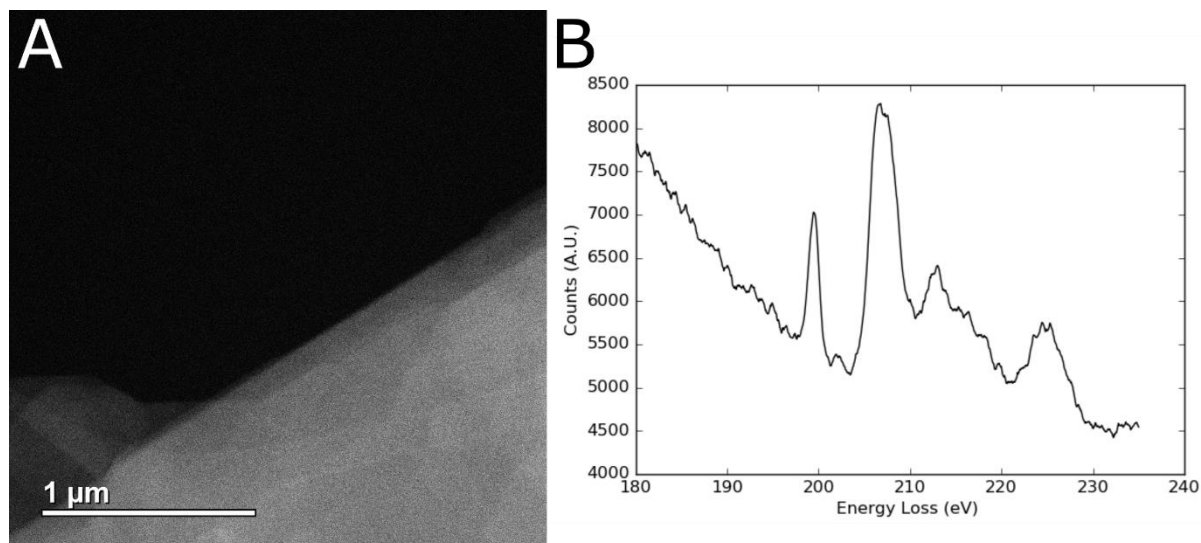
Figure 1.4 (A) HAADF image of a multi-layered Boron Nitride flake from a Hitachi HD2300A STEM. The darker area is a vacuum region with no specimen, resulting in no contrast in the dark field image. (B) Typical Boron edge from a Gatan Enfina EELS spectrometer with a five second exposure further processed by a moving window average. Note the complicated structure of the edge, with multiple interspersed peaks which can be altered by change in the bonding configuration of the element. While this potentially gives powerful information about the state of the material, it can make fitting and quantification difficult, especially due to the very large pseudo-power law tail from the plasmons.

These tradeoffs mean that EELS and EDS are typically used in tandem to provide complementary information. However, the large background in EELS and the dose inefficient nature of EDS mean that most analytical maps at high resolutions require large incident electron doses [18]. Typical doses of 10^5-10^6 e$^-$/ A^2 prevent the imaging of many interesting specimens, such as hybrid soft-hard materials, porous frameworks, catalytic materials, or *in-situ* phenomena (which will be discussed later)[19-22].

Although traditional EM has involved the recording of two-dimensional images, electron tomography has seen a renaissance as STEM has allowed for the suppression of diffraction contrast and the imaging of thicker specimens[23, 24]. Acquiring a series of images at multiple angles yields sufficient information to solve for the three-dimensional structure of a sample. Atomic resolution tomograms have recently been achieved [25]. However, the limited available tilting range due to the risk of colliding with the pole-pieces of the objective lens and the increase of sample thickness at high tilts generally introduces a considerable number of artifacts [26]. The need for high sample stability over such a prolonged imaging experiment can be even more challenging, as mass flux (which will be discussed later) and sample motion can preclude a consistent solution[27]. Time-lapsed video shares a similar set of problems with tomography, in that the prolonged imaging of a specimen over multiple exposures results in considerable risk of damage without the advantage of dose fractionization[28].

Driving the interest in time-lapsed observations, advances in fabricating enclosed micro-or nano-volumes of liquids and gasses through advanced lithographic processes has allowed for the observation of a wide variety of phenomena. While electron microscopes are typically operated in high vacuum to reduce pre-specimen scattering in the electron beam, tightly enclosed volumes can be fabricated with thin electron transparent windows to allow for the formation of a high-quality incident beam on a liquid or gaseous sample.

As will be discussed in the following section, a consistent challenge at the frontier of modern electron microscopy is the consistent and repeated observation of non-traditional structures and samples without inducing untoward sample alteration.

1.2.1   Limitations due to Radiative Damage

The risk of ultrastructural damage under electron illumination is a challenge that must be acknowledged and minimized when investigating any sample. Bombarding a specimen with relativistic electrons at high current densities can quickly modify a stable specimen or move a dynamic process out of equilibrium[29]. As the likelihood of observing the desired elastic or inelastic scattering event on a detector or spectrometer is related to the incident beam current, there exists a trade-off between structural modification and signal-to-noise ratios[30]. This has been long

realized in the biological sciences community, where the insulating and fluctuation driven nature of bonding in soft samples makes them highly susceptible to ionization and inelastically driven damage. As the contrast of these samples is due to slight shifts in phase (weak phase object approximation), considerable work has been dedicated to optimizing imaging conditions to maximize the ratio of detectable elastic scattering to damaging inelastic events[30, 31].

Next-generation hybrid soft/hard materials in energy, therapeutics and aerospace are increasingly sharing these weak fluctuation driven properties. Materials which derive novel functionality by an interlinked traditional metallic or ceramic ('hard material') component with a polymeric or biological component ("soft material") have become a major area of interest as bottom-up chemical and directed assembly methods have improved[32]. Metal/Covalent organic framework structures (MOFs/COFs), in which a metal atom or cluster is coordinated within a larger organic framework, have become a major topic in energy storage, catalysis, and ion separation[33]. It has been shown that structural defects in MOF structures can increase their ability to store/transfer hydrogen for high capacity storage by opening new channels and pores[34]. A direct inspection of the defect structure at high resolution is needed to quantify the relationship between lattice defects and hydrogen transport. As will be discussed in the following section, the fluctuation driven bonding of the organic component makes it extremely difficult to image with electron microscopes without introducing additional defects due to ionization. Intelligently designed pseudo-lattices of metallic clusters has also been achieved with the help of programmed DNA interactions[35, 36]. Such systems have interest for their novel coupled plasmonic and sensing properties, as periodic

materials at this scale have not previously been synthesizable without the tightly controlled bonding of DNA structures[37, 38]. DNA itself is easily modified by ionizing radiation, which can quickly cause structural collapse[38]. Silica embedding and other sample preservation methods can result in sample modification, making it difficult to observe the native structure. Hybrid materials are also seeing attention for next-generation composite aerospace materials, where the soft component is chemically bonded to the hard filler at the nanoscale level. As opposed to mixing separately prepared components, such grafted nanoconstructs have tightly controllable filling ratios and suffer from none of the self-segregation that can occur with other macro-scale mixed composites[39]. By maximizing the interface between the soft and hard component they also may achieve higher strengths at lower weights, improving the efficiency of aerospace systems. Imaging the graft/particle interface and particle/particle interactions is complicated by the need to apply significant electron currents in order to resolve the weakly scattering soft component next to a highly scattering 'bright' hard system, which can often result in ionization of the graft interface and structural modification.

Advances in hardware have afforded an order of magnitude higher available beam current at probe sizes smaller than an atom[40]. Save for 'work-horse' specimens such as Strontium Titanate (STO), these higher currents have only further complicated the observation of soft and hybrid materials for reasons other than the quality of the microscope[41]. The choice of operating voltage and beam current must be optimized to minimize the effect of ionization damage and sputtering, particularly for time-lapse or tomographic imaging, as mass loss during imaging completely removes the

chance for a consistent structural solution. In addition, high beam currents can drive the deposition of organic contaminants in the microscope (mass addition). Despite the high standards for vacuum purity in most microscopes, the 'dirty' liquid phase processing of most materials that is necessary for scale up and commercialization provides a large source for contamination that frequently cannot be removed without destroying the specimen of interest[42].

As discussed above, there are two major sources of damage when observing a material at high integrated doses. Firstly, the ionization of a sample atom by an inelastic scattering event with an incident electron. Local structure plays a key role in the downstream effect of inelastic scattering, as in conducting materials an additional electron can be donated quickly. In insulating materials, such as biological specimens, an ionization event is much more likely to result in bond breakage and mass diffusion at room temperature. The application of imaging techniques which rely on inelastic scattering is therefore much more challenging on soft and insulating materials. Conducting materials are still subject to knock-on damage, where high angle elastic scattering of high speed incident electrons results in atomic displacement. Such knock-on damage can occur at both the surface and the bulk of the specimen. If on the surface, considerable material thinning from atom ejection can result at high accelerating voltages, though random surface diffusion of adaptors may occur at considerably lower activation energies[30, 43]. In the bulk, atoms may be displaced to interstitial sites or vacancies as a result of an elastic scattering event[44]. As opposed to ionization which is current driven, knock-on requires a critical activation energy and can be controlled by the beam accelerating voltage[45].

Both damage mechanisms affect that overall beam conditions under which images can be collected. In landmark work, Glaeser examined the effect of low-flux electron beams on the achievable information and resolution in electron micrographs of biological specimens[46]. The inherent image contrast is defined as the difference in intensity between two arbitrary points normalized by the local average in intensity (background component). Statistical fluctuation in the illumination due to the quantized nature of electron charge at low fluxes and the associated read-out noise of the detectors frequently obscure features with weak contrast. It is common to approximate the arrival rates of electrons on to a detector element as a Poisson process, characterized by a mean arrival rate λ. Thus, the statistical fluctuation in the arrival of electrons on an arbitrary area of the sample is $\sqrt{\lambda}$ (square root of the variance of a Poisson process). Glaeser approximated the arrival rate of the process as related to the current density through the specimen, j; the resolution of the detector, d^2, the exposure time, t; and the collection efficiency of the post-specimen lenses and apertures, f[46]. For STEM, the collection efficiency is the fraction of post-specimen electrons that fall on any annulus, and in TEM it's the number of electrons which are accepted by the post-specimen apertures and lenses. Thus, the contrast ($\Delta n/n$) purely due to statistical fluctuations, which must be exceeded by the inherent contrast of the object to be detectable, can be written as follows:

$$\frac{\Delta n}{n} = \frac{1}{\sqrt{jfd^2t}} \tag{1.1}$$

It was further showed by Howie that the resolution at a radiative Dose, D, and detector quantum efficiency, η, could be defined as:

$$d = \frac{K}{C\sqrt{\eta fD}} \tag{1.2}$$

Where K is the signal-to-noise ratio, typically chosen to be 5 to satisfy the Rose criterion, and C is the contrast[47-49]. The challenge for electron imaging is this inverse relationship between the resolution and the required electron dose. A dose-limited resolution, DLR, can be defined as the maximum achievable resolution at a particular detector set up, contrast, and signal-to-noise ratio before damage can occur. For HAADF imaging at high scattering angles, both the contrast and the collection efficiency depend on the elastic scattering cross section of the material normalized by the support cross section. Thus, the dose limiting resolution (DLR), or the maximum resolution achievable at an accelerating voltage can be written as the square root of the ratio of the elastic scattering cross section (σ_D) and the damage cross section (σ_S):

$$DLR = \sqrt{\frac{\sigma_D}{\sigma_S}} \tag{1.3}$$

Channeling effects in crystalline specimens often require extensive simulations to define an optimal imaging condition to achieve high resolution.

LogLog Plot of Dose vs. Resolution

Damage Regime

DLR

Noise Regime

Resolution (Å)
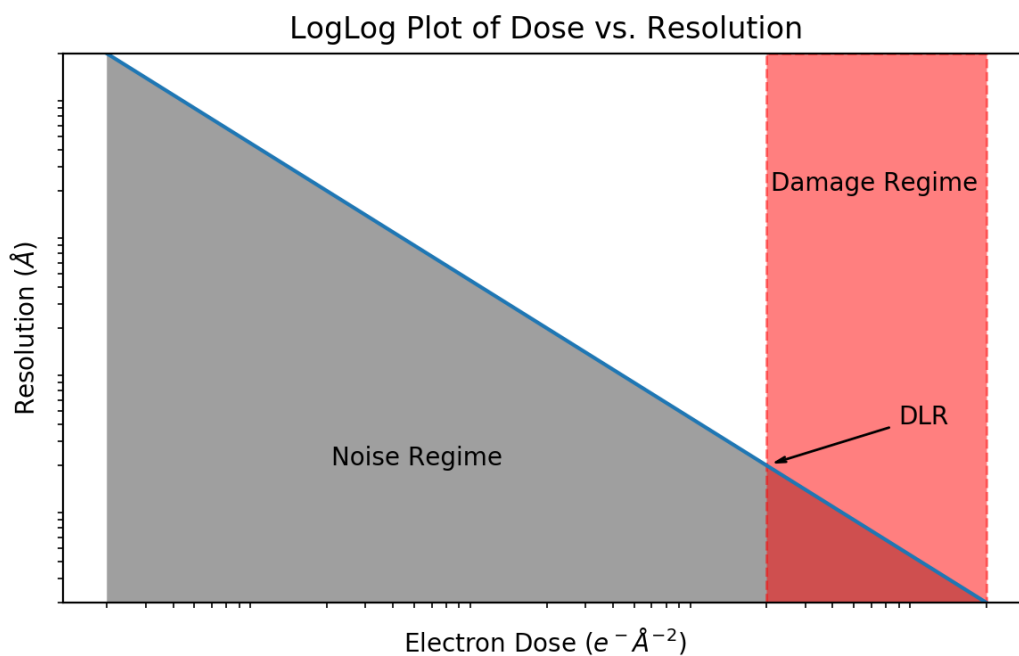
Electron Dose ($e^- Å^{-2}$)

Figure 1.5 Plot of the relationship between the quality of a final image, in terms of signal-to-noise ratio and resolution, and the requisite Electron Dose. Equation 1.2 is plotted in blue showing the crossover between a noise-dominated image (k<5) and a resolvable structure. On the right, the critical area for damage is highlighted in red at which the structure of the sample is altered during the integration of one image. The highest achievable resolution, the DLR, is annotated as the crossover of the blue line from Equation 1.2 and the Damage regime.

The impact of the incident radiation on a specimen of interest has up to this point been described strictly in terms of a total integrated 'dose', as a product of the beam intensity and the exposure time. It has been noted that the instantaneous beam intensity, or current density, also plays a unique role in the evolution of specimen damage. The development of a specimen charge due to the injection of electrons or wide emission of secondaries may cause sample motion due to the buildup of an internal field and consequent image blurring. This charging effect has been shown to be suppressed by reducing the total beam intensity below some material dependent threshold[50, 51]. Reducing the beam intensity may also reduce the rise in local temperature from energy deposition[52]. Conflicting evidence on the importance of the beam current density on the stability of organic and biological materials exists, and likely remains a topic of future work in the field[53, 54].

The fact that these challenges are not unique to electron microscopy, and in fact are shared by many other characterization methods relying on a radiative probe, means that much cross-disciplinary work is possible[55].

1.2.2 Advances in Hardware

When Ruska first envisioned the electron microscope, he substituted the wavelength of the electron in the constitutive equations for the resolution of optical microscopes[56]. This extremely high

resolution remained unchallenged until Scherzer noted that the symmetry of the spherical electromagnetic lenses would result in resolution limiting aberrations[57]. These aberrations are referred to as geometric, which result directly from the spherical shape of the lenses. Parasitic aberrations due to the imperfect manufacture of lenses, and the chromatic aberration due to imperfect focusing of electrons with slightly different wavelengths must also be accounted for[58]. By altering the phase of the electrons, these change the trajectory of the particle passing through the microscope and fundamentally limit resolution[59].

For TEM, the critical image forming lenses immerse the specimen (objective lens), and therefore must contend with chromatic aberration due to inelastic scattering events and imperfect focusing. In STEM, spherical and other aberrations make it difficult to perfectly focus all electrons that pass into the condenser system. This results in a trade-off between the intensity of the probe and the resolution, making it difficult to achieve high signal-to-noise ratio images at very small probe sizes. Improvements to electron sources for higher beam coherency and better power sources to expand the temporal coherence envelope in the transfer function have improved the capabilities of systems which have remained fundamentally limited by aberrations.

Scherzer initially proposed that an aberration correction system could be produced with non-rotationally symmetric multi-pole lenses[57, 60]. Critical work in the field in the early 1990s, more than fifty years later, made aberration correction a practical reality[61, 62]. For STEM, such correctors have allowed for the use of very large beam convergence angles at small probe sizes, dramatically

increasing available beam currents at high resolutions. Steady commercialization has democratized aberration correction outside of specialized national labs into the hands of universities and individual research groups.

Paralleling improvements in electron lensing, the detection of electrons has also seen a rapid reinvention. Prior to the 1980s, virtually all electron images were collected on silver halide gel film, such as the KODAK EM Film series. The ionization of the halide due to an inelastic scattering event with an electron produces silver which can be post-developed into an image. The grains themselves were typically less than one micrometer giving high resolution. However, the nonlinear response of the film due to ionization and the limited dynamic range (ionization is a one-shot process) required complicated multi-layer processing and post-exposure development. Developing film is also a very low-throughput technique, and the inability to ensure a good image on the microscope could be a major source of frustration.

Charge-coupled devices (CCD) offered a solution due to their real-time nature, high sensitivity, linear range, and high dynamic range[63-66]. A CCD operates by dividing a surface into an array of 'buckets' which can store multiple ionization events in a local capacitor. This charge is then transferred column by column into an output amplifier until all the charge is read out into a digital storage device.

Radiation damage was a consistent problem for CCDs directly exposed to the electron beam, so virtually all modern cameras employ a scintillator coupled to the CCD by a fiber optic cable[67].

The scintillation layer converted the incident electrons into photons which could be detected by the CCD without significant radiation damage. The introduction of the scintillator layer introduced the possibility of multiple scattering events which increased the point-spread-function of the camera. Thinning the scintillation layer was also not feasible due to the quantum efficiency of the cameras, which resulted in some photons being lost[66]. In typical 10-20 micron scintillation layers, the electron scattering in the scintillator broadens the detection event to several times the pixel size of the CCD, necessitating demagnification between the scintillator and the CCD[68]. Despite these challenges, the high-throughput nature of CCD imaging and ability to directly perform digital image processing on-the-fly made them the de-facto choice for general purpose imaging.

Radiation hardened CMOS cameras share none of these drawbacks, particularly due to the removal of either the lens-coupled or fiber-coupled scintillator layer[69]. As the active detection element in a CMOS layer is only present in the top film, additional scattering into the bulk of the detector produces significantly less stray signal than in the scintillator layer of traditional cameras[70]. Each pixel in the final CMOS cameras is equipped with its own read electronics meaning that significant frame-rates up to and beyond hundreds of frames per second with manageable read-noise is possible. The opportunity to operate in a 'counting' mode in which each electron incident on a detector operating at high speed is digitized can further increase the effective Discrete Quantum Efficiency (DQE) of the camera[71].

Analytical electron microscopy has also benefitted from improved detector technology, where extremely large area EDS detectors and high sensitivity 4K CMOS EELS cameras are now commercially available[72]. In combination with monochromators and aberration correctors such detectors can resolve molecular level fine structure[73].

1.2.3   New Developments in Software

Electron microscopes remain expensive investments, and each new generation can be expected to be a multi-million-dollar investment. The increasing digitization of microscope control and detectors has increased the possibility to creatively leverage advances in software to improve their usability or develop entirely new techniques. While the scope of the field is wide, only a few of the most relevant developments for the purposes of this thesis will be considered.

Surprisingly, if one were to compact all the sample area characterized by electron microscopes since their invention into one space, it would occupy less than a millimeter cubed[74]. New CMOS cameras discussed in the last section (Gatan K3 Camera) can produce 24.437 Petabytes of data in a single day, orders of magnitude more than previous systems. To put this in perspective, this is more data than all of Facebook processed globally on an average day in 2012[75]. It should be noted that this data flow is not an outlier, Cryo-Electron Microscopy labs commonly run these systems

24/7. The challenge for modern electron microcopy is to increase the amount of useful information about samples while managing this deluge of data.

Two schools of thought have emerged:

1. Improve the interpretability of large volumes of raw data
2. Prioritize collection of reduced data for simpler interpretation

We will highlight several examples of implementations based around these ideas, which is by no means meant to be an exhaustive list. Examples have been selected based around novelty, follow-on work, relevance for the work in this thesis, or wide acceptance.

Among these, the use of Model-Based methods has drawn much attention[76]. The relatively simple forward model for the formation of contrast in incoherent imaging modes, such as HAADF, enables the computation of data likelihood with limited time complexity[77]. Considerable work in the development of Model Based Iterative Reconstruction techniques in the context of Computer Tomography for the medical field, have been translated to the domain of Electron Microscopy[78]. By combining a physical model for the formation of image contrast, a reliable three-dimensional volume can be constructed from a raw tilt series. Instead of solving for the volume in terms of an arbitrary intensity value (typically nm^{-1}), MBIR methods can solve for the scattering or attenuation coefficients. With the use of an effective prior, these methods have been used to characterize interfaces between materials of wildly different elastic scattering coefficients, which would normally be completely overwhelmed by artifacts from the high scattering region[79].
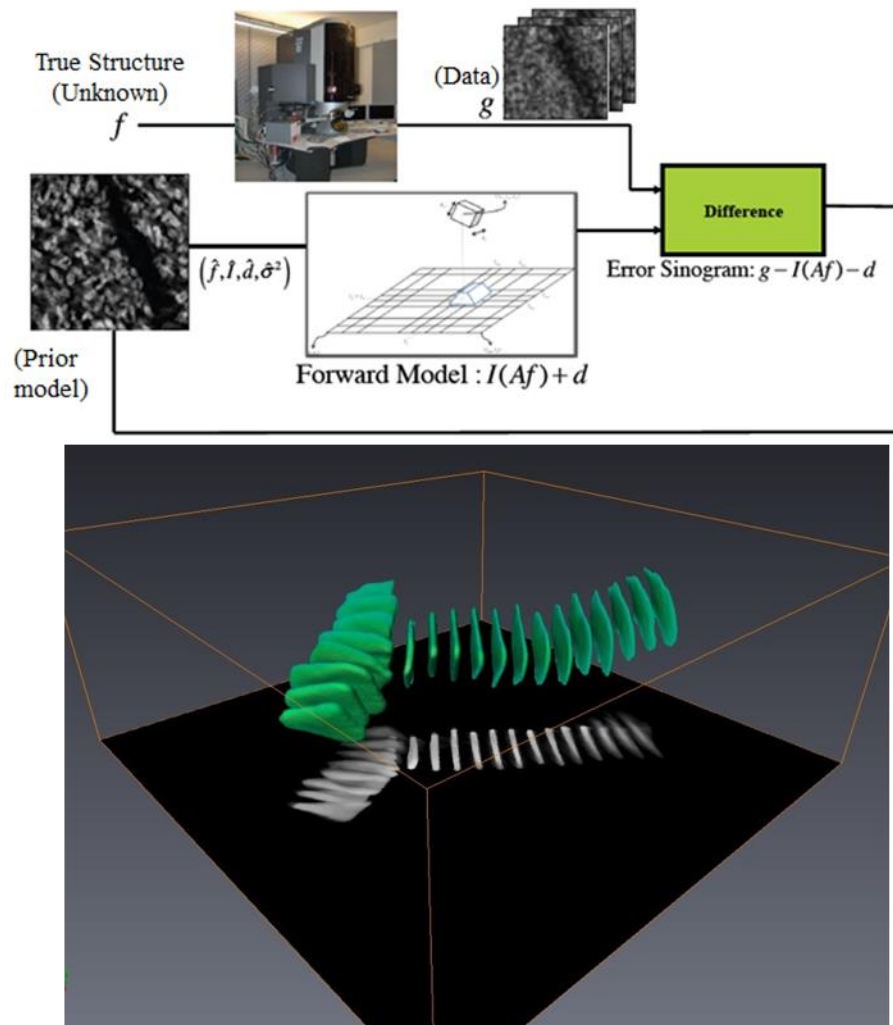
Figure 1.6 Top: Workflow describing the Model-Based iterative process for Electron Microscopy. A tilt series from a three-dimensional unknown sample, f, is collected on a microscope and stored as a series of tilted two-dimensional images, g. This series is inverted into

a three-dimensional volume and constraints on the sample given material insight is applied. A simulated tilt series is then calculated for this approximate volume using an accurate physical model for image formation in the electron microscope. The error between the simulated tilt series and the actual, g, is then used to optimize the structure. This model directly accounts for noise and other instrument imperfections, allowing lower dose or further restricted angular field of view (FOV) acquisitions to still be reconstructed accurately. **Bottom:** MBIR reconstruction of a HAADF tilt series of a resin embedded DNA-linked gold nanoprism structure. Sample courtesy of Jinsong Wu.

Methods for correcting for artifacts in high volume rate images from electron microscopes have been developed as the desire to image faster for longer time periods has grown. RevSTEM is one incarnation of this topic, in which several rotated high-speed images of a specimen are recorded[80]. Nonlinearities in the scanning coils, primarily caused by eddy currents, and sample drift introduce many artifacts which preclude the alignment of a series of images to interpret dynamic phenomena such as crystal growth/evolution[81]. The multiple quick views with regards to a semi-constant drift vector give sufficient information to solve for a transformation to bring all images on to a common coordinate frame. Such a method is only possible due to the combination of a custom acquisition method which can be implemented on a digitally controlled microscope.

It is frequently much more difficult (and sometimes impossible due to the DLR) to produce high quality information about a sample than a large volume of noisy/poor quality data. Increasingly, investigators are making use of a few high-quality image samples to infer high resolution structures from poor, noisy, and low-resolution images[82]. Such multi-resolution techniques attempt to use the few high-resolution examples as an effective prior to solve for a super-resolution version of the low-resolution data. In some cases, up to 4x improvement in the resolution is possible from a small library of high-resolution image patches[83]. Such methods have not explored the possibility of hybrid low/high resolution recording within one frame using dwell time as a Bernoulli random variable. In addition, the possibility of using high resolution, more easily achievable HAADF images as priors for more difficult to obtain spectral images should not be understated. Although no experimental system has been developed to take advantage of the results, it's expected that continued progress in the super-resolution task from other fields may further increase the practicality of this method for electron microscopes.

1.3   Compressive Sensing

In this chapter I will attempt to provide a *microscopist's* introduction to Compressive Sensing (CS) by providing the key context that led to its formulation and the important take-aways for its application. Although in this thesis no compressive sensing schemes will be demonstrated, it's

important to clarify the difference between a CS acquisition and a more general under-sampled imaging technique, especially due to some perennial mislabeling in the literature. Originally formulated between 2007/2008, compressive sensing entered the stage when the ability to store and transmit data was quickly becoming eclipsed by the rate of information generation[84]. There was a pressing need to reduce the number of bits required to transmit data from sensors to processing centers without losing information[85].

In CS we will be concerned with the solution to a set of linear equations:

$$y = Hx + \epsilon \tag{1.4}$$

Where $x \in \mathbb{R}^P$ is an arbitrary vector to be acquired, $y \in \mathbb{R}^Q$ is a vector of acquired values, and $\epsilon \in \mathbb{R}^Q$ is a noise vector. $H \in \mathbb{R}^{QxP}$ is a sensing matrix which describes the physical process of acquiring the signal and storing it in some Q dimensional vector. In the case of a TEM, H describes the collection of the electron amplitude incident on a camera pixel and its conversion into a digital value. For STEM, H represents the conversion of scattered or transmitted electrons as the beam rasters onto the photomultiplier tube and into a digital value. In both cases, P=Q and H is a square matrix with all zeros except for on the diagonals (Equation 1.5).

$$H = \begin{pmatrix} 1 & \ldots & 0 \\ \vdots & \ddots & \vdots \\ 0 & \cdots & 1 \end{pmatrix} \tag{1.5}$$

Performing matrix multiplication between H and x effectively sifts out each value from x and passes it directly into a corresponding space in y. This produces an equivalent copy of x stored in y. In TEM, this matrix multiplication occurs simultaneously across all elements in x, as the camera integrates one 'frame' during a single exposure. For STEM, each row of H is the collection of a single pixel from one beam position, and thus the rows of H operate on x in sequence. While we've described the CS equation in terms of vectors, it's equally applicable to images and volumes which can be 'unwrapped' into long vectors.

The design of H is crucial to ensure an accurate recording of the sample structure or phenomena. The Shannon-Nyquist formula provides a sufficient (but not necessary) guideline that a band-limited signal must be sampled at twice its maximum frequency to prevent artifacts due to subsampling (aliasing)[86]. This can result in an extremely large H sensing matrix, as doubling the height and width of an image quadruples the number of rows and columns in H. Since H is an extremely sparse matrix, with very few non-zero elements for high pixel count images, it begs the question if it's possible to transmit more information for the same number of rows of H by filling some of the non-zero off-diagonal elements. It is precisely this question, where H goes from a sparse to dense matrix, and y consequently from dense to sparse, that is the core of compressive sensing.

Let us consider the case where $P < Q$, which gives a very short, wide sensing matrix and an acquired signal which is shorter than the signal of interest ($dim(y) < dim(x)$). How could we

construct such a scenario? First, let's consider dropping some random number of rows from H. This means y is now fundamentally missing information about x, and it is impossible to exactly represent x. This is obviously an undesirable result and is referred to as an *ill-posed* or *underdetermined* problem[87].
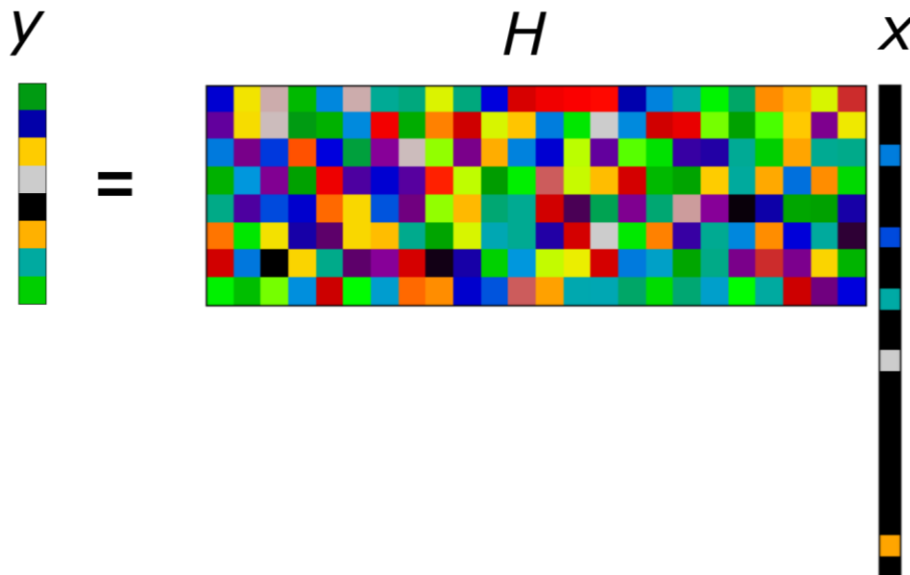
Figure 1.7 A graphical description of the Equation 1.4 for the compressive sensing recovery problem. A dense sensing matrix, H, is used to acquire a series of data points in y about an arbitrary signal x. Taking advantage of prior knowledge about the sparsity of x, it becomes possible to solve this heavily underdetermined problem.

Instead, we will try two things. First, let's apply some constraints to y, specifically that it's sparse or most of its elements are zero (similar to the constraint on H in the conventional acquisition formula)[88]. Second, let's populate all or nearly all of the matrix positions on H without worrying too much yet how we would accomplish that in practice[88]. Each non-zero element of x selects exactly one unique dense column from H which is then linearly combined with the columns from all other non-zero elements to produce the dense vector y. Reconstructing x from y and H involves a *'guess and check'* process to estimate which columns from H were activated by x, which tells us the locations of the non-zero elements[89]. A least square estimate for the coefficients in front of the linear combinations of columns tells us the values of x given their location. The 'sifting' property of y effectively reduces the wide undetermined sensing matrix H into a reduced set of columns corresponding to the non-zero locations, which is well determined and solvable. Since $dim(y) < dim(x)$ this means that our camera or PMT can make fewer acquisitions than dictated by the Shannon Nyquist theorem and still accurately reconstruct a signal from a specimen[89]. In addition, the noise term is added to a linear combination of *many* measurements instead of each one individually, which can substantially improve the signal-to-noise ratio. This has advantages in both time and data transmission/storage rates. The process of converting the original high dimensional and sparse signal down to a low-dimensional dense representation through a multiplication with the sensing matrix is referred to as a *projection* (not to be confused with the general concept of projective imaging in Transmission Electron Microscopy).

Formally, we will try to solve the following minimization problem:

$$\min_{x \in \mathbb{R}^P} \|x\|_0 \; s.t. \|Hx - y\|_2 \leq \epsilon \tag{1.6}$$

This is an L0-minimzation problem where $\|x\|_0 := \text{card}(x)$ is the L0 norm, counting the number of non-zero elements, and $\|\cdot\|_2$ is the L2 norm measuring the Euclidean distance. In practice, we will try to find the sparsest possible approximation of the original signal such that the difference between our estimation and what we measured has a smaller mean squared error than some noise limit in the system.

Finding the absolutely sparsest vector in the L0-minimization task is very complicated (NP-hard) and thus typically an L1-minimization proxy task is used:

$$\min_{x \in \mathbb{R}^P} \|x\|_1 \; s.t. \|Hx - y\|_2 \leq \epsilon \tag{1.7}$$

Where the L1 minimzation counts the absolute values of every non-zero element, $\|x\|_1 := \sum_{i=1}^{P} |x_i|$ [90] The difference between these two expressions is not particularly relevant to an interested microscopist, and many algorithms have been developed to solve these problems, most often using iterative thresholding or some form of basis pursuit[91, 92]. A rich set of Bayesian approaches have also emerged[93].

For these equations to have well determined solutions and for information recovery about x to be possible, two criteria in general must be satisfied. Firstly, as discussed before, the signal x must

be appropriately sparse. Secondly, the sensing matrix H must satisfy some properties to ensure that each reduced set of columns from H generated from the 'sifting' property of x must form an appropriate subspace. Consider the following trivial matrix multiplication:

$$Hx = y \tag{1.8}$$

$$\begin{pmatrix} 3 & 2 & 3 & 1.5 \\ 6 & 3 & 1 & 3 \\ 2 & 7 & 4 & 1 \end{pmatrix} \begin{pmatrix} 1 \\ 0 \\ 0 \\ 2 \end{pmatrix} = \begin{pmatrix} 6 \\ 12 \\ 4 \end{pmatrix} \tag{1.9}$$

The sparse x vector reduces the sensing matrix from a short and wide matrix to a tall narrow one due to its sparsity:

$$\begin{pmatrix} 3 & 1.5 \\ 6 & 3 \\ 2 & 1 \end{pmatrix} \begin{pmatrix} 1 \\ 2 \end{pmatrix} = \begin{pmatrix} 6 \\ 12 \\ 4 \end{pmatrix} \tag{1.10}$$

While this would appear at first glance to be a well-determined problem, note that the two remaining columns of the sensing matrix are linearly dependent (by a factor of 2). Thus, all the following estimates for x are potentially equally valid for this sensing matrix, sparsity, and acquired vector:

$$\begin{pmatrix} 1 \\ 0 \\ 0 \\ 2 \end{pmatrix}, \begin{pmatrix} 2 \\ 0 \\ 0 \\ 0 \end{pmatrix}, \begin{pmatrix} 0 \\ 0 \\ 0 \\ 4 \end{pmatrix} \tag{1.11}$$

It therefore becomes impossible to reconstruct the original signal accurately with only the prior information that it's sparse.

When we design a sensing matrix to be used to record and compress any arbitrary signal x, we must ensure that any possible reduced sensing matrix created by the sifting property of the sparse signal forms a linearly independent set of columns, ie is *full rank*[94]. Proving this in detail is quite challenging, as it involves the combinatoric evaluation of ever increasing sets of columns, which can be quite large for high-dimensional signals which might benefit the most from compression. The restricted isometry constants (RIC), δ_K, is one metric which can summarize the results of such a calculation[94]. For a K-sparse vector, x, (which K non-zero elements) the RIC is the smallest δ such that:

$$(1-\delta)\|x\|_2^2 \leq \|Hx\|_2^2 \leq (1+\delta)\|x\|_2^2 \tag{1.12}$$

This principle, the restricted isometry principle (RIP), directly describes the information preserving strength of a particular sensing matrix[94]. The RIP represents how the sensing matrix preserves the Euclidean distance of the original signal fudged by some small factor 2δ. The reconstruction error can then be directly expressed in terms of the RIP:

$$\|x - \hat{x}\| \le \frac{A}{\sqrt{K}} \|x - x_K\|_1 + B\varepsilon \qquad (1.13)$$

Where A, B are constants depending on the sparsity of the signal, K, and δ_{2K} and x_k is the thresholding of x to the K largest columns[94]. This error term has three key components: a term related to the underlying sparsity of the signal, a series of constants related to the effectiveness of the sensing matrix at compressing any input sparse vector, and a noise component[95].

Given the difficulty in evaluating the RIC on any given sensing matrix, some authors have instead reported the maximum mutual coherence between pairs of columns[96]:

$$\mu(H) := \max_{i \ne j} \left| h_i^T h_j \right| \qquad (1.14)$$

Where h_i is the ith column of H. If the product of the sparsity and the coherence is much less than one, a very conservative quadratic relationship can be derived between the number of acquisitions required and the underlying sparsity of the signal times some constant, ie $Q \ge CK^2$ [96]. Note that designing an incoherent sensing matrix has nothing to do with the coherence of the imaging modality (not HAADF), and the distinction between incoherent measurements and acquisitions will be discussed in detail in the following.

Since the sparsity of the input signals cannot be directly controlled and noise present during acquisition is often unavoidable, performing CS effectively comes down to intelligent engineering of the sensing matrix. As a general rule, it is very difficult to intelligently engineer matrices that

satisfy the RIP, although this is an active area of research. Fortunately, pioneering theoretical work in the 1970s and 80s showed that randomly populated matrices are almost always guaranteed to be incoherent (and with other bases as will be discussed later)[97-99]. It can be shown that with a Gaussian sensing matrix and acquisitions $Q \geq 2Kln\left(\frac{2P}{p}\right)$ a perfect reconstruction can be achieved with probability 1-p [89]. Note that we've gone from $Q = P$ to $Q \propto \ln(P)$, thus the number of acquisitions needed to reconstruct a signal scales only as the log of the requisite final sampling density. This is possible by populating the off-diagonal elements of the sensing matrix, resulting in more information being stored per acquisition.

Before the practical implementation of such a method is discussed, let's first consider performing CS on a non-sparse signal (dense x). In this case, the 'sifting' property is not satisfied and the problem remains highly underdetermined and unsolvable without additional prior information. A clever trick involves decomposing the desired signal x into the product of a sparsifying basis and a vector of coefficients:

$$x = Dw \tag{1.15}$$

$$y = HDw + \varepsilon \tag{1.16}$$

$$\Theta = HD \tag{1.17}$$

$$y = \Theta w \tag{1.18}$$

In this case, the product of a sparse vector, w, with some basis transformation, D, produces the signal of interest, x. We collect the non-sparse signal, y, through the sensing matrix, H, and attempt to reconstruct the sparse signal w using the joint matrix Θ.
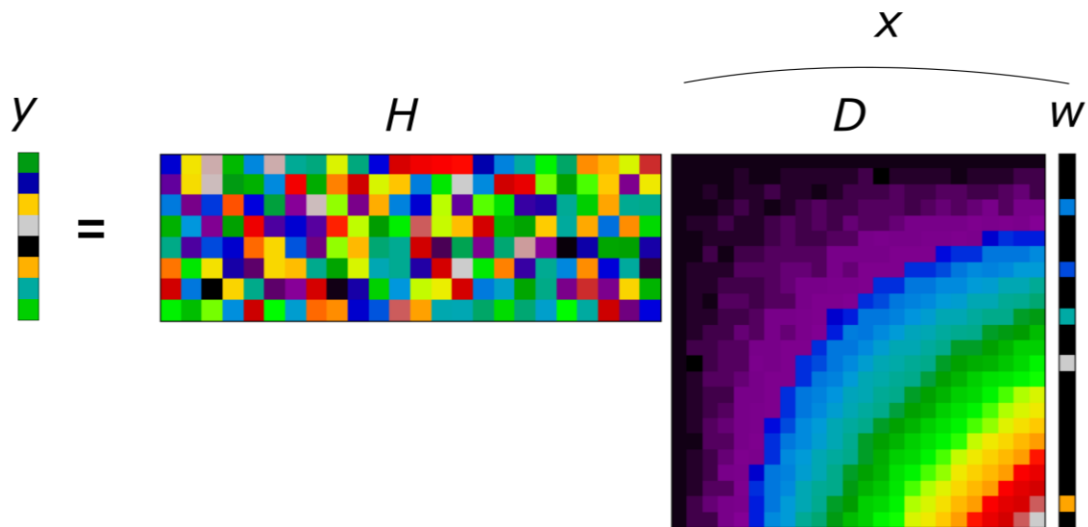
Figure 1.8 A graphical description of the Equation 1.16 for the compressive sensing recovery problem of signals acquired in a non-sparse domain. The use of a structured basis representation which cannot describe the desired signal in a compressed or sparse format can allow for RIC satsified acquisition of a non-sparse signal. Although the sensing matrix may not have to satisfy the RIC in this case, to ensure recovery of w, the joint matrix product of H and D must now satisfy the recovery criteria. By solving for w from y we can make use of the sparsity property to recover the signal. Reconstructing x is as simple as the matrix vector product of w with D.

As long as a proper sparsifying basis for the signal of interest is known, we can perform compressive sensing on distinctly non-sparse signals. Solving for w allows us to reconstruct x by multiplying with the *a-priori* known basis. Note now that the RIC applies to the joint matrix, Θ, since we are interested in the compression of the sparse signal w. Basis transformations which can produce sparse or compressible (approximately sparse) signals are well known and used for image and signal compression, including the Fourier, wavelet, and DCT transformations, although the set of measurement matrices they are incoherent with can be somewhat limited[97].

1.3.1   Practical Challenges with CS

Many algorithms have been proposed to solve for a compressively acquired signal given an appropriate basis and the measurement matrix. Such algorithms have routinely been applied to improve signal quality and reduce acquisition times in optical microscopy, X-ray tomography, and MRI imaging[100-102]. A wide body of literature has emerged over the past five years applying these techniques in electron microscopy as well[103, 104]. Unfortunately, many of those methods proposed are not actually performing CS. It's hoped the following intuitive description will help alleviate some of this confusion.

Let's consider the prototypical compressive sensing experiment, the single pixel camera[105]. The light reflected from a specimen is collected onto a digital micro-mirror array device, in which small mirrors can be manipulated to reflect light on or away from a detector. This sensing matrix, while not randomly Gaussian, can be modeled as a random Bernoulli matrix which has slightly less attractive theoretical properties, but is much easier to practically realize[106]. The detector in this situation is a single photodiode, which outputs a single value for any combination of micro-mirror positions. Having known the position of the micro-mirrors at each time point, an operator can collect the integration of random combinations of mirror positions into a single long vector. The dimensionality of this vector is much less than the dimensionality of the original micromirror device (number of mirrors) and knowing that the image is likely sparse under a wavelet transform an accurate picture of the image can be restored after only a few acquisitions.

However, each 'acquisition' was composed of many light-specimen interactions, as many mirrors were 'on' and collecting signal for each photodiode capture. Each 'row' of the sensing matrix contains the list of 'measurements' which are integrated into a single acquisition. In traditional cTEM or STEM each 'row' contained only a single entry, and thus represented a single beam-specimen interaction. Populating the off-diagonal elements of the sensing matrix does increase the efficiency of each camera or PMT acquisition, but at the cost of including many more beam-specimen interactions. Thus, a real CS acquisition can reduce the time required to record information from a specimen by increasing the effective area dose by an order of magnitude.

Real applications of compressive sensing in electron microscopy have therefore exclusively been focused on accelerating the acquisition speed of detectors[107]. This has been done by introducing a semi-electron transparent membrane behind the specimen and randomly jittering it to create a pseudo-flutter shutter (or coded aperture) effect[108]. The challenges fabricating a reliably transparent Bernoulli mask for electrons, as well as jittering with a piezo driver without introducing unwanted vibrations into the chamber have resulted in little follow-up work. Inherent in such a scheme some electrons which have interacted with the specimen are rejected by the coded mask (or the sensing matrix), meaning that the dose efficiency is again lower than normal imaging. Improving the reconstruction quality by designing a true Gaussian sensing matrix is likely practically impossible for an electron microscope.

We have seen thus far that real compressive sensing operates exclusively in a post-specimen fashion, by selectively modulating the spatial distribution of intensity into a lower dimensional signal. Such a technique has theoretical guarantees regarding the recovery ability, a fact which has unfortunately been somewhat abused in the literature. Many papers claiming to have performed compressive sensing in the electron microscope have instead relied on modifying the pre-specimen lenses to reduce the total electron dose. Such techniques have no theoretical guarantees regarding their performance, and most rely on exhaustively tested empirical guidelines. These methods will be discussed in the following chapters.

1.4   Scope of Dissertation

This thesis will describe several methods utilizing machine learning or image processing to design new methods of interrogating material specimens with a focus on electron beams. In principle, many of the techniques delineated henceforth are equally applicable to many other instruments if the primary mechanism of imaging involves the sequential interaction and collection of a finite probe with a sample. **Chapter 2** will first review a direct way to reduce the impact of multiple probe/sample interactions by directly under-sampling the specimen of interest. The novel use of an electrostatic deflector into the electromagnetic column is proposed to allow for the facile and repeatable interruption of electromagnetic scanning. Several machine learning techniques will be discussed for the reconstruction of image quality, with a focus on dictionary learning approaches due to their effectiveness at low sampling rates. Empirical methods for analyzing the resulting image quality will then be discussed in lieu of theoretical guarantees that might be present for compressive acquisitions. **Chapter 3** will then highlight an advanced collection method in which the under-sampling strategy is deployed *'on-the-fly'* rather than pre-determined before the interaction of the probe with the sample. A module is developed to distribute the method on virtually all scanning transmission electron microscopes (STEMs) and the effectiveness evaluated for varying amounts of prior information. The method will be discussed in the context of alternate control and policy selection strategies, including reinforcement. This thesis will then shift gears slightly in **Chapter 4** and discuss creating large 4-D datasets of orientation space information from

polycrystals using a hybrid beam-stage rocked electron microscope. As the alignment of flat planes observed at varying perspectives is a well solved problem in image processing, many thousands of full electron channeling contrast images (ECCIs) can be collected at a variety of stage/beam tilts to enable radically large and high angular resolution orientation maps. The possibility applying these methods in ion microscopes and for the disentanglement of many competing defect structures will be discussed. Finally, **Chapter 5** will summarize the thesis and highlight some key potential items for future work. In the spirit of increasing accessibility, the relatively low cost of implementing the techniques discussed in this thesis will be further emphasized.

CHAPTER 2: UNDERSAMPLING OF SEM IMAGES FOR DOSE MITIGATION

Abstract

Electron microscopy of biological, polymeric, and other beam-sensitive structures is often hampered by deleterious electron beam interactions. In fact, imaging of such beam-sensitive materials is limited by the allowable radiation dosage rather than capabilities of the microscope itself, which has been compounded by the availability of high brightness electron sources. Reducing dwell times to overcome dose related artifacts, such as radiolysis and electrostatic charging, is challenging due to the inherently low contrast in imaging of many such materials. These challenges are particularly exacerbated during dynamic time-resolved, fluidic-cell imaging, or 3-D tomographic reconstruction – all of which undergo additional dosage. Thus, there is a pressing need for the development of techniques to produce high quality images at ever lower electron doses. In this contribution, a direct dose reduction and suppression of beam induced artifacts through under-sampling pixels is demonstrated, by as much as 80% reduction in dosage, using a commercial scanning electron microscope with an electrostatic beam blanker and a dictionary learning in-painting algorithm. This allows for multiple sparse recoverable images to be acquired at the cost of one fully sampled image. This approach may open new ways to conduct imaging which otherwise require compromising beam current and/or exposure conditions.

2.1   Radiation Challenges for Organics and *In-Situ* Experiments\

Dynamic observations with high intensity electron probes have revealed detailed electronic and elemental information at previously unachievable spatial and temporal resolution [109, 110]. Many of these observations are facilitated by the increased brightness of electron sources that afford the necessary signal-to-noise (SNR) ratio for meaningful imaging, analysis and interpretation. In addition, sample holders allowing the introduction of a fluidic cell for *in situ* imaging of dynamic phenomena are widely available [111]. Despite the bevy of signals and environments selectable inside the electron microscope, artifacts and sample damage due to electron dose have remained challenging for materials susceptible to knock-on damage [112], radiolysis [113], electrostatic charging [114], sample heating [115], and beam induced reduction [116]. Many material systems are highly sensitive to these damage mechanisms, as operating at higher magnifications can significantly increase the electron dose per unit area. These shortcomings have been acutely felt for many decades in the biological electron microscopy community due to the ease of beam damage in most organic systems [117-119]. Organic and biological systems are particularly susceptible to electrostatic charging due to their insulating electronic structures, and weak bonding that can be heavily be perturbed by incident electrons. In addition, many of these damage mechanisms and artifacts are compounded in time-lapsed imaging common among *in situ* experiments. Imaging dynamic chemical reactions in native environments could help us gain fundamental understanding of the reaction mechanisms behind catalytic and chemical processes for energy and medicine [120, 121].

However, the electron beam may alter reaction pathways after multiple exposures through sustained reduction of the participating chemical species [122]. Electron beam induced crystal growth and electrostatic interactions with nanoparticles have also complicated the unobstructed observation of *in situ* materials [123]. Challenges maintaining appropriate SNR while limiting artifacts and damage from dose in experiments involving these described systems, such as organic and biological materials or fluidic or gaseous observations, have motivated the search for alternative methods of imaging.

2.2 Under-sampling and Non-Compressive Imaging

In a typical scanning electron or scanning transmission electron microscope (SEM/STEM) a pair of electromagnetic scanning coils rasters the beam across the specimen while a resulting signal at a digitized set of beam positions is recorded into an image. There is typically a 'slow' and 'fast' scan axis, where the 'slow' scan axis is held fixed while a 'row' of the image is collected. After completion of one 'row' of the image, the beam is quickly jumped back to the opposite side of the image and allowed to settle, as the electromagnetic scan coils have a finite response time. This settling time (or fly-back time) can be quite large and result in the anisotropic deposition of electron dose, usually appearing as thick contamination layer along the left side of the image. In addition,

for high pixel-density images this settling time may contribute a non-negligible amount to the total imaging time.

In the context of the sample and instrument limitations there are two key challenges:

1. Reduce the time to record full images
2. Limit the impact of dose and multiple observations

As discussed in the introduction, Compressive Sensing (CS) has been proposed by multiple authors as a solution to this problem. However, since CS actually increases the number of probe sample interactions, it's not clear how one would design a populated sensing matrix for a serial scanning technique or if it would have advantages in terms of dose. The serial nature of scanning electron imaging is not unique to SEM/STEM and is shared by virtually all radiative or mechanical probe instruments (including XRF and atomic force microscopy). Multi-beam SEMs which could potentially allow for the recording of multiple beam positions onto a single detector do exist, but on-the-fly modulation of each beam independently by a random factor as would be required by a true CS sensing matrix remains impractical[124].

Since most SEM/STEM images are heavily compressible under common image transforms, it suggests that there's considerable amount of redundancy in such images[125]. This begs the question if it is truly necessary to acquire images at the pixel densities they were originally recorded at since

a lot of the information will be thrown out when archiving, transmitting, or publishing the images. Many novice or intermediate users will record images exclusively at pixel densities of 1024x1024 or 2048x2048, which at a micron field of view means a span of several pixels are below the physical resolution of common SEMs. These additional pixels are not really contributing meaningful information and are recorded for aesthetic reasons.

Taking advantage of the fact that images have relatively low informational content given their high dimension, it has been proposed that under-sampling and post-collection image recovery could be an effective way to reduce the impact of radiative imaging without altering the underlying content[126-129]. In fact, an analysis of a database of electron microscopy images determined that most secondary electron images are highly amenable to such a technique[130]. The high degree of textural similarity or repeated motifs in most materials samples (columns of atoms, scattered nanoparticles, etc.) increases the redundant information since contrast motifs are shared over the field of view.

In principle, there are a combinatorial number of ways to sample a configuration of pixels from an image. Since it has been assumed that not all pixels are contributing information, this logically leads to the conclusion that there is a reduced subset of pixels which dominate the informational content. Thus, not all sampled configurations of pixels from an arbitrary image will have the same informational content. How the subsampling is performed therefore has an extremely large impact on the final image quality. Spacing measurements uniformly and equidistantly on a grid is

unfavorable, as this is equivalent to simply scanning with larger pixel sizes. Instead, non-cartesian methods, such as spiral and Lissajou scanning, will be primarily discussed, as well as random pixel and line scanning.

For random sampling, the 'identity' sensing matrix in conventional scanning:

$$y = Hx \tag{2.1}$$

$$H = \begin{pmatrix} 1 & 0 & 0 & 0 & 0 \\ 0 & 1 & 0 & 0 & 0 \\ 0 & 0 & 1 & 0 & 0 \\ 0 & 0 & 0 & 1 & 0 \\ 0 & 0 & 0 & 0 & 1 \end{pmatrix} \tag{2.2}$$

Has random elements along the diagonal replaced with zeros:

$$H = \begin{pmatrix} 1 & 0 & 0 & 0 & 0 \\ 0 & 1 & 0 & 0 & 0 \\ 0 & 0 & 0 & 0 & 0 \\ 0 & 0 & 0 & 0 & 0 \\ 0 & 0 & 0 & 0 & 1 \end{pmatrix} \tag{2.3}$$

In contrast to a CS acquisition, this reduces the number of probe/sample measurements during a full acquisition. By subtracting these 'zero' rows the number of acquisitions can be reduced and collection time potentially improved, although practically this may not always be possible for some implementations:

$$H = \begin{pmatrix} 1 & 0 & 0 & 0 & 0 \\ 0 & 1 & 0 & 0 & 0 \\ 0 & 0 & 0 & 0 & 1 \end{pmatrix} \qquad (2.4)$$

This is now an underdetermined problem since some pixels are inherently unmeasured, and some prior information about the image/structure is needed in order to infer or simulate the missing values in a plausible manner. Effective algorithms have been demonstrated for this problem for a wide class of images, but there remains no theoretical guarantee that we will perfectly reconstruct the original signal. It is therefore necessary to rely on empirical guidelines by experimentally testing different sampling schemes and reconstruction techniques to lay out best-practices for performing sub-sampling on previously unseen images.
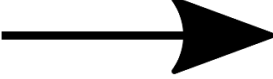
Technique	Compressive Sensing	Under-sampled Imaging	Conventional
# of Measurements	~ P*Q	~ 0.2-0.3 P	~P=Q
# Acquisitions	~ Kln(P)	~ 0.2-0.3 P	~P=Q
Recovery Guarantee	Theoretical Support	Empirical Guidelines	Shannon-Nyquist

Table 2.1 A comparison of the number of measurements (physical probe sample interactions), acquisitions (recording a signal on camera/detector), and the guarantee regarding signal recovery for a compressive sensing system, under-sampled imaging method, and conventional fully scanned raster imaging.

Several simulations on electron micrographs have been published utilizing various in-painting algorithms including TV minimization [129] L_1 split-bregman algorithms [131], and dictionary learning (which are still incorrectly referred to as Compressive Sensing) [132]. While such an imaging method does not really satisfy incoherence criteria or the restricted isometry principle for compressive sensing to apply, recovering images from real space under-sampling can still utilize well-known local statistical correlations between nearby pixels in most images [133, 134]. Probabilistic dictionary learning algorithms, such as the Beta Process Factor Analysis (BPFA) algorithm, exploit this correlation to achieve state of the art recovery from heavily under-sampled images without the use of a training set or a preselected dictionary [135].

Apply Randomized Sensing

Dose, Time, or General Cost Reduced Image

Learn Image Dictionary from Observed Pixels

Inpaint Missing Pixels Using Dictionary
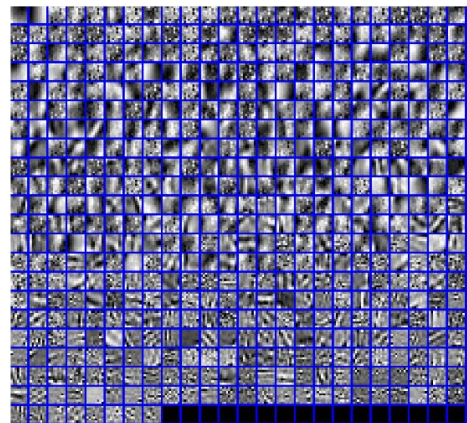
Figure 2.1 Proposed workflow in which an image to be acquired is sub-sampled randomly through some reducer agent, an electrostatic beam blanker in this case. The image collected is decomposed into a Dictionary containing common textures and features and an estimate of the original image is produced using a linear combination of dictionary elements on a patch-by-patch basis. The final estimate achieves a high degree of similarity to the desired image while having been collected with considerably fewer measurements and acquisitions. This potentially saves time while also reducing the area dose the sample experiences in a radiative imaging modality.

Although effective algorithms have been available to recover under-sampled images, previous approaches to experimentally realize a non-raster type scanning in an electron microscope have been limited due to inherent hysteresis in the scan coils, and careful attention must be given to avoiding damage due to overheating from the constant acceleration and deceleration needed to achieve random sampling [130]. Herein, the use of a high-speed electrostatic beam blanker is proposed to achieve a scanning "mask" in which certain pixels are un-sampled by deflecting the electron beam away from the sample. This allows for the design of scanning masks that may not be feasible through direct beam control due to limitations of the scan coils, while being more easily implementable on many microscopes.

2.3   Materials and Methods

2.3.1   Modification of Electron Microscope

A commercial SEM (FEI Quanta 600F) with an electron beam lithography system (JC Nabity Lithography Systems) was utilized to sparsely image samples of interest. It is worth noting that the general form of this methodology is equally applicable to any instrument where information is sampled serially in any digital scan systems (e.g., any model of Scanning Electron Microscope, Scanning Transmission Electron Microscope, or Scanning Probe Microscope, etc.). Images were acquired in a raster scan with the beam rapidly deflected away from the sample for the pixels determined to be un-sampled through the use of a high-speed electrostatic beam blanker. In this way, the overall area dose was reduced as the electron beam only interacted with a user selected sampling "mask".

2.3.2 Dictionary Learning
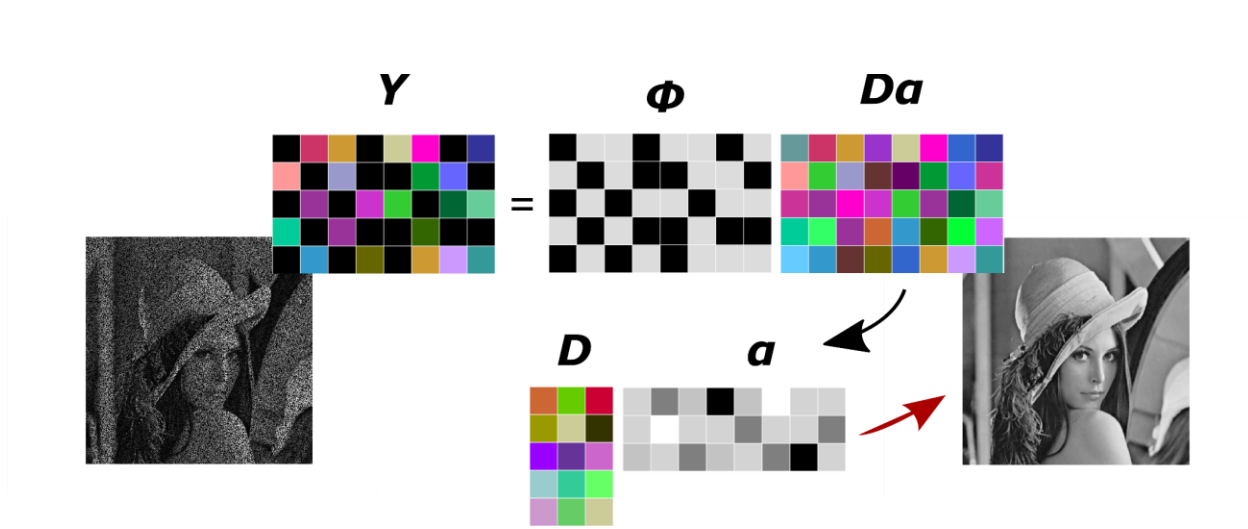
Figure 2.2 Graphical figure describing the masking process performed by the electrostatic beam blanker, as a Hadamard product (elementwise). The collected image has a high number of missing entries, which is modeled using a Dictionary and activation matrix. Iteratively solving for a dictionary representation of the image in terms of common textures and patterns and the proper activation matrix allows for an estimation of the fully sampled image.

Dictionary learning algorithms seek to find an accurate representation of data given the multiplication of a dictionary matrix, D, by corresponding dictionary weights, α. Generally, we can imagine the columns of D as important "features" of the data of interest and α representing the relative activations of these different features throughout the image. Instead of using an off the shelf dictionary (or transform) such as the Wavelet transform, it is often beneficial to learn useful

dictionary elements strictly from the observed data. Given the innate uncertainty with recovering missing pixels and the high number of model parameters it is natural to turn to a Bayesian formulation of the problem. In this case, it is assumed there is some learnable underlying statistical structure in the image that can be used to recover the missing measurements in the image.

To identify the dictionary and weights the Beta Process Factor Analysis algorithm (Zhou et al. 2009) is used. In this algorithm, only information from the observed pixels in each independent image is used to construct the dictionary, so no offline dictionary construction with training data is needed. Further, the only assumption made by algorithm is the sparse activation of weighting coefficients, which is achieved by the Beta-Bernoulli statistical process. In simple terms, this assumption ensures that each image patch will be recovered using only a few dictionary elements, rather than using small amounts of the entire dictionary. In their paper they have demonstrated that a sparse activation matrix is a good prior assumption for natural images.

To learn this local structure, the image is divided into 8x8 overlapping pixel patches which are unwrapped into 64 dimensional vectors, from which our objective will be to identify the likeliest combination of weighting coefficients and dictionary elements to explain the observed pixels. This is done by estimating the posterior probability distributions for the dictionary and the weighting matrices, which gives probability of model parameters from the observed data. Once this combination has been determined, the missing pixels are inpainted using straightforward matrix

multiplication of the dictionary and the weighting matrix and the recovered patches are summed together to reproduce the image.

Mathematically, we can describe the sparse imaging and dictionary learning process through the following equation:

$$v_i = \Phi_i x_i \tag{2.5}$$

$$v_i = \Phi_i D_i \alpha_i + \epsilon_i \tag{2.6}$$

Where x_i represents the "true" fully sampled image, v_i represents the sparsely sampled image, Φ models the electrostatic beam blanking by zeroing out a random percentage of true pixel values, and a residual ϵ_i represents noise in the measurement process. The learned dictionary D and its corresponding weight matrix α linearly combine to reconstruct the most probable true image x as illustrated by the following equation:

$$x \approx d_1 \alpha_1 + d_2 \alpha_2 \cdots d_k \alpha_k \tag{2.7}$$

We have employed the same notation as Stevens et al. for consistency. Practically, the BPFA algorithm iteratively seeks D and α using analytical update rules derived from Gibbs sampling given in the original work (Zhou et al. 2009).

In this implementation, the secondary electron (SE) signal for each of the sampled pixels was stored and loaded into the BPFA algorithm (implemented in MATLAB). This algorithm was selected due to the fact that it requires no pre-training of the dictionary and has few assumptions beyond an underlying learnable statistical structure and sparse activations, and is therefore very generalizable to many types of imaging. Detailed technical information on the algorithm can be found in original works in the following references[135-140].

To evaluate the quality of images generated using this sparse imaging method, the Peak Signal to Noise Ratio (PSNR) and the cross-correlation factors (CCF) are used, which are defined below:

$$PSNR(dB) = -10\log[I(:) - I_{ref}(:)] \tag{2.8}$$

$$CCF = \frac{\sum_m \sum_n (I_{mn} - I)(Iref_{mn} - Iref)}{[\sum_m \sum_n (I_{mn} - I)^2][\sum_m \sum_n (Iref_{mn} - Iref)^2]} \tag{2.9}$$

These metrics are commonly employed in the digital image processing community to reflect the quality of image compression and reconstruction between different algorithms on the same image.

2.4   Experimental Results on FEI Quanta SEM

Several simulations were first run on a variety of biological and material samples with complicated structures to determine the most appropriate sampling mask for general imaging. The PSNR and cross correlation coefficients of reconstructions from several different simulated scan patterns on a variety of fully sampled images collected from a microscope were examined in Figure 2.3. These scan patterns include those generated from trigonometric function (Spiral and Lissajous) as well as simply subsampling horizontal lines from the image, modeling a coarse raster scan.

Original Images
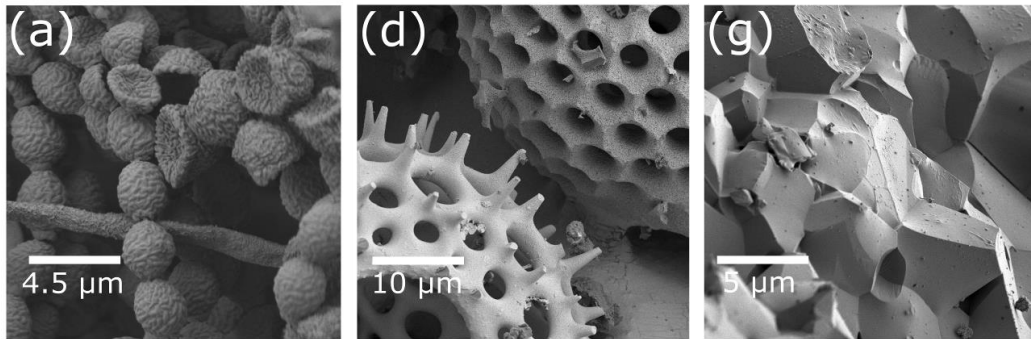
Randomly Sampled Images
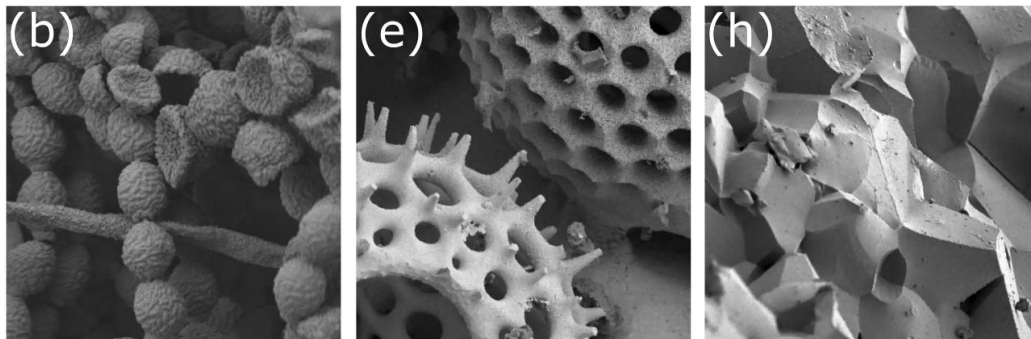
Spiral Sampling	Lissajous Sampling	Subsampled Lines
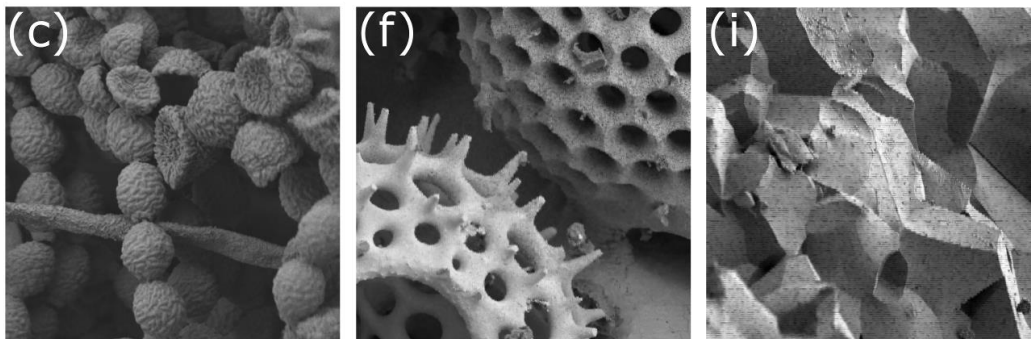
(j)

	Diatom Cross Corr.	Diatom PSNR (dB)	Cork Cross Corr.	Cork PSNR (dB)	Fracture Cross Corr.	Fracture PSNR (dB)
Random	0.9757	26.1645	0.9885	34.3821	0.9838	28.7733
Lines	0.9635	24.2868	0.9610	28.2310	0.9573	23.5935
Lissajous	0.9731	25.7155	0.9866	33.7097	0.9809	28.0742
Spiral	0.9751	26.0516	0.9894	34.7147	0.9825	28.7171

Figure 2.3 Simulations of reconstructing under-sampled images with varying sampling "masks". Sampling for all masks was performed with only 15% of the total pixels physically sampled. (a-c) Fully sampled and reconstructed sparsely sampled images of yeast bacterium on cork demonstrating the effectiveness of random and spiral scanning masks. (d-f) Image of a biological diatom comparing reconstructions from Lissajous and random scanning. (g-i) A fractured steel surface comparing random scanning to a reconstruction simulating a coarse raster scan with lines subsampled to achieve the same pixel count. (j) Quantitative metrics comparing the effectiveness of inpainting the different proposed scanning masks.

As seen above in Figure 2.3, random sampling most commonly achieves the highest quality metric of all the proposed sampling schemes on two of the three samples and avoids several prominent artifacts. A coarse raster scan, ie subsampling horizontal lines, results in the far poorest performance and introduces very noticeable artifacts that detract from the interpretability of the image. Lissajous scanning achieves consistent quality metrics, but introduces jagged aliasing on sharp diagonal features such as the diatom frustules. On the other hand, spiral scanning performs surprisingly well in all three cases, however it drastically under samples the edges of the image and can result in blurry peripheral features. An additional advantage of random sub-sampling is that it is easy to construct scanning masks composed of mutually exclusive pixels, ie at 30% sampling a user can produce three images in which no pixels are sampled more than once. Due

to this fact, all further experiments in this thesis will employ random sampling, taking advantage of the electrostatic beam blanker to achieve this effect.

As a proof of concept, several geometrically diverse, complicated and heterogeneous samples with minimal beam sensitivity were selected to experimentally examine the quality of the reconstruction against a fully sampled image. Varying sampling percentages were collected with different dwell times to examine the dual effect of noise and under-sampling on the reconstructed image. These experiments on a physical microscope are listed below.
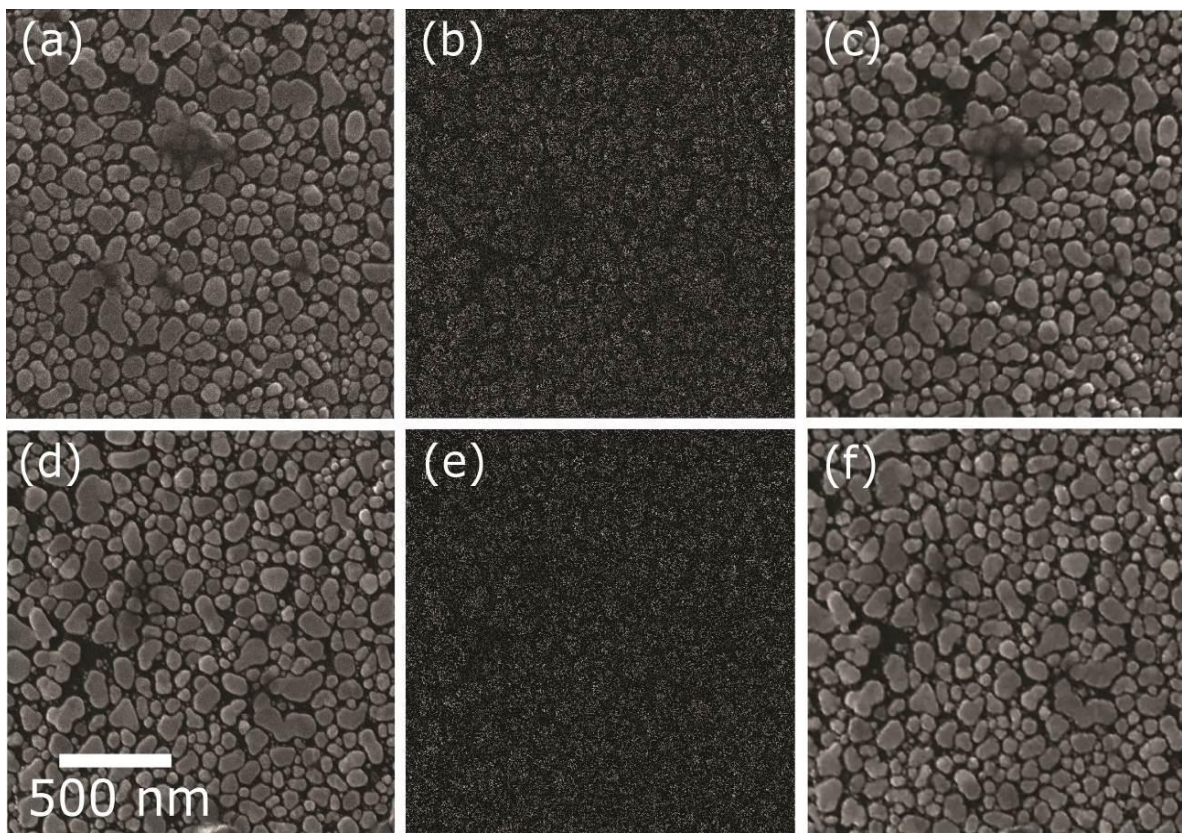
Figure 2.4 Both sparse and full images were captured at 30 kV and 283 pA beam current. (a) A fully sampled image of gold nano-islands on a carbon substrate collected at a dwell time of 5 μs (area dose of 1424 e$^-$/nm^2). (b) 30% sparsely sampled image with a pixel dwell time of 5 μs (427 e$^-$/nm^2). (c) Reconstructed sparse imaging pattern of the sample area imaged in A. (d) Another fully sampled image of a different region of the same sample with a 25 μs dwell time (7120 e$^-$/nm^2). (e) Sparsely collected image with only 20% of the total pixels collected (1424 e$^-$/nm^2). (f) Reconstructed sparse image of the same sample area as imaged in (d).

A dense collection of gold nano-islands prepared on a carbon substrate was selected as the first sample. As seen in Figure 2.4, short dwell times can often result in noisy and blurry images due to Poisson-like noise. This can be seen by comparing fully sampled images 2.4a and 2.4d, where the longer dwell time results in sharper and cleaner features. The middle panels (2.4b and 2.4e) show the raw output of the sparse imaging process from the microscope, where the naked eye has great difficulty resolving the structure of the gold nano-islands due to heavy under-sampling. However, the reconstructions in the right panels from 30% and 20% sampling rates, respectively, show strong correlation with the fully sampled images. Complicated features are well reconstructed and a strong majority of point features are maintained, while simultaneous de-noising can often ameliorate the presence of Poisson-like noise at low exposures. It is particularly interesting to note that the effective *area* dose in Figure 2.4f is effectively the same as in 2.4a, as the area dose is calculated as dose per pixel multiplied by total number of pixels and the pixel area.
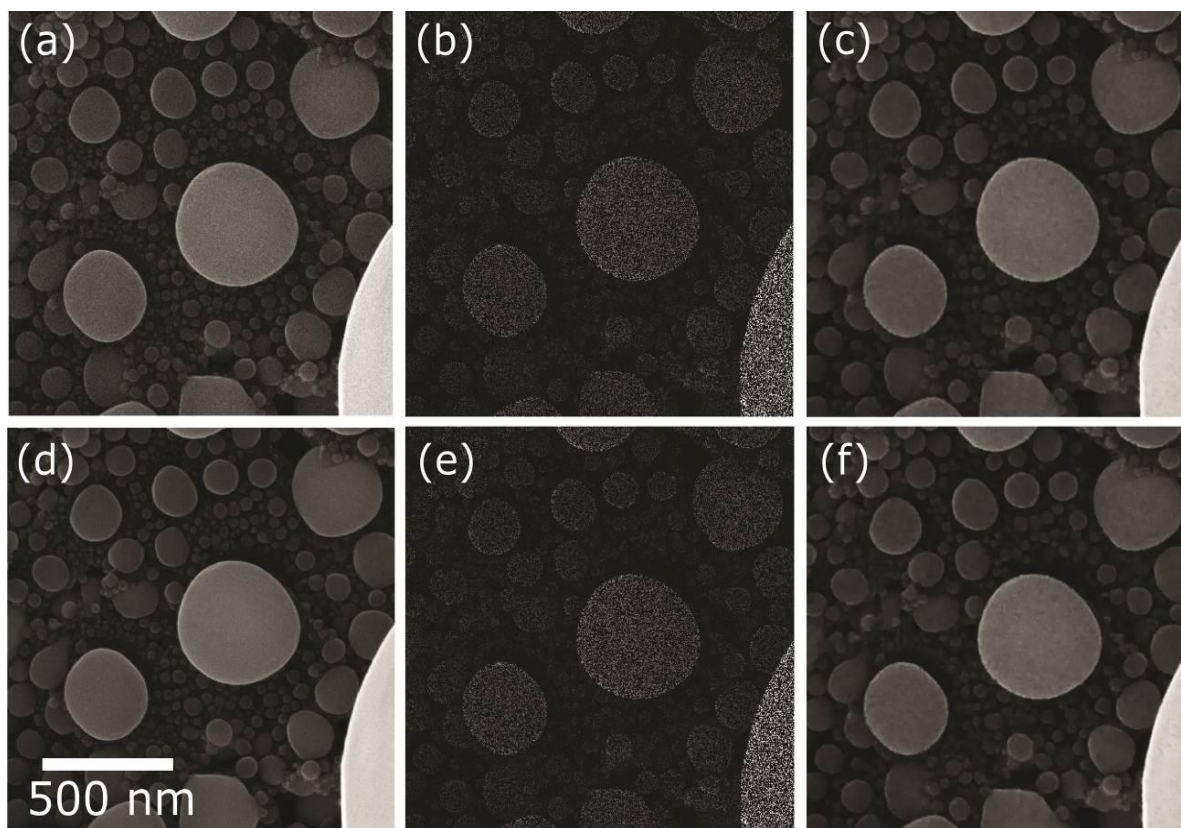
Figure 2.5 As in the previous figure, images were captured at 30 kV and 283 pA beam current. (a) A fully sampled image of tin nanoparticles of various diameters collected at a dwell time of 5 microseconds (area dose of 1234 e$^-$/nm^2). (b) Sparsely sampled (30%) image with a pixel dwell time of 5 microseconds (370.2 e$^-$/nm^2). (c) Reconstructed sparse imaging pattern of the sample area imaged in (a). (d) A second fully sampled image of the same area with a 25 micosecond dwell time (6170 e$^-$/nm^2). (e) Sparsely collected image with 30% of the total pixels collected (1851 e$^-$/nm^2). (f) Reconstructed sparse image of the same sample area as imaged in (d).

Next, tin nanoparticles prepared on a silicon substrate were selected to validate the sparse imaging methodology for samples with a similar array of geometric shapes, but highly heterogeneous sizes and shapes. Figure 2.5 shows the results of the full and sparse imaging processes, as well as the final reconstructions from the BPFA algorithm. Similar to the gold nano-island example, high quality reconstructions were obtained for sampling as low as 30 %.

We then examined several biological nanomaterials that are highly susceptible to drift and shrinkage due to electrostatic charging and radiolysis. A sample of human collagen (fibril diameter ~ 100nm) was used due to its tendency to drift and move under the electron beam, which compromises several quantitative analyses for use in subsequent applications of these structures. Observing the distribution of collagen in joints and other isolated areas of the human body may give clues to the injury and healing process in areas that are highly limited blood flow [141]. In addition, it has been shown that the performance of hybrid collagen based tissue scaffolds is highly dependent on collagen alignment and the resulting mechanical anisotropy [142]. Therefore, the ability to image such collagen fibrils without altering their sensitive structure would greatly speed the quantification of treatment efficacy in cartilaginous structures. The collagen was obtained from a human patient, then immediately placed in fixative and processed with Osmium tetroxide and dehydrated with ethanol followed by critical point drying. The sample was then mounted to an SEM stub with silver paint and coated with 5nm of Osmium in a plasma osmium coater prior to imaging.

(a)

2 µm

(b)

(c)

1 µm

(d)

(e)

Cross-Correlation

Full Images
Sparse Images

Number of Images

(f)
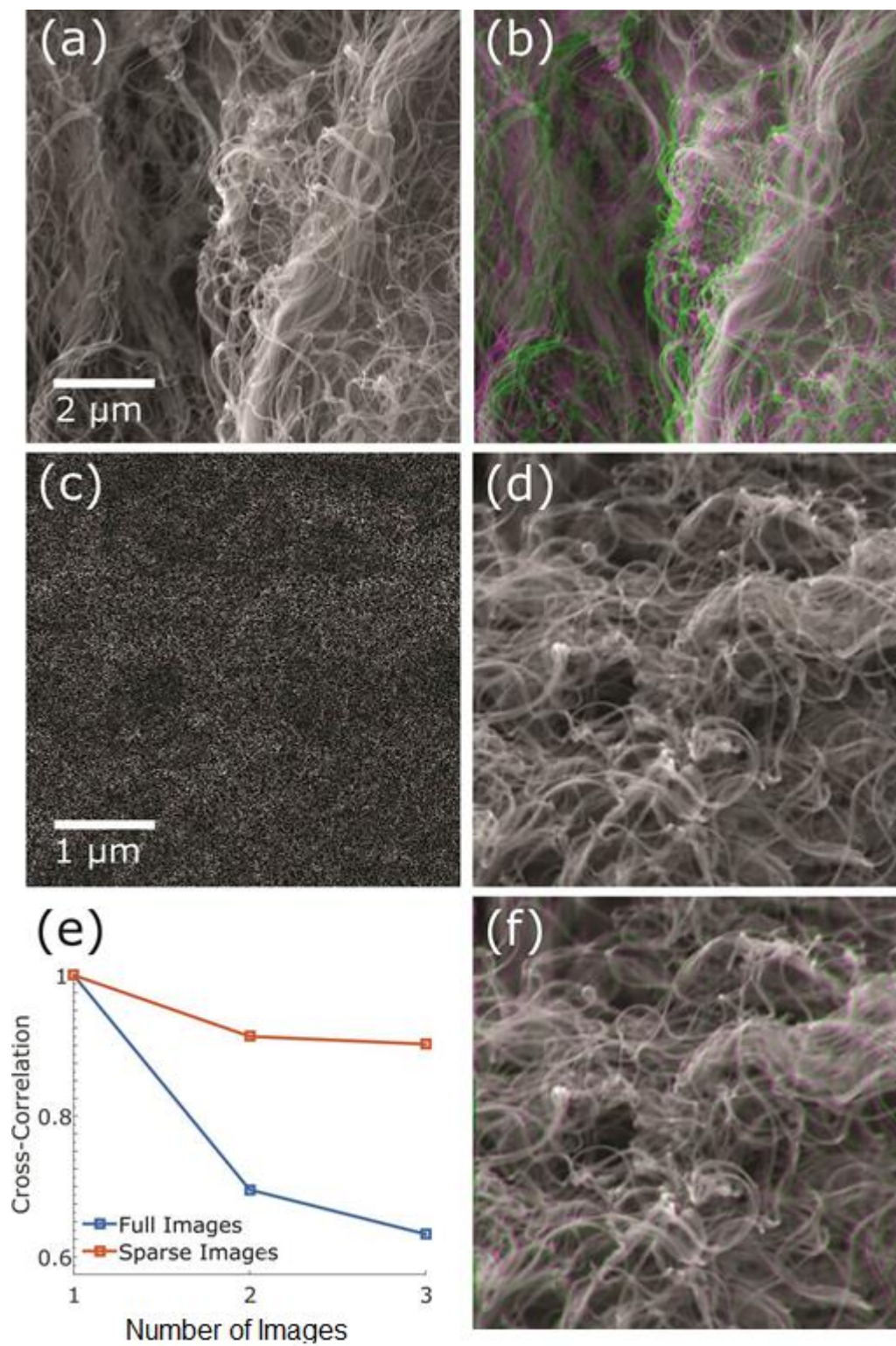
Figure 2.6 Sample imaged at 30kV with 48.2 pA beam current with a full image area dose of 20.45 e$^-$/nm^2 and a sparse image area dose of 6.135 e$^-$/nm^2 (a) A fully sampled image of human collagen prepared on carbon tape. (b) A second fully sampled image overlaid on the original image showing large distortion and sample movement due to beam sample interactions, with differences highlighted with green and purple. (c) Raw sparse image on the same sample collected at 30% sampling rate. (d) The reconstruction of the under-sampled data with the BPFA algorithm. (e) The cross correlation vs. three sequences of images captured using 100% sampling and 30% sparse sampling. A very strong reduction in similarity between fully sampled images is observed, while sparse images maintain high similarity due to strong reduction in electron dose and corresponding dose induced artifacts. (f) The differences between the first and third sparse image are highlighted with green and purple and show significantly reduced beam induced sample alteration compared to (b).

As seen in Figure 2.6 although SEM can produce high quality micrographs of complicated collagen distributions, multiple images can result in substantial changes to the native collagen architecture. The overlaid images in Figure 2.6b show just how significant this sample distortion can be between just two exposures. Sections highlighted with green and purple are areas of the first and second image, respectively, which do not match when overlaid due to electrostatically induced sample drift. The drift associated with individual fibrils under the electron beam in 2.6b can be more than 400% their diameter (>450 nm translation for a fibril diameter of 100nm). On the other hand,

sparse imaging can produce images of similar quality with only 30% sampling rates. Figure 2.6e quantitatively demonstrates this "*three for the price of one*" effect, as the similarity between three fully sampled images diverges quite quickly due to the extreme beam sensitivity of the sample. However, the cross correlation for the three subsequent sparse images is effectively constant, demonstrating the direct dose reduction. In the case of the sparse images, only one low-mag full sampled image was captured prior to imaging sparsely to rule out the formation of a polymerized hydrocarbon film in reducing sample movement.

Samples for *in situ* fluidic cell microscopy were prepared by first thermally evaporating 2 nm of Cr followed by 8 nm of Au on custom fabricated MEMS chips with electron transparent silicon nitride membrane windows. Thiolated DNA oligonucleotides were then attached to the gold surface and used to immobilize DNA functionalized gold nanoparticles through complementary DNA binding interactions [143]. The nanoparticle coated chips were then mounted over a reservoir containing a buffer solution (0.5 M NaCl, 0.01 sodium phosphate, pH=7.4) and loaded into a custom built SEM liquid cell holder that will be described in detail in a forthcoming manuscript. Imaging was carried out using an accelerating voltage of 25 kV and a solid-state backscattered electron (BSE) detector.
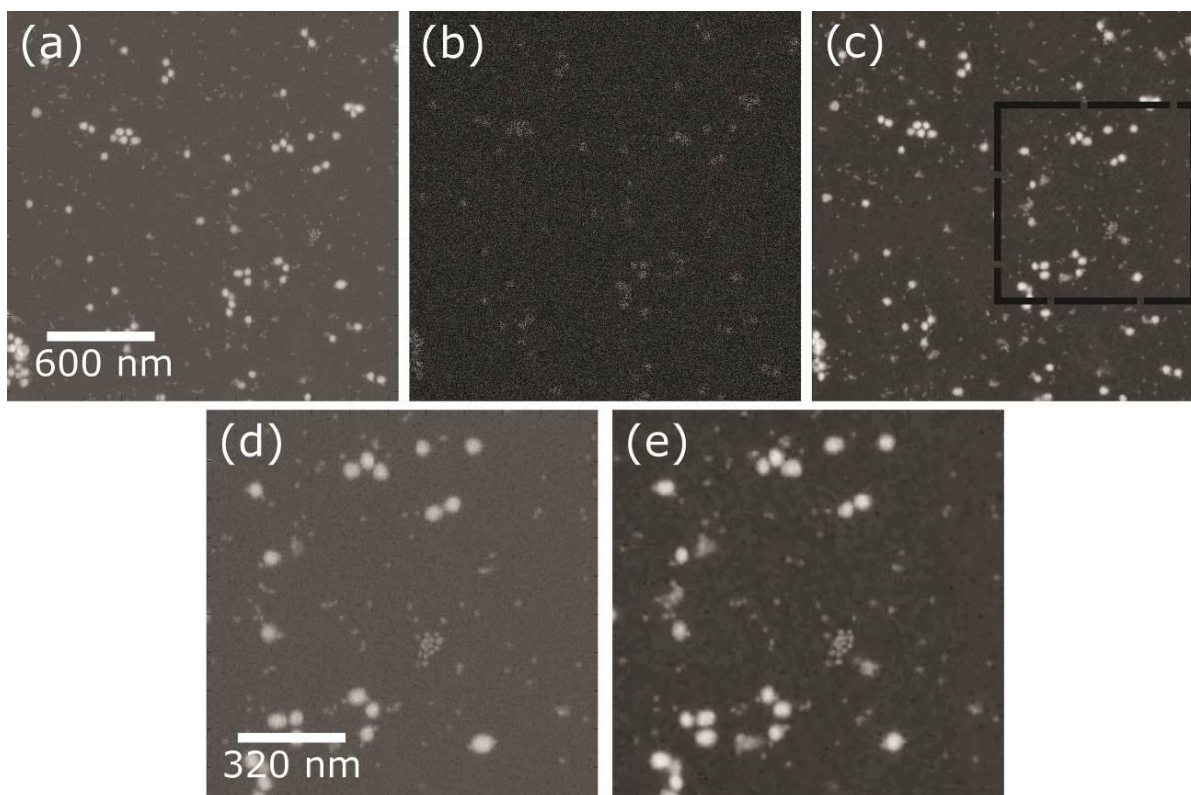
Figure 2.7 (a) A fully sampled secondary electron (SE) image of 80 nm and 30nm gold nanoparticles immersed in water on a porous gold substrate. (b) A sparse 30% sampled experimental image collected for reconstruction of the same sample. (c) The reconstruction of the sparsely sampled image showing strong similarity and dramatically reduced background noise as compared with (a). (d) A zoomed in image of the inset in (c) highlighting the noise present in most SE images in liquid environments. (e) The same inset from the reconstruction which was experimentally collected after the fully sampled image. The highlighted region displays nanoparticles that are present and observable in the sparse imaging method, that were attracted to the region when capturing fully sampled images, possibly due to a combination of electrostatic

interactions and electron beam induced cross-linking of the DNA linkers. Multiple 30nm particles are missing from the fully sampled image, and clumps of particles not resolvable in the fully sampled image due to noise are clearly distinguishable.

In situ fluidic-cell experiments have shown to be highly susceptible to dose related damage and artifacts due to the need to capture sequences of images with the fluidic medium providing samples with great mobility and potential side reactions with aqueous electrons. This is particularly important for the observations of interactions of nanoparticles and nucleation and growth or supramolecular chemical reactions, for example. Depending on the nanoparticle surface charge, electrostatic effects can cause attraction or repulsion of particles in the viewing area as well as beam induced agglomeration [144]. In addition, unavoidable noise due to the low SNR of such experiments makes such observations challenging, particularly with BSE imaging in the SEM liquid cell. However, as shown in Figure 2.7 the sparse imaging method is well suited to this problem. Since the algorithm models some of the additional noise and can distinguish the correct signal to use for inpainting, the sparsely imaged sample produces a lower noise image than the fully sampled image while all major features, including the small 30nm nanoparticles, are retained. For the case of DNA functionalized nanoparticles, the nanoparticles are attracted to the field of view under high dose irradiation. This effect is seen in the sparsely sampled image in Figure 2.7e following acquisition of the fully sample image in Figure 2.7d. These small particles are highly mobile and are likely "glued" to the surface during high dose imaging due to crosslinking effects.

In addition, nanoparticles, which had clumped together and were not individually distinguishable due to high noise in the fully sampled image, are clearly separable in the sparse image. In this way, sparse imaging may provide the "one-two punch" needed for *in situ* experiments, drastic reduction of undesirable electron dose and retrieval of de-noised images. Of course, this will be limited to our ability to model the specific form of the noise distribution, which may be non-trivial for next-generation detectors with where the mixed Poisson-Gaussian model breaks down.

2.5   Resolution and Image Quality Concerns

We have also quantitatively examined the effect of sparse imaging through the use of the PSNR, cross correlation coefficients, and Structural Similarity Index Measure (SSIM) in Figure 2.8. For the tin nanoparticle sample there is no obvious drop in PSNR or cross correlation, measuring the similarity of the fully sampled and sparsely sampled images, even down to 20% sampling. The quantitative values also compare well with figures from other "in-painting" and image recovery results [145-147]. Therefore, even at 20% sampling, one can record five images for the same overall dose of a comparable fully sampled image. This method could have notable impact in imaging sensitive structures such as soft biological materials [148], unstable zeolite structures [149], and hybrid soft nanoconstructs [150].
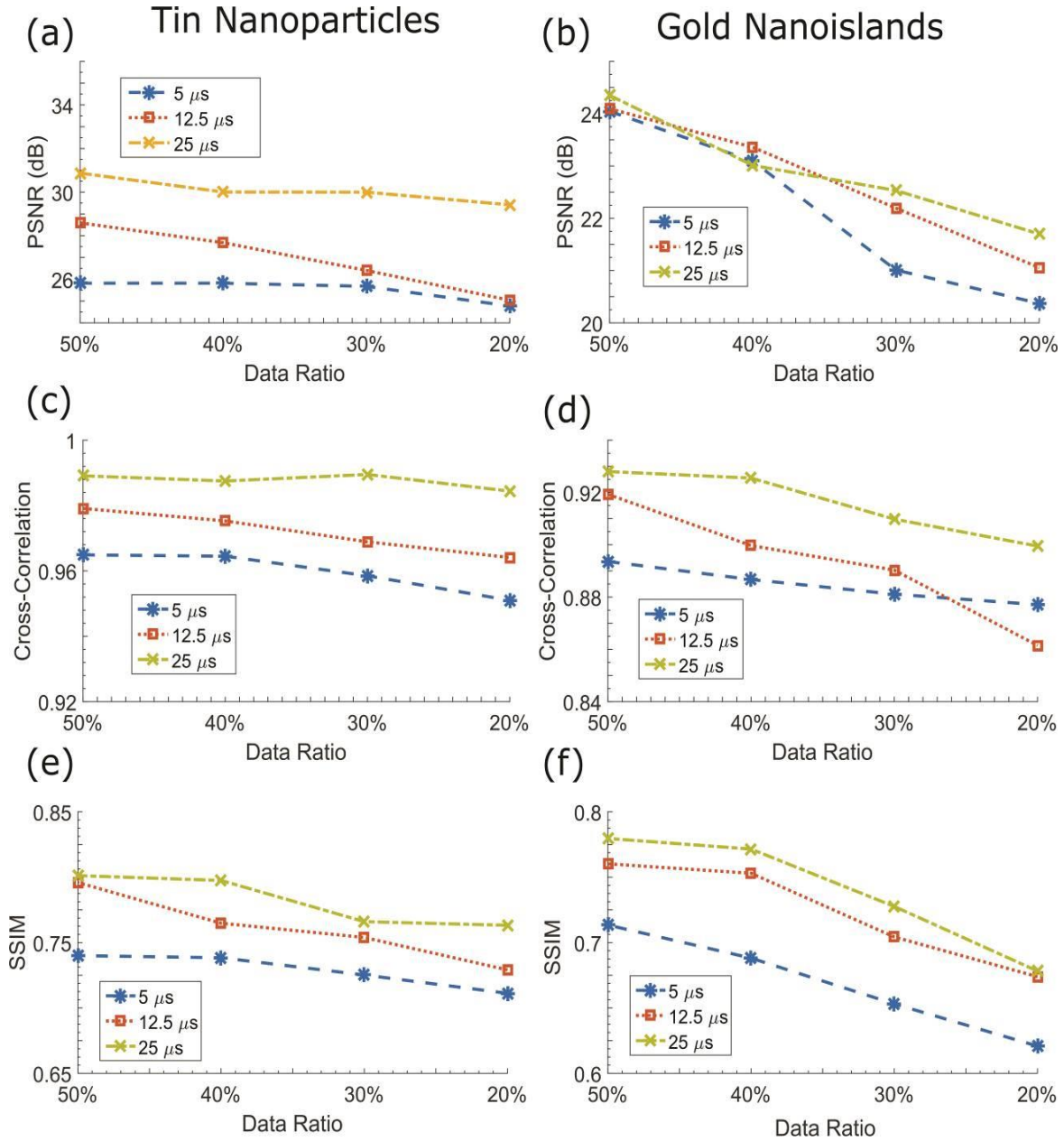
Figure 2.8 (a),(c),(e) The peak signal-to-noise ratio (PSNR), cross correlation coefficients, and structural similarity index measures (SSIM) for the sparse imaging and reconstruction process on

the tin nanoparticle sample with various dwell times and data sampling ratios (percentage of pixels in the full image actually sampled). There is no strong drop of quantitative measures of image quality, even at extremely low sampling rates. (b),(d), (f) PSNR, cross correlation, and SSIM results for the sparse imaging process on the gold nano-island process shows a slight dip in PSNR with decreasing data ratios as to be expected for slightly lower contrast samples. Cross correlation coefficients often vary less than 5% between reconstructions and fully sampled images, showing reconstructions are highly similar with fully sampled images.

The loss of some point-like features is unavoidable in this imaging method, due to the random method of sampling. Features only present in one pixel have a statistically small chance of being sampled by the electron beam, but one is rarely interested in pixel values that share no correlation with nearby pixels. Thus, the suppression of random 'spikey' noise is another advantage of this method, which is usually found when operating at high magnification in a noisy environment. This, again, is particularly relevant to the observation of *in situ* or biological samples, where spiky or line like artifacts can often obscure real information that the sparse imaging process is capable of retrieving. Generally, it appears that sampling more information does not necessarily correlate with a higher fidelity reconstruction. As shown in Figure 2.4, Figure 2.5, and Figure 2.8, a higher dwell time will result in better reconstruction due to the suppression of noise. Despite this, samples with feature sizes many orders larger than the pixel size minimum dwell times are generally acceptable, as seen in the gold nano-island example. For samples with many small features, such

as the smallest tin nanoparticles, increasing the dwell time may be necessary in order to properly sample and reconstruct features that are captured in less than 20 pixels. In general, 30%-20% sampling affords a quality reconstruction for a variety of dwell times and samples, while successfully suppressing many artifacts.

Although it was mentioned in the introduction, this work has not yet discussed the relative trade-offs between under-sampling with relatively high per-pixel doses and fully sampling with low per-pixel doses. It is possible to achieve the exact same area dose in both cases over a fixed field of view and further possible to use the exact same method to either inpaint the undersampled image or denoise the fully sampled image. Much recent work (post-2017) has focused on this tradeoff, with the conclusion being that it's often heavily sample dependent [151, 152]. For samples with highly varying textures of dissimilar features scattered on a non-homogenous background, higher quality image reconstructions can be achieved by fully sampling at low dwell times[152].
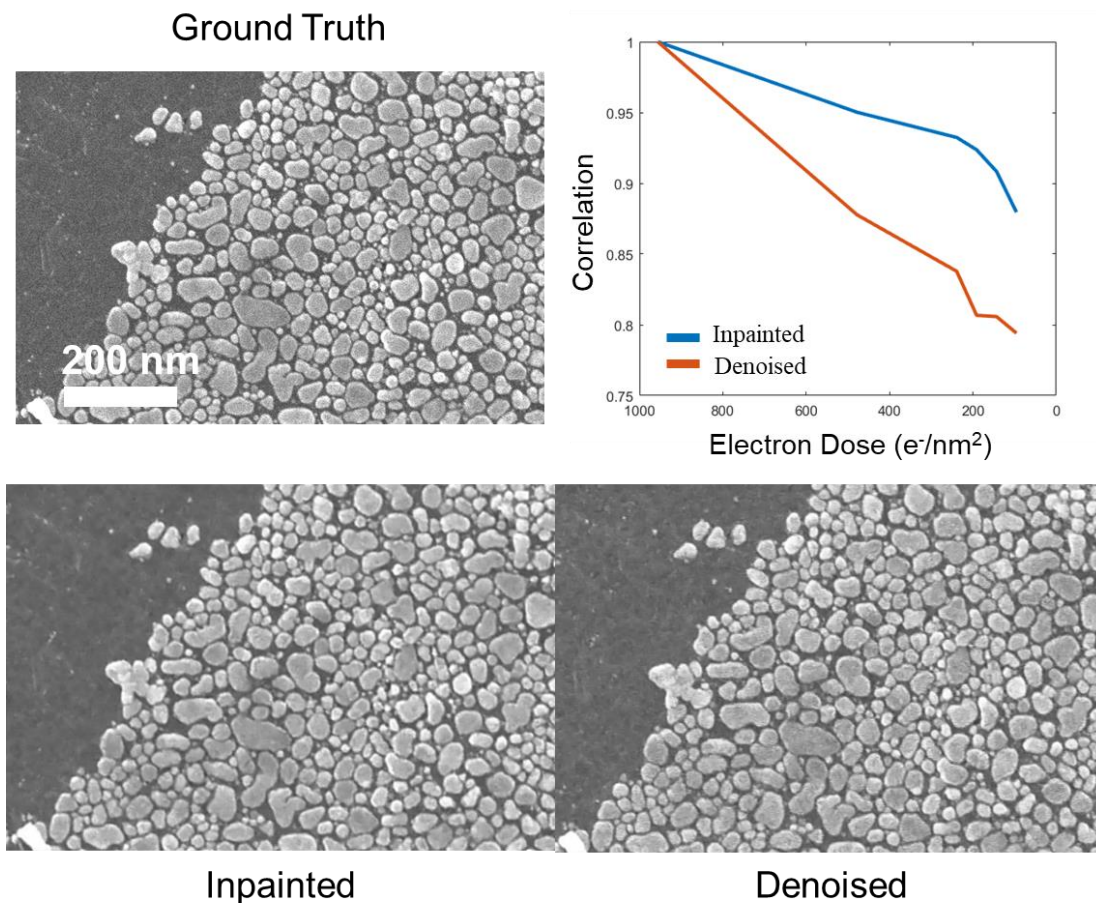
Figure 2.9 A comparison of several experimentally acquired images on the same region of a sample of gold nano-islands acquired in two separate ways. First, a series of under-sampled images were collected at the same beam current. The relative area doses of the under-sampled images were calculated as a function of the total dose experienced by all sampled pixels in the image. Noisier fully sampled images at the same area dose were collected by reducing the dwell time at all pixel (scanning faster). The BPFA algorithm was used to either inpaint the undersampled images or denoise the lower dwell time images. The same number of iterations

were used in both cases and the maximum cross correlation coefficient plotted for the relative electron doses.

In Figure 2.9, a series of images collected in an undersampled form using an experimental beam blanker have been compared to a series of fully sampled images collected at low dwell times. Each pair of images from the two series was collected at an equivalent electron area dose over the same field of view. Excessive blurring from the denoising process at low integrated electron doses results in a lower figure of merit for image quality as compared to the inpainted images. This is likely due to the incomplete modeling of the noise process in electron microscopes, which is often mixed Poisson Gaussian in character. This result is heavily dependent on the nature of the image, much more complicated heterogeneous images frequently will exhibit superior performance through denoising.

While image metrics such as PNSR, SSIM, and cross-correlation coefficient are useful in evaluating the statistical quality of an image reconstruction, as microscopists we care about resolution. The resolution of a reconstructed image can be calculated quantitatively given a ground truth example using the Fourier Ring/Shell Correlation. By integrating the correlation over successive rings (if in 2D) or shells (if in 3D) between two Fourier transformed images/volumes, the correlation as a function of spatial frequency given by the following equations and plotted in Figure 2.10:

$$FC(r) = \frac{\sum\limits_{r_i \in r} F_1(r_i) \cdot F_2(r_i)^*}{\sqrt{\sum\limits_{r_i \in r}\left|F_1(r_i)^2\right| \cdot \sum\limits_{r_i \in r}\left|F_2(r_i)^2\right|}} \tag{2.10}$$

Where r is a corresponding shell/ring in Fourier space, $F(r_i)$ is the complex value at r_i in Fourier Space, and the summation occurs over all Fourier space voxels/pixels r_i in a particular shell/ring.
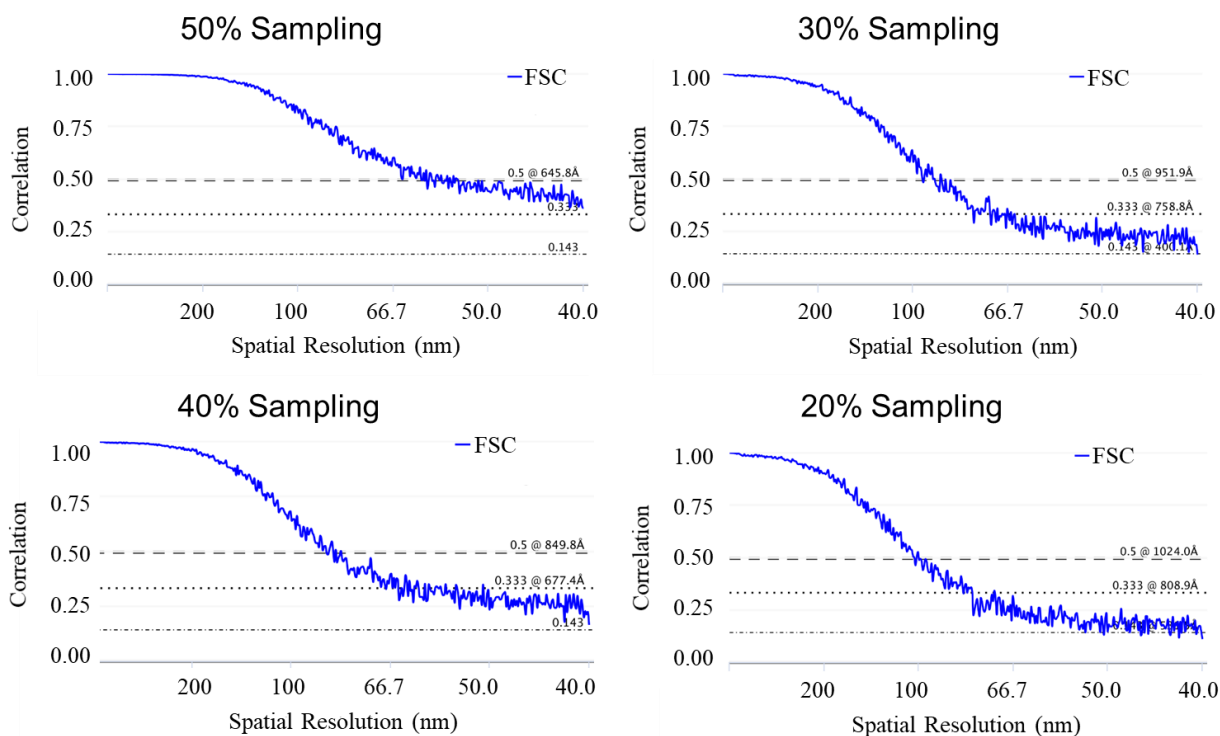
Figure 2.10 Comparison of Fourier Ring Correlation plots comparing reconstructions from simulated undersampling and inpaintings at various sampling rates. These plots give a quantitative

measure of the resolution in the reconstructed image given the dose. Note that at 20% sampling achieves a 55% poorer resolution with a 30% savings in total area dose as compared to 50% sampling, which may not be a favorable trade-off for some specimen.
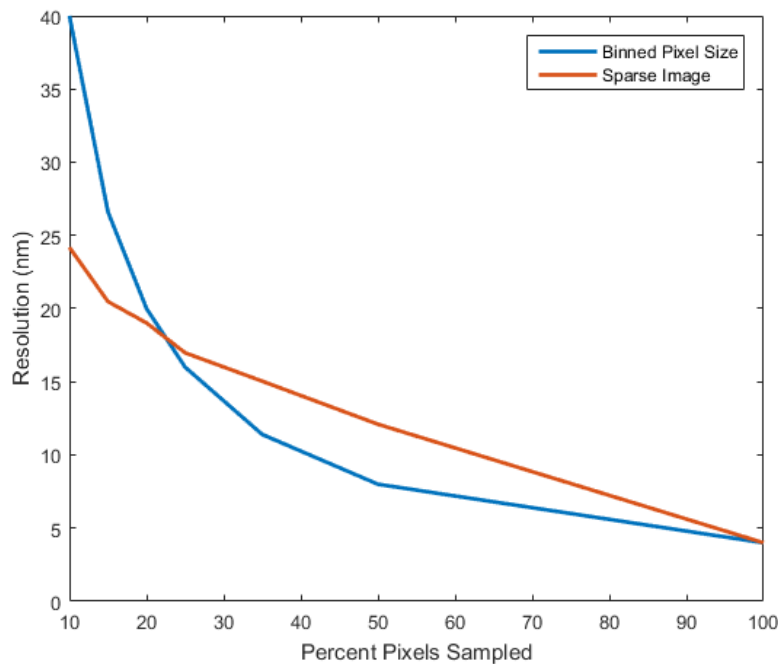
Figure 2.11 The resolution of a undersampled image of the gold nano-islands calculated from the Fourier Ring Correlation plotted against the resolution of a binned fully sampled image acquired at the same area dose. As can be seen, coarsening the scanning mask appears to be highly effective in preserving real 'resolution'. Inpainting and under-sampling appear to help only in the very low-sampling/low area dose cases.

Comparing the resolution between undersampled and fully sampled images tells a somewhat different story however. Binning the overall number of pixels to maintain a lower integrated area dose (at the same dwell time) results in a higher resolution image except at the very lowest sampling rates. For these reasons, undersampling is likely best applied in situations where multiple observations must be made over the same field of view while minimizing the impact of radiative damage. Since it's possible to generate multiple images where each pixel was only visited once, this technique may find applications in *in-situ* and tomographic imaging over day-to-day imaging tasks.

2.6 Summary of Key Results

We have experimentally demonstrated that under-sampling electron microscopy images by up to 80% using an electrostatic beam blanker can still yield high quality images through modern probabilistic machine learning techniques. Such reduced dosage conditions are able to suppress many beam induced artifacts common in sensitive materials, such as polymer/biological structures and in-situ fluidic systems. This allows for up to, and possibly exceeding, four images to be captured for the dose of one fully sampled image; which is a significant reduction in the price of information yielded from a session on a typical electron microscope. The effective application of

this sampling methodology in scanning transmission electron microscopy (STEM) may be very effective, where periodicity in images can be further exploited by such a dictionary learning algorithm, and hyperspectral elemental information can simultaneously be recovered, possibly leveraging the stochastic process of x-ray detection inside the column.

Of particular importance to the field microscopy, the hardware details of this implementation (external electrostatic blanker) are readily accessible to many other microscopy facilities, as there is no need to directly interface with the scan coils of the microscope. This method also allows on the fly switching between full sampling and sparse imaging, and thus may replace the final exposure step in traditional imaging. As is traditionally done, the microscope can be aligned on a nearby area and then jumped to the area of interest, but while also simultaneously switching to sparse imaging in order to capture as unaltered of an image of the feature of interest as possible. Less computationally intensive inpainting approaches than BPFA can then quickly be used to confirm that the feature of interest was indeed captured before performing high quality reconstructions off the microscope.

Further, experiments measuring elemental information in three dimensions (either spatial or temporal) of interfaces and defects in hierarchical nanomaterials that were previously infeasible due to large electron doses may now be possible. Future work will involve in-painting in three dimensions to retrieve correlated elemental information with reduced electron dose, as well as

expanding this method to the reconstruction of three-dimensional electron tomograms. Work will also be carried out expanding this method to cryo-SEM to further explore the imaging of extremely beam sensitive nanostructures not observable through conventional methods. Further, the idea of intentionally sensing incomplete information and its subsequent recovery with Bayesian Machine Learning may have very general applications in other "radiation-based" imaging modes beyond EM, such as x-ray and optical imaging with applications to a wide variety of fields where reduced dosage has practical and technical benefits.

CHAPTER 3: HIGH SPEED/LOW DOSE ANALYTICAL ELECTRON MICROSCOPY WITH DYNAMIC SAMPLING

ABSTRACT

Technological advances in electron microscopy, particularly improved detectors and aberration correctors, have led to higher throughput and less invasive imaging of materials and biological structures by enhancing signal-to-noise ratios at lower electron exposures. Analytical methods, such as electron energy loss spectroscopy (EELS) and energy dispersive x-ray spectrometry (EDS), have also benefitted and offer a rich set of local elemental and bonding information with nano- or atomic resolution. However, spatially resolved spectrum imaging with EELS and EDS continue to be difficult to scale due to limited detector collection angles or high signal background, requiring hours or even days for full maps. The principle and application of a Multi-Objective Autonomous Dynamic Sampling (MOADS) method which can accelerate spectrum mapping in EELS or EDS by over an order of magnitude is presented. Initial guesses about the true spectrum images are constructed as measurements are collected, which allows the prediction of points which contribute information/contrast. In this fashion, an intelligently selected and reduced set of points which best approximate the true spectrum image are autonomously collected on-the-fly to save considerable time and/or radiative area dose. MOADS was implemented as a software add-on to arbitrary commercial Scanning Transmission Electron Microscopes (STEMs) equipped with a Gatan Digital Micrograph (DM, Gatan ©) interface. The efficacy of this proposed method on

several prototypical analytical specimens is demonstrated, as well as dose sensitive materials. It is expected that MOADS and similar supervised dynamic sampling approaches may open the exploration of large area analytical maps or the imaging of beam reactive materials not previously thought feasible.

3.1   Previous Work on Dynamic Sampling

Newer generations of electron microscopes have dramatically increased spatial resolution and analytical sensitivity by *focusing* ever higher electron currents into smaller and smaller volumes [153]. Studies of a wide variety of materials which utilize new high brightness and high coherence electron sources now commonly report atomic resolution imaging and atom-by-atom elemental mapping with Electron Energy Loss Spectroscopy (EELS) and Energy Dispersive X-ray Spectrometry (EDS) [110, 154]. Commercially available MEMS-based sample holders, which can encapsulate the sample in a small volume of controllable fluid or gas, have also become widely available for most microscopes with accessible EDS or EELS signals [155, 156]. Spatially resolved EDS and EELS spectra, referred to as spectrum images (SI), have continued to be applied to the exploration of soft and hybrid soft/hard materials, often answering questions about complex and nanoscale processes un-addressable through other imaging modalities [157, 158]. In contrast to energy

filtered TEM, these spectrum images provide 'fine structure' which can be used to resolve bonding configuration and/or other information about local electronic structure [159, 160].

Although increased radiative fluence with a fixed cross section for signal generation has had analytical advantages [161, 162], the limited detector collection angles for EDS and high background signal in EELS have prevented the routine application of spectrum imaging at reasonable doses/times outside of specialized labs. In particular, the predilection of soft, hybrid, and *in-situ* systems to be damaged under incident radiation has been an unresolved problem compounded by the increasing brightness of modern electron sources [13, 115]. Performing additional correlated measurements after spectrum imaging, such as high-resolution imaging or nano-diffraction, is often impossible due to the distributed area dose involved in conventional spectrum imaging. Larger area or higher fidelity spectrum images of dose insensitive materials also provide challenges, as the hours or days required to complete a full map may exceed the stability of the microscope or specimen. This is especially true for *in-situ* systems, where dynamics often proceed at much faster rates [163, 164]. A significant need exists for improved methods of collecting spatially resolved EELS and EDS signals at area doses low enough for the preservation of sensitive structures or subsequent investigation with a correlated technique, and/or for the acceleration of conventional spectrum images for the investigation of spatially confined biological-inorganic complex structures, engineered hybrid soft/hard ordered materials, or responsive and dynamic reconfigurable nanostructures.

Recently, algorithmic approaches have been proposed to substantially reduce the collection time or radiative dose of conventional electron, x-ray, and other radiation-based probe instruments [165-169]. The central idea of these methods is that there is considerable redundancy in most experimental data, which can be disregarded without loss of fidelity [170]. Sparse imaging involves an *under-sampled* acquisition of the signal in real space (sometimes incorrectly referred to as *compressive sensing*) [169, 171, 172]. This redundancy in combination with prior information is used to impute reasonable values for the missing entries in the image, which potentially reduces the area dose and the acquisition time. It is important to note that in the case of a scanned probe, the local fluence at a single pixel in an under-sampled image is equivalent to the conventional case. However, the reduction in total area dose may allow for the subsequent investigation with a correlated technique on pristine sample in the same region-of-interest or the reduction of diffusing and damaging radical species in *in-situ* systems due to beam-media interactions. Recently, it has also been shown that for small electron probes and particular energy losses, the region of primary energy deposition in which sample damage occurs is smaller than the point spread function (PSF) for inelastic scattering [173]. Sparse or under-sampled EELS acquisitions may therefore take advantage of this property to maximize the volume of signal unperturbed by the beam [73]. So far, in all the cases described above, the scan mask is 'fixed' before observing the specimen and is referred to as static, or non-adaptive.

Instead of pre-choosing which measurements to make, dynamic sampling is performed 'on-the-fly' (also referred to as adaptive). As data is collected from a mobile probe interacting with the specimen, an algorithm uses the previously collected data to predict the next best measurement to make. By intelligently adjusting the position of the probe after each sequential acquisition, an accurate approximation of the true image can be obtained at radically lower area exposures/collection times [174, 175]. Supervised methods based on simple linear regression have also shown strong performance at minimal computational cost (milliseconds) [176, 177]. Simulations on scanning electron microscopy (SEM) EDS images have recently been carried out using a similar approach but have not been followed up with a practical implementation [178]. In addition, this previous work could not map multiple overlapping elements or continuously valued spectrum images (only integer class-based maps) and required the training of a dedicated neural-network for fitting the spectra for each potential sample. A more robust approach based on direct mapping of elements, rather than binned 'material' classes, is much needed for routine applications.
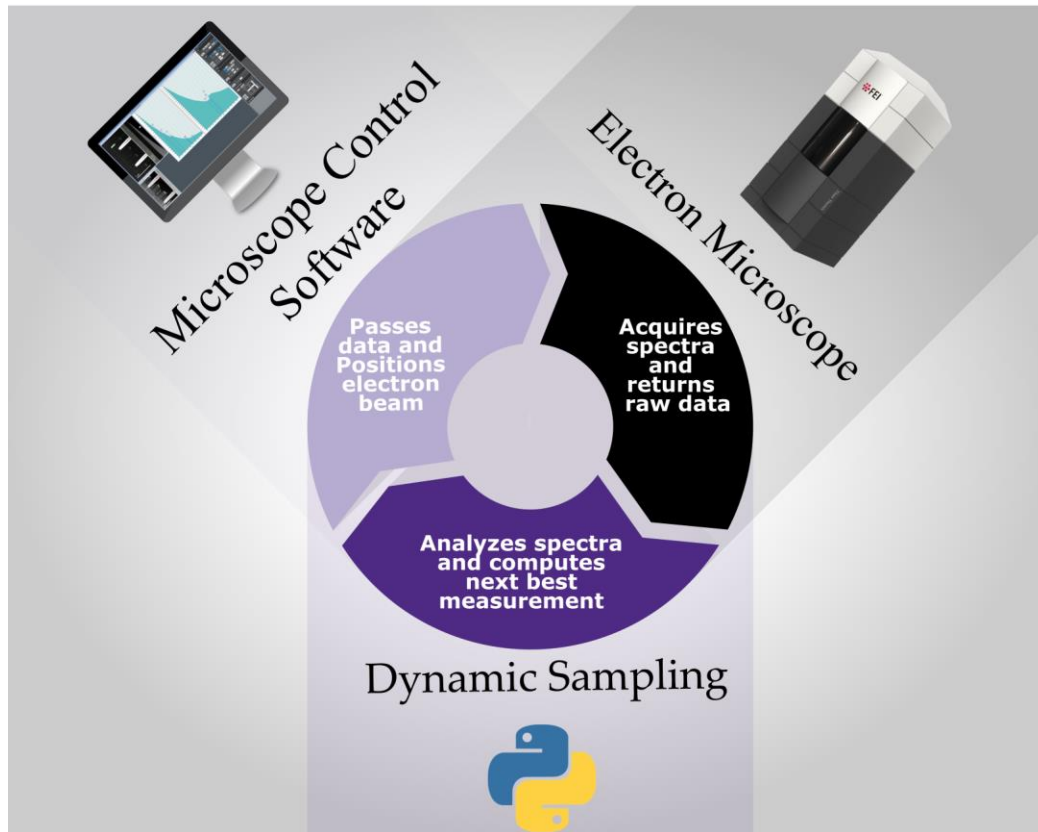
Figure 3.1 A flow chart describing the interaction of MOADS, Digital Micrograph or other Microscope Control Software (TIA Envision, JEM Toolbox, etc.), and the physical microscope. All direct calls to the microscope hardware are made through the manufacturer's control and COM interface, which translates the requested measurement from the dynamic sampling code from relative coordinates to the physical DAC commands to the scan coils. After acquiring a spectrum, the raw data is sent to a support PC running the dynamic sampling code, which analyzes each spectrum and performs the necessary steps to estimate the next best measurement. In this way, the manufacturer software acts as a safety buffer, preventing bad calls to the microscope hardware.

Herein, it will be shown that spectrum imaging in analytical EM is amenable to dynamic sampling, where abrupt interfaces or continuous changes can be mapped with considerably fewer measurements. In particular, the multi-objective form of dynamic sampling allows for independently resolving multiple elements simultaneously, while previous methods relied on classifying groups of signals into discrete classes [177]. Such an approach may potentially allow for very large spectrum images at acquisition times in the minutes, as opposed to hours or longer. In the current rendition, this approach is drop-in ready and autonomously operable on any STEM equipped with a Digital Micrograph (DM®, Gatan Inc.) control system.

3.2   Multi-Objective Dynamic Sampling Formulation

The goal in dynamic sampling will be to minimize the error between a ground truth (the true fully sampled) image X and an approximation $\hat{X}$ by sequentially sampling a reduced set of pixels that best represent the true image. In this section, the relevant terminology and process will be defined in an intuitive fashion, leaving the mathematical formulation for Appendix A.1 and A.2. At any point during an experiment there will be a set of k values sampled from the grid of pixels of X which can be interpolated to form $\hat{X}$. This interpolation will have some error in its estimation X, which is referred to as the distortion between the interpolant and the ground truth $D(X, \hat{X}^{(k)})$. In

this case D is calculated as the cumulative pixel-by-pixel error between the two images. In principle, adding any additional measurement $k+1$ should give us more information about X and reduce the distortion, D. However, it is assumed that some pixels are strongly correlated with their neighbors and thus the reduction in distortion is not uniform for all possible pixels (some pixels contribute more information than others).

If one knew the ground truth image X, the pixel which offers the maximum reduction in distortion could simply be calculated by enumerating through all the possible choices and calculating D directly. During an experiment we do not have access to the ground truth elemental distribution, and thus it is necessary to calculate an *expected reduction in distortion*, or ERD, for all possible pixels to sample.

Our second assumption is that there are some metrics which could describe the reduction in distortion, which are local around each unsampled pixel in the interpolated image. Calculating these metrics, it would then be possible to learn a mapping to the ERD for each possible additional $k+1$ measurement. In the context of Machine Learning, these metrics are described as a *feature vector*, which for MOADS have been listed in Table 3.1. These features, or metrics, are general but powerfully descriptive calculations, such as the local gradient in the interpolated image around that pixel, the variance of the last few measurements near that pixel, or the distance to the nearest measurement. Intuitively, if many measurements are taken locally in a small area and they all

return very different spectra, this is likely an area with fine detail. Similarly, if there are no measurements in a large area of the image, we might like to take a few exploratory measurements.

Measures of Gradient	
$$Z_1 = D(\hat{X}_{s_{x+}}, \hat{X}_{s_{x-}})$$	$$Z_2 = D(\hat{X}_{s_{y+}}, \hat{X}_{s_{y-}})$$
Horizontal gradient in the reconstructed image for adjacent pixels around the potential measurement	Vertical gradient in the reconstructed image for adjacent pixels around the potential measurement
Measures of Standard Deviation	
$$Z_3 = \sqrt{\frac{1}{L}\sum_{r\in\delta s} D(X_r, \hat{X}_s)^2}$$	$$Z_4 = \sum_{r\in\delta s} w_r^{(s)} D(X_r, \hat{X}_s)$$
The difference between the set of closest L measurements and the estimate of the potential measurement	The difference between the closest measurements (r) and the potential measurement (s) weighted by the Euclidean distance:

	$$w_r^{(s)} = \dfrac{\dfrac{1}{\left\|s-r\right\|^2}}{\dfrac{1}{\displaystyle\sum_{u\in\delta s}\left\|s-u\right\|^2}}$$
Measures of Density of Measurements	
$$Z_5 = \min_{r\in\delta s}\left\|s-r\right\|_2$$ The distance between the closest measurement and the potential measurement	$$Z_6 = \dfrac{1+A_{(s;\lambda)}}{1+A^{*}_{(s;\lambda)}}$$ The number of measurements performed in a disk of radius lambda around the potential measurement

Table 3.1 The features used to construct the V matrix. Each of these features is expanded polynomially into a 26 dimensional vector [174, 177]. These features capture information about the structure of the image, such as gradients and local deviations, as well as the history of previous measurements, local density of measured points or distance to last measurement. These features have been shown previously to map un-measured pixels to the expected reduction in distortion (ERD) with high efficiency.

In the case of MOADS, this mapping is learned by providing training images, with which the distortion between an interpolated version and the ground truth image can be calculated exactly. By calculating many local metrics for each unsampled pixel and recording the actual reduction in distortion on making a measurement, many training pairs can be created. Simple linear regression can then be used to provide a set of coefficients which can be used to predict the ERD for an arbitrary set of input metrics. It was important to demonstrate that the success of MOADS on an arbitrary sample does not depend very strongly on the nature of the training images. While one could provide a detailed set of experimental images of the same or similar sample of interest, a series of arbitrary binary shapes produced in a paint application have been used. These are referred to as *weakly informative* training images as they do not on their own give specific information about the fine structure in the experimental images.

In the case of MOADS, for h different elements present in the sample, h different interpolated images are constructed for each element independently. Next, h different ERDs are calculated and the point with the highest joint predicted ERD using the coefficients trained offline is sampled.

In many low-dose conditions, noise or high background can complicate simple fitting and interpolation schema, leading to a very inaccurate estimate of the spectrum image. To fit the spectra and calculate an approximation to the true spectrum image in a time scale on the order of milliseconds straightforward fitting and interpolation methods which do not explicitly account for

noise are used. Thus, in low signal-to-noise ratio cases the algorithm may wind up chasing spurious noise. To avoid these difficulties while still completing the fitting and interpolation on a time scale much faster than the acquisition, the algorithm can map elements in a *discrete* mode, in which the estimated spectrum image is discretized (1s meaning the element is present and 0s meaning its absence).
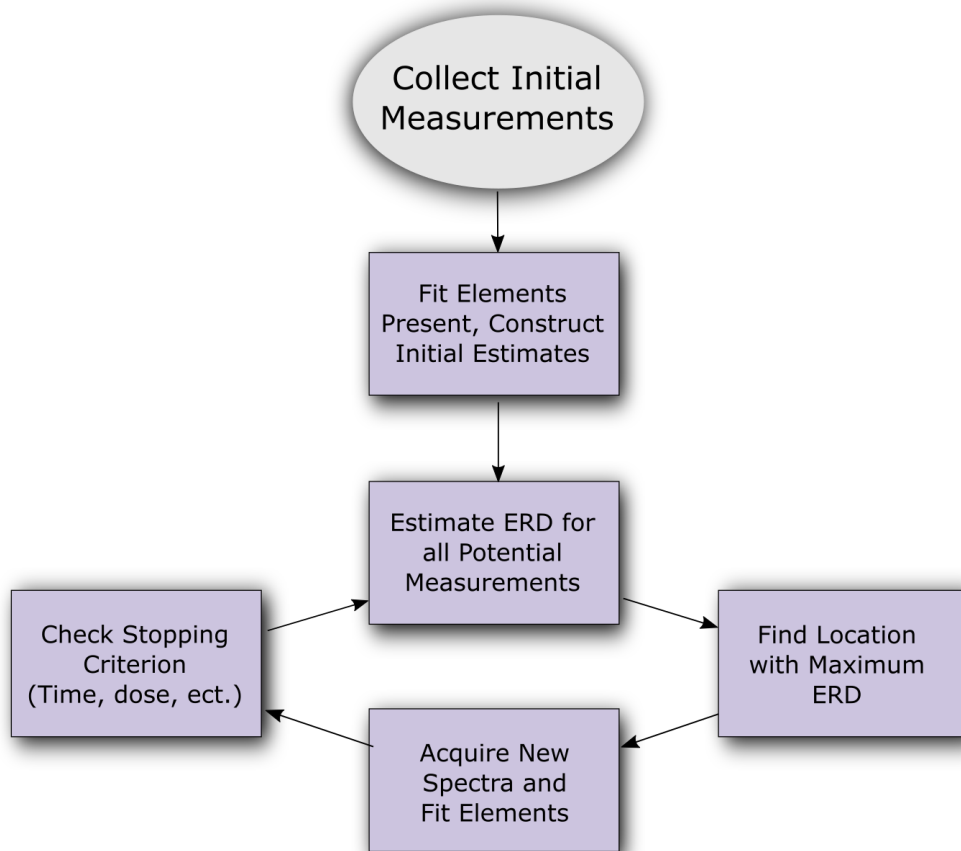
Figure 3.2 Flowchart of the dynamic sampling methodology. First, a small subset of the total measurements is acquired by the microscope uniformly or randomly over the grid of defined pixels. This initial set is used to make a crude estimate of the true spectrum image of the sample, from which expected reduction in distortion (ERD) between the estimate and true image is calculated for each potential measurement. The pixel with maximum ERD is chosen and the appropriate coordinates sent to the microscope for acquisition. The algorithm then incorporates

the information collected and updates its estimation of the spectrum image; repeated until a dose, time, or sampling threshold is met.

Practically, a user sets a region of interest (ROI), the pixel density, loads the pre-trained coefficients, and chooses which elements to map from the EELS spectrometer or the EDX detectors. The algorithm selects an initial measurement set (typically 0.5 to 1 % of the pixels) defined randomly or uniformly and collects the initial EELS or EDS spectra. In this implementation a relatively naïve fitting method was employed, but in principle any advanced fitting or quantification method could be dropped into MOADS to suit the users' preferences as long as a discrete label, continuous count or quantified percentage is returned to MOADS. In this case, each EDS spectrum is fit by integrating pre-and post-peak regions and comparing to the integrated counts in the peak region. If the peak counts were more than three times the pre-and post- peak counts, the peak count value was returned to MOADS (if operating in continuous mode) or a discrete label (if operating in a discretized mode). In the case of EELS, the classic three-window method was used by fitting the pre-and post-edge region after a log transform and integrating the remaining peak counts after background subtraction. Every spectra is saved separately in a raw format, enabling more advanced fitting offline in commercial packages or free modules [179].

Using these values and their locations, a crude estimate of the spectrum image for each element is made through inpainting, and features are extracted for each un-sampled pixel (as done during training). Multiplying the features and pre-trained coefficient vector results in a predicted ERD for each potential measurement. The algorithm then automatically directs the microscope to acquire a new spectrum at the pixel with the maximum ERD. Using this new information, the estimates of the sample are updated, and this process continues iteratively until a preset time or area dose threshold is exceeded, or when the estimated spectrum image remains unchanged from sampling additional points.

3.2.1 Mathematical Formulation for Single Objective

The goal of dynamic sampling is to choose measurements from a set of available choices which cumulatively best approximate the true measurement. In this case, these measurements are made sequentially such that at each iteration a desired pixel from the set of unmeasured pixels which has the maximum expected reduction in distortion (ERD) is chosen. First consider making k measurements at s locations with $X \in R^N$ values:

$$S^{(k)} = \begin{bmatrix} s^{(1)}, X_{s^{(1)}} \\ \vdots \\ s^{(k)}, X_{s^{(k)}} \end{bmatrix},$$
(3.1)

Where $S^{(k)}$ is a vector containing all the previous individual measurements. $S^{(k)}$ can construct $\hat{X}^{(k;s)}$, the approximation of X after sampling k measurements. The distortion, or difference, between $\hat{X}^{(k;s)}$ and X is $D(X, \hat{X}^{(k;s)})$. This is estimated as the pixel by pixel summed difference between the ground truth and the estimate:

$$D(X, \hat{X}^{(k;s)}) = \sum_{r \in \Omega} D(X_r, \hat{X}^{(k;s)})$$
(3.2)

After making an additional measurement, $k+1$, the reduction in distortion is effectively the change in $D(X, \hat{X}^{(k;s)})$ before and after measuring $k+1$.

$$R^{(k;s)} = D(X, \hat{X}^{(k+1;s)}) - D(X, \hat{X}^{(k;s)})$$
(3.2)

In most cases, the ground truth map or image, X, is unavailable, so the *expected reduction in distortion* (ERD) will be computed:

$$\tilde{R}^{(k;s)} = \mathbb{E}\left[R^{(k;s)} \mid S^{(k)} \right]$$
(3.3)

The next measurement $k+1$ which has the maximum value of ERD of all unmeasured pixels will be sampled:

$$s^{(k+1)} = \underset{s\in\Omega}{\operatorname{argmax}}(\tilde{R}^{(k;s)}) \tag{3.4}$$

In the supervised approach for dynamic sampling, the ERD values for all unmeasured pixels are predicted by mapping features from $\hat{X}^{(k;s)}$ to the ERD value for each pixel linearly:

$$\tilde{R} = f^{\theta}(V) \tag{3.5}$$

Therefore, for n un-sampled pixels in an image, there is an n-dimensional vector $\tilde{R}$, and an n by m dimensional matrix for V, where m is the number of features extracted for each pixel. Features include local gradients around the un-sampled pixel in the estimated image and the distance to the nearest measured pixel, among others (see Table 3.1).

$$\tilde{R} = \begin{bmatrix} R^{(s_1)} \\ \vdots \\ R^{(s_n)} \end{bmatrix}, \quad V = \begin{bmatrix} V^{(s_1)} \\ \vdots \\ V^{(s_n)} \end{bmatrix} \tag{3.6}$$

To learn the coefficients (f^θ), a user provides a set of *training* images, which have similar features as the experimental images. Many values for R and V are populated from these *training* images and the coefficients, $\hat{\theta}$, are then estimated using simple linear regression:

$$\hat{\theta} = \arg\min \left\| \tilde{R} - V\theta \right\|^2 \tag{3.7}$$

The training process has been described in detail previously [174, 177], and will not be repeated here. Once the coefficients have been learned the next measurement is chosen by taking the pixel with the maximum approximated ERD, from linearly multiplying the feature matrix times the coefficients:

$$s^{(k+1)} = \underset{s \in \Omega}{\operatorname{argmax}}(V_s^{(k)}\hat{\theta}) \tag{3.8}$$

Each time an additional measurement is to be made, the estimated image $\hat{X}^{(k;s)}$ is re-calculated, and the V matrix populated for each remaining un-sampled pixel. Importantly, it will be shown in the following text (along with previous literature) that the technique is relatively robust to *"weakly informative"* training images, in which the training images provide little or no specific information about the sample structure.

Performed without a heuristic for $\tilde{R}$, each training example would involve one complete inpainting step to compute the actual reduction in distortion between the ground truth map and the estimated map. This would be computationally prohibitive to produce many training examples, so instead the reduction in distortion is calculated only for a small window around the candidate pixel using the following gaussian heuristic:

$$R_r^{(s)} \gg h_r^{(s)} D(X_r, \hat{X}_r) \tag{3.9}$$

$$h_r^{(s)} \approx \exp\left\{ \frac{-c}{2(\sigma^{(s)})^2} \|r - s\|^2 \right\} \tag{3.10}$$

$$\sigma^{(s)} = \min_{t \in P}\{\|s - t\|\} \tag{3.11}$$

The parameter c is self-estimated during training as reported previously [176, 177].

3.2.2 Extending to Multiple Objectives

Previously, supervised dynamic sampling only considered the possibility that each pixel in the grid had membership with only one class or signal (ie, each sampled point, $s^{(k)}$, has one and

only one value, $X_{s^{(k)}}$). In real materials, elements may be distributed in conflicting ways that may not be amenable to single class classification. Particularly, projection style measurements in S/TEM may involve the transmission of the beam through multiple elements or classes of distinct materials. Thus, it would be preferable to optimize the order of measurements for each map independently and simultaneously, sharing a common coordinate set.

In Multi-Objective Autonomous Dynamic Sampling (MOADS), each un-sampled point has an h length vector $X_{s^{(k)}}^h$ which stores the values measured at coordinate k for all h maps. The ERD is and features for each n un-sampled point in each h map independently are estimated and collated into two large matrices, $\tilde{R}$ and V, where each un-sampled point has a vector of possible ERDs and a 2D matrix of V features from each h map.

$$\tilde{R} = \begin{pmatrix} R_1^{(s_1)} & \cdots & R_h^{(s_1)} \\ \vdots & \ddots & \vdots \\ R_1^{(s_n)} & \cdots & R_h^{(s_n)} \end{pmatrix}, \quad V = \begin{pmatrix} V_1^{(s_1)} & \cdots & V_h^{(s_1)} \\ \vdots & \ddots & \vdots \\ V_1^{(s_n)} & \cdots & V_h^{(s_n)} \end{pmatrix}, \tag{3.12}$$

The columns of $\tilde{R}$ and V shares a common set of measurable coordinates, but which have separate X_s values, ERDs, estimated images, and feature vectors. Training and experiments proceed exactly

as described previously for each h map separately. In principle, it is possible to simultaneously map elements with very different features or distributions by training a custom $\hat{\theta}_h$ for each element, fully exploiting the prior knowledge about the sample characteristics (plasmon mapping, core loss vs. low loss, EELS vs. EDS). The next coordinate is selected as follows:

$$s^{(k+1)} = \underset{s \in \Omega}{\operatorname{argmax}} \left(\sum_h V_h^n \hat{\theta}^h \right) \tag{3.13}$$

The point, $k+1$, with the maximum joint ERD across all the maps is chosen. Rather than choosing the best point for each h map separately and sequentially, this joint ERD results in a more efficient application of dose across all the maps (see following sections). Each element's estimated map is then updated using the information from $(s^{(k+1)}, X^1_{s^{(k+1)}}, \cdots, X^h_{s^{(k+1)}})$ and $\tilde{R}$, V updated for all n and h. It becomes unnecessary to assign each spectrum, which may be composed of multiple elements, into one class. Thus, multiple elemental maps (for as many elements or signals as are present) may be constructed and imaged simultaneously.

3.2.3 Computational Resources

In this work, a Digital Micrograph (DM®, Gatan Inc.) script was developed to interface the python implementation of MOADS with the microscope. Relative coordinates on a grid are sent over the

network to the computer hosting DM®, which receives and converts these commands into DAC voltages for the scan coils on the microscope. Each spectrum is automatically collected and returned over the network to the support PC hosting the dynamic sampling code, which fits and analyzes the spectra. This process is iterated until a preset sampling threshold is met, the area dose limit for the materials is met, or the estimated spectrum map converges. As Digital Micrograph is relatively hardware agnostic and implemented on most analytical STEMs, it is expected that this method will generalize well. Simulations and experiments were performed on a commercial laptop computer equipped with a Core i7 processor and 16 Gb of memory.

3.2.4 Microscope and Specimen Detail
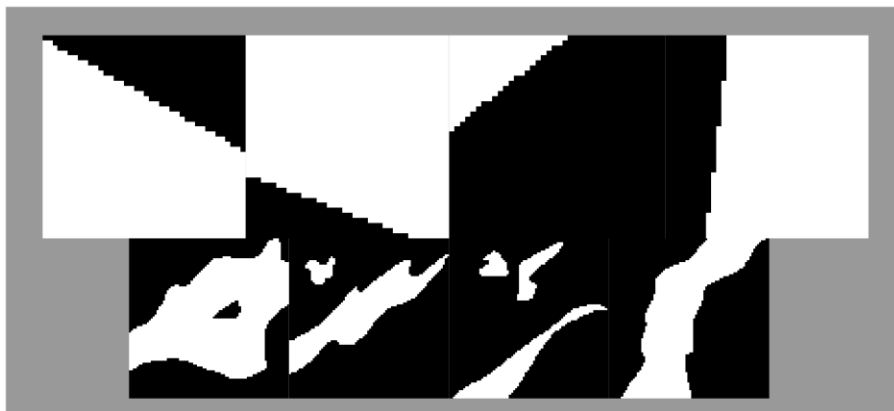
Figure 3.3 Training images used to construct the coefficient vectors for populating ERD matrices in the experiments and simulations used in this paper. **Top Row**: The selection of four basic straight-line interfaces used to construct the coefficients used in all experiments and simulations

except for the Gallionella results. **Bottom Row**: Abstract art pieces produced by the author for the creation of coefficient matrices able to follow more complicated interfaces. Only these four images were supplied to the algorithm for all experimental results involving the *Gallionella* bacterial sample.

EELS experiments were performed on a Hitachi HD2300 dedicated STEM equipped with a Gatan Enfina EELS spectrometer. The microscope was operated at 200kV with convergence angle range 5-24 mrad and collection angle range 7-30 mrad. EDS experiments were carried out on an FEI Titan TEM/STEM equipped with an image corrector and single EDAX Si(Li) detector in STEM mode at 300kV, condenser aperture #2 200mm, and probe size of 5 (probe current ~ 250 pA). In both cases, spectral acquisition was controlled through DM®. Flakes of Fe_3O_4-MoS2 were drop casted onto a carbon membrane grid prior to imaging. The suspended boron nitride flakes on holey carbon film was obtained from Gatan as a reference specimen for the testing and calibration of the Enfina EELS spectrometer. There is increasing interest in exploring the distribution of elements in soft-matter, particularly in the case where hard and soft material intersect, referred to as *hybrid* materials. In this vein, Gallionella spindles were chemically processed with aldehydes and osmium tetroxide followed by dehydration and infiltration with resin for ultramicrotomy. Binary Ti-Al films with nominal composition Ti-48 at. % Al were deposited using magnetron sputtering

according to a previously published paper and annealed at 823 K for 10 minutes [180]. Samples were mechanically grinded, dimpled, and ion milled to produce a thin foil for imaging.

3.3   Simulated Dynamic Sampling Results

We first conducted an experiment offline using a fully sampled spectrum image of molybdenum di-sulfide flakes supporting a collection of magnetic iron oxide nanoparticles.   These materials have been explored due to the multifunctional nature of combining super-para-magnetic nanoparticles with the unique electronic and optical properties of 2D MoS_2. The fully sampled spectrum image was kept in memory and the MOADS algorithm sequentially observed spectra from the grid of available measurements. In Figure 3.12, image quality between dynamic sampling and random sampling with two different reconstruction methods are compared (the same Nearest Neighbor Mean inpainting used in MOADS and a state-of-the-art patch based inpainting method [181]). Patch-based methods have been used in many earlier under-sampled electron microscopy methods due to their strong performance at low sampling rates [167]. However, patch-based methods rely on their being at least one entry in every overlapping patch in the image and will perform poorly if large portions of the image are unsampled.
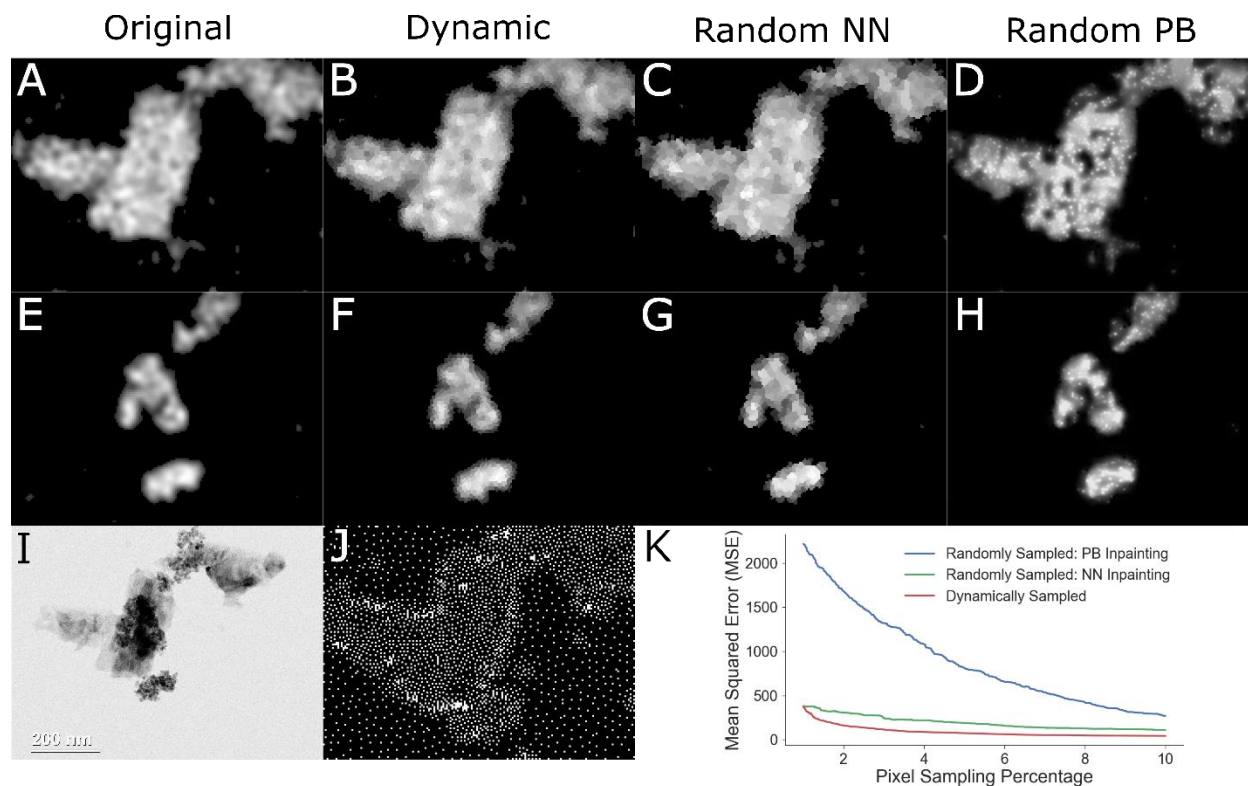
Figure 3.4 Simulated MOADS experiment from a fully sampled EDS spectrum image of molybdenum di-sulfide (MoS$_2$) flakes decorated with iron oxide (Fe$_3$O$_4$) nanoparticles collected on a Hitachi HD2300 STEM. A. Processed molybdenum K$_\alpha$ spectrum map showing strong agreement with the distribution of the flakes in bottom left panel (132,156 pixels). B. Simulated dynamically sampled molybdenum map restored with nearest-neighbor mean inpainting after iteratively sampling 10% of the pixels. C. Nearest-neighbor mean interpolation of a random grid of 10% of the pixels from the molybdenum map, and D. Patch based interpolation of the same random set of pixels. E. Additional experimental processed spectrum map of iron K$_\alpha$ from the

same region of interest. (F-H). Dynamically sampled iron map, randomly sampled 10% with nearest-neighbor mean interpolation, and with patch-based inpainting. I. Bright-field STEM image of the region of interest, showing the thin MoS_2 flakes decorated with darker patches of agglomerated iron oxide nanoparticles. J. Both the iron and molybdenum maps were sampled and interpolated simultaneously for dynamic sampling simulations, resulting in a single scan mask. White pixels represent a grid point at which the algorithm simulated the collection of a spectra, and black represent skipped pixels. K. The joint mean-squared-error (MSE) for the three collection methods: dynamic sampling + nearest neighbor (NN) inpainting, random sampling + nearest neighbor (NN) inpainting, and random sampling + patch based (PB) inpainting.

The results of the simulated experiment with 10 percent sampling can be seen in Figure 3.4, showing the experimentally collected images and the reconstructions after simulating acquisition with MOADS. As can be seen from the scan mask in Figure 3.4 J, the MOADS approach has prioritized the collection of measurements on the flakes and particles themselves, balancing the collection of both iron and molybdenum specific information simultaneously. Strong agreement between the MOADS results for iron and molybdenum and the original ground truth maps is quantified by the relatively low MSE, which drops quickly after the initial 1% sampling rates. Random sampling with nearest-neighbor inpainting reconstructs the rough shape of the object but doesn't produce the fine detail or exploit new data, resulting in slow improvement. On the other

hand, random sampling with patch-based inpainting improves very quickly but still cannot handle the large gaps in information at these low sampling rates.

To understand the practicality of this dynamic sampling approach on common instruments, sthe time to perform one iteration as a function of different mapping parameters was simulated. In Figure 3.5, the time to perform an image has been examined as a function of the overall pixel count in the image. For small maps, this time is on the order of the time required to pass desired coordinates from Digital Micrograph (DM) scripting interface to the Digiscan control box, and for the scan coils to re-position the beam (~ 1 ms). For larger maps, the time to complete one iteration of the dynamic sampling process is still more than an order of magnitude smaller than the acquisition time for typical EELS and EDS spectra (~100-500 ms). Notably, the time to complete one loop actually increases with the number of sampled pixels. This is because many of the features are calculated for the set Ω of nearest sampled pixels. As more pixels are sampled, more distance calculations are required. Using an approximate nearest neighbor search instead of brute force would likely improve performance at higher pixel densities, as well as using more powerful workstation grade computational systems.
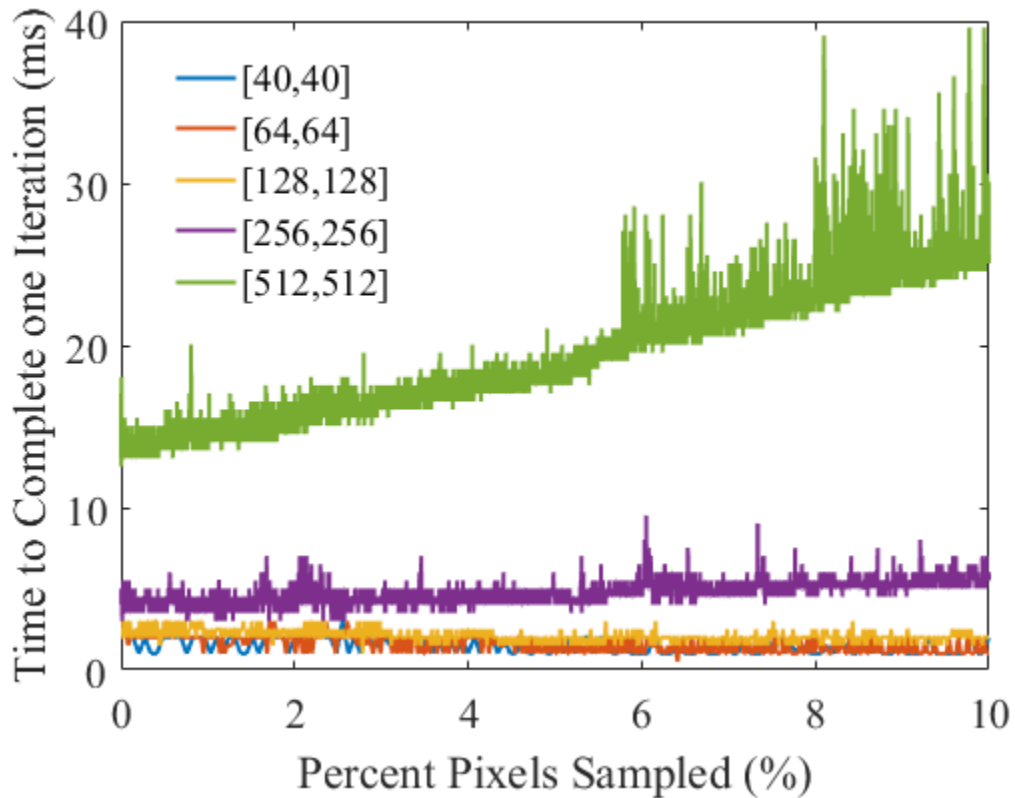
Figure 3.5 The time required restore missing entries in the spectrum image and estimate the next best pixel as a function of the grid size for several common choices.

For a naïve implementation with no parallelization, the impact of adding additional mapping objectives on the total time to complete one iteration was compared (updating the estimated spectrum image and predicting next best measurement). With no parallelization, in Figure 3.6, it can be seen that the total time to feed in new coordinates is still much less than a typical dwell

time for EELS/EDS. Parallelization is relatively simple to implement, since although multiple objectives share the same relative mapping coordinates, the entire ERD calculation is based solely on the portion of the measurement relative to that map (predicting ERD for a Boron edge does not depend on a carbon edge in an EELS map). Thus the calculations associated with each objective can be performed completely independently, with the shared joint ERD calculation (a weighted average) the only shared calculation.
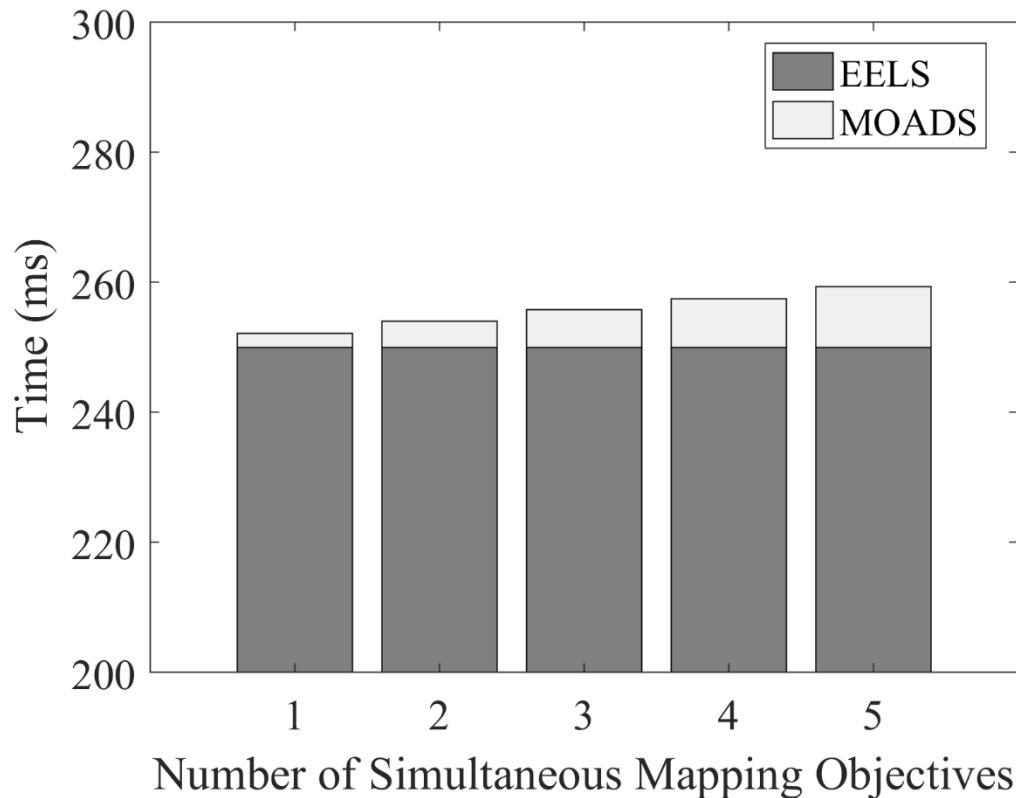
Figure 3.6 For a [128,128] map the time to execute one iteration of MOADS as a function of h, the number of simultaneous mapping objectives, is compared. Even for five separate objectives, the time to perform the estimation is still an extremely small fraction of the total time to complete one experimental loop, due to a 250 ms EELS acquisition time. Note shifted Time scale, otherwise the computation time from MOADS would be unnoticeable in the graph. Simulations were performed on a commercial laptop computer equipped with a Core i7 processor and 32 Gb of memory.

Next, the specific form of the multi-objective ERD was examined by comparing the effectiveness of two different strategies: (1) sample the point with the maximum total ERD across all maps and (2) sequentially choosing the best pixel for each individual map independent of the others. Figure 3.7 shows the result of a simulated Boron Nitride flake on a straight carbon support. As can be seen, with strategy (1) the algorithm has allocated more measurements along the more complicated polygonal shaped BN surface, while allocating less time to the more easily recoverable carbon/vacuum surface. Comparing the final inpainted BN flake for strategy (1) and (2) in Figure 3.7 F and H, respectively, it can be seen that strategy (1) results in a much less rough approximation of the true surface. The final plots of the actual ERD as a function of sampling show this effect, where for strategy (2) it quickly oversamples the simpler carbon surface.
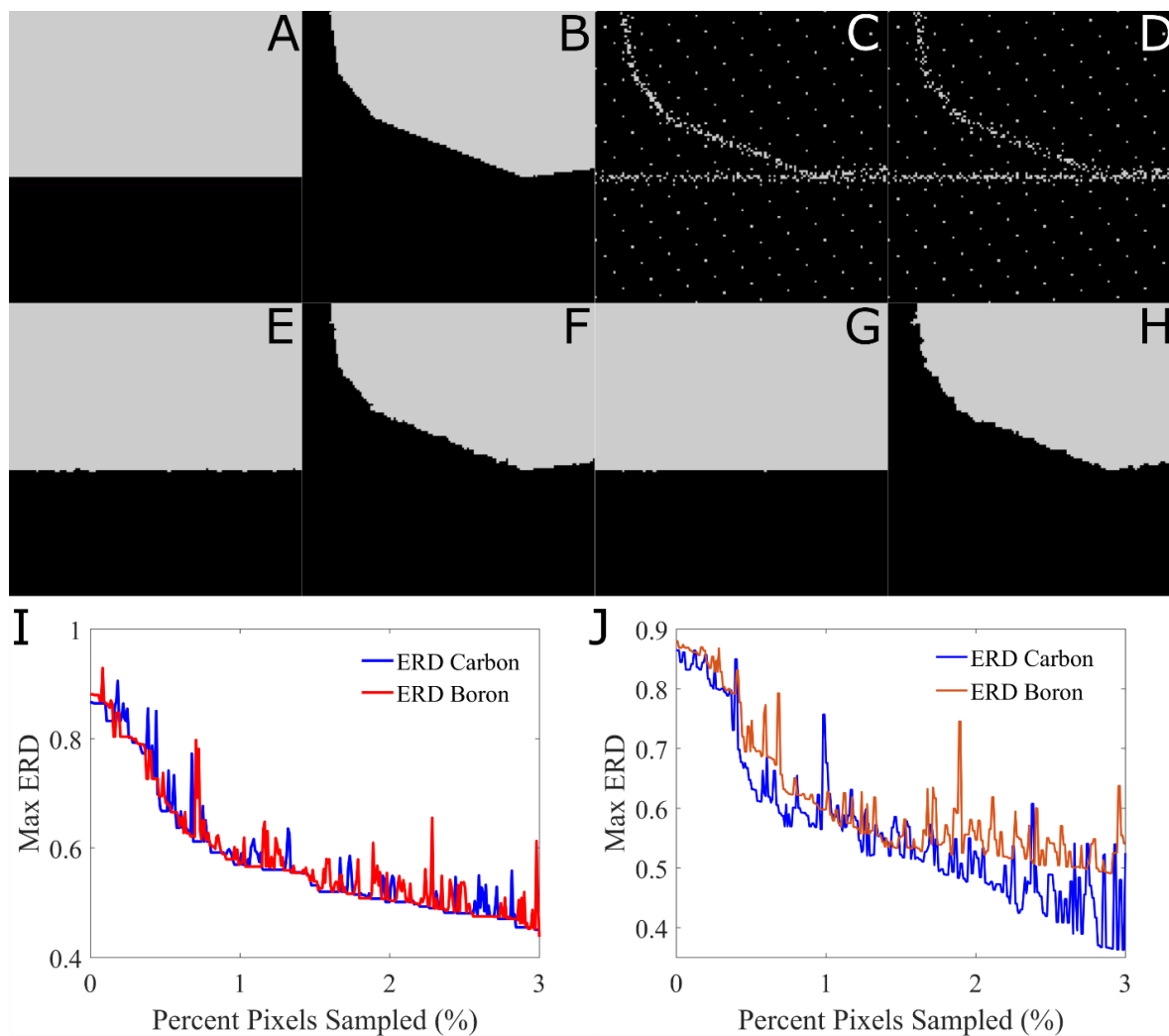
Figure 3.7 The effect of the joint ERD calculation is examined by simulating a straight line between a carbon support (A) and vacuum, and an angled polygonal boron nitride flake (B). Consider the simulation of two different multi-objective sampling strategies: (1) sample the point which gives the most information about both maps (best average ERD) and (2) sample the best point for each map independently, iterating back and forth between the best for carbon and the best

for boron. In the mask for scheme (1) in panel C it can be seen that the algorithm has spent more time sampling the complicated BN interface and less time the simple C line, as compared to scheme (2) in panel D. In the reconstructed maps for scheme 1 in panels E,F, it can be seen that the boron map is comparatively better reconstructed as compared to the reconstructed maps for scheme 2 in panels G,H. Plotting the maximum ERD at each iteration for the boron nitride and the carbon maps it is shown that for scheme (1) in panel I, the ERD for BN and C decreases together. However, for scheme (2) in panel J, the ERD diverges between the complicated BN and C maps.

Thus, scheme (1), which is used in MOADS, allows the algorithm to allocate dose dynamically as a function of the total complexity of each map. After 3% sampling, scheme (1, MOADS) had 52 mislabeled pixels, as compared to 61 mislabeled pixels for scheme (2).

3.4 Experimental Results on Commercial STEMs

Having demonstrated the potential benefit, an experimental spectrum mapping of boron nitride flakes on lacey carbon was conducted, which is a classic specimen for the validation and calibration of EELS spectrometers. These thin flakes provide well resolvable boron and nitrogen edges and are stable under the high exposures common to EELS measurements. Both the carbon

support and the BN flakes provide highly distinguishable interfaces, in which it is possible to examine the effectiveness of the dynamic sampling approach for autonomous EELS collection, and the balancing of multiple experimental objectives. As in this system, and in many other relevant materials, elements may have highly overlapping or uneven distributions. A simple approach to classify each region separately will fail to resolve overlapping interfaces in transmission electron imaging [177]. Thus, it is essential to be able to balance multiple objectives when performing an adaptive or dynamic spectrum imaging technique.
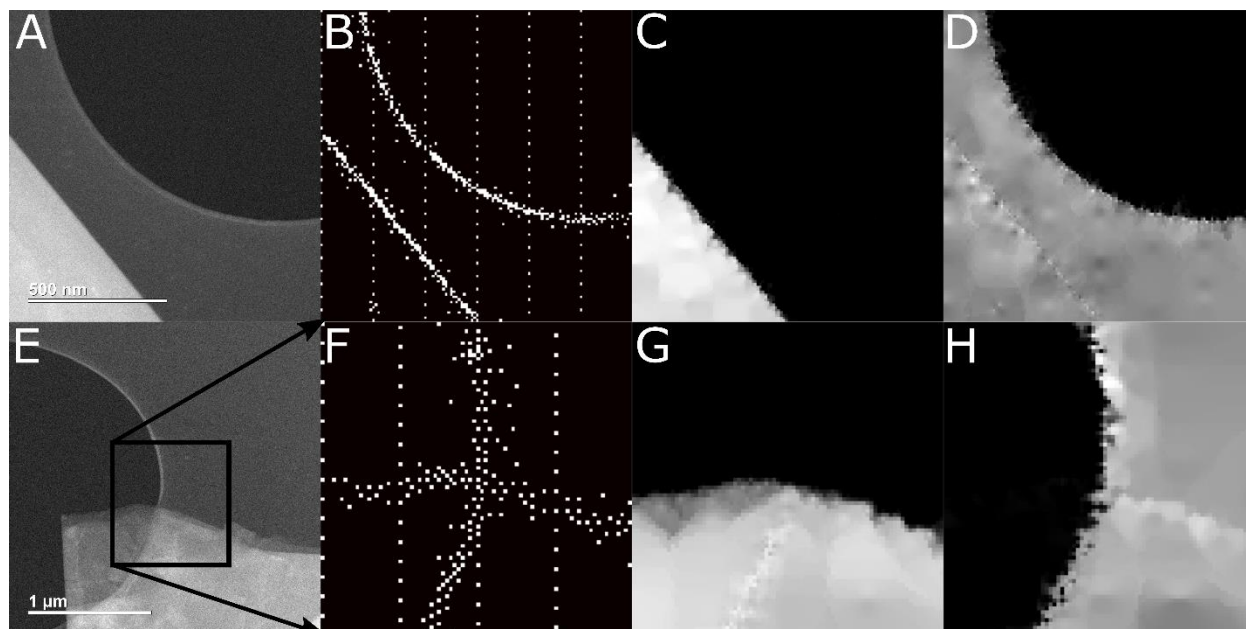
Figure 3.8 Experimental MOADS acquisition of boron nitride flakes on a lacey carbon film using EELS. A. HAADF image of a boron nitride flake supported by carbon film, adjacent to vacuum

on Hitachi HD2300 STEM with Gatan Enfina Spectrometer (convergence angle: 8 mrad, collection angle: 21 mrad). B. The final mask of points imaged autonomously by the microscope, white pixels representing sampled and black skipped. 4% of the total pixels of the 120x120 spectrum image were collected in 9.6 minutes compared to 4 hours for a full spectrum image, with an initial 1% sampled uniformly. At each pixel a separate boron and carbon spectra were captured, each with an exposure of 0.5 seconds and a dispersion of 0.1 eV/ch. C. Reconstructed boron map from the measured spectra in B of the area in A. D. Similar carbon map from the measured spectra in B of the area in A. E. An additional area of boron nitride flake in which the boron signal overlaps with the carbon and the vacuum. F. Sampled spectra from the inset in E, 5% of an 80x80 grid of spectra were collected in a total time of 7.5 minutes vs. 2.3 hours for a full spectrum image. G. Reconstructed boron and H. carbon maps. In all maps, the zero-loss peak was used to roughly normalize the counts for differences in sample thickness.

We examined several regions with a distinguishable edge between the carbon film, BN flake, and the vacuum. In Figure 3.8 two distinct MOADS resolved EELS spectrum images are displayed, where at each pixel the drift tube was varied to collect a carbon and a boron edge. The user aligned the microscope and centered the desired region, but the mapping was performed fully autonomously. In this case, one percent of the total number of pixels was sampled uniformly to make an initial guess about the sample structure. This initial sampling scheme can also be

performed randomly, or potentially initialized from the gradient of the HAADF image (so-called Z-contrast). In this case, a uniform sampling scheme was chosen as it is reproducible and provides little initial sampling bias, giving no extra information about the curved or diagonal interfaces in the true specimen spectrum map. In addition, this avoids a situation where elements with similar Z but distinct spectra may be missed.

Despite this, as seen in the left most panels of Figure 3.8, the true interfaces are well captured at very small sampling percentages; even just 4% of the pixels in the top map is enough to quickly resolve the angled BN flake edge and the sloped interface between the carbon and vacuum. In addition, where interfaces may overlap, as is the case in the middle inset of Figure 3.8, the multi-objective formulation is able to apportion time and dose efficiently to distinguish the two overlapping interfaces independently from a shared set of pixel coordinates. In this case, the influence of changing thickness on the total counts was accounted for by normalizing against the zero-loss peak. Instrumental errors and drift complicate this procedure and result in a slightly higher contrast region at the BN flake interface in the carbon map, but this problem is ubiquitous in spectrum imaging of samples with discontinuous jumps in thickness with EELS and is not due to MOADS.

Training images used in these experiments involved simple straight lines separating areas of one element from another (binary images separated by sharp interfaces). The same coefficients were used to estimate ERD_{BN} and ERD_C, although it is possible to use specialized coefficients for each

element or to train explicitly for curved interfaces. This is typically unnecessary since the features used to predict the ERD are calculated on a pixel-by-pixel basis and are therefore robust to large scale features in the image. In all experiments reported in this paper, similar *'weakly informative'* training images have been used to demonstrate the generalizability of the method.

In addition to reducing the time-to-image, reducing the number of measurements can also substantially reduce the overall area dose. Below, a biologically relevant sample is shown where spectrum imaging would conventionally struggle to perform using a single EDS detector due to poor efficiency and long dwell times, which can quickly accumulate into a destructive area dose. *Gallionella* bacteria are unique organisms that have developed a metabolism utilizing oxidation of iron. These bacteria form biofilms in iron-rich environments such as freshwater springs, oceanic hydrothermal vents, or deep within the Earth's crust along redox gradients. They are also of interest in the *astrobiology* community, where such bacteria are a focus in the study of possible extraterrestrial life, particularly where harsh conditions and iron abundant environment coincide (asteroids, rocky planetoids, Mars, etc.).

In Figure 3.9 an autonomous dynamic spectrum mapping of a thin section of the spindle-like residue these bacteria has been performed. Traditional HAADF images of these mixed carbon and iron spindles are shown in Figure 3.9, where a dense core of iron is surrounded by a more sparsely packed distribution of iron oxide nanoparticles. Sampling was performed as described above, where the Fe K_α peak was recorded at each pixel position following an initial random 1% sampling

mask. Due to the inefficiency of the single detector, this experiment was performed in a discretized form, where each spectrum was classified into a binary feature (1s representing iron, and 0s representing no visible peak by comparing against the background).
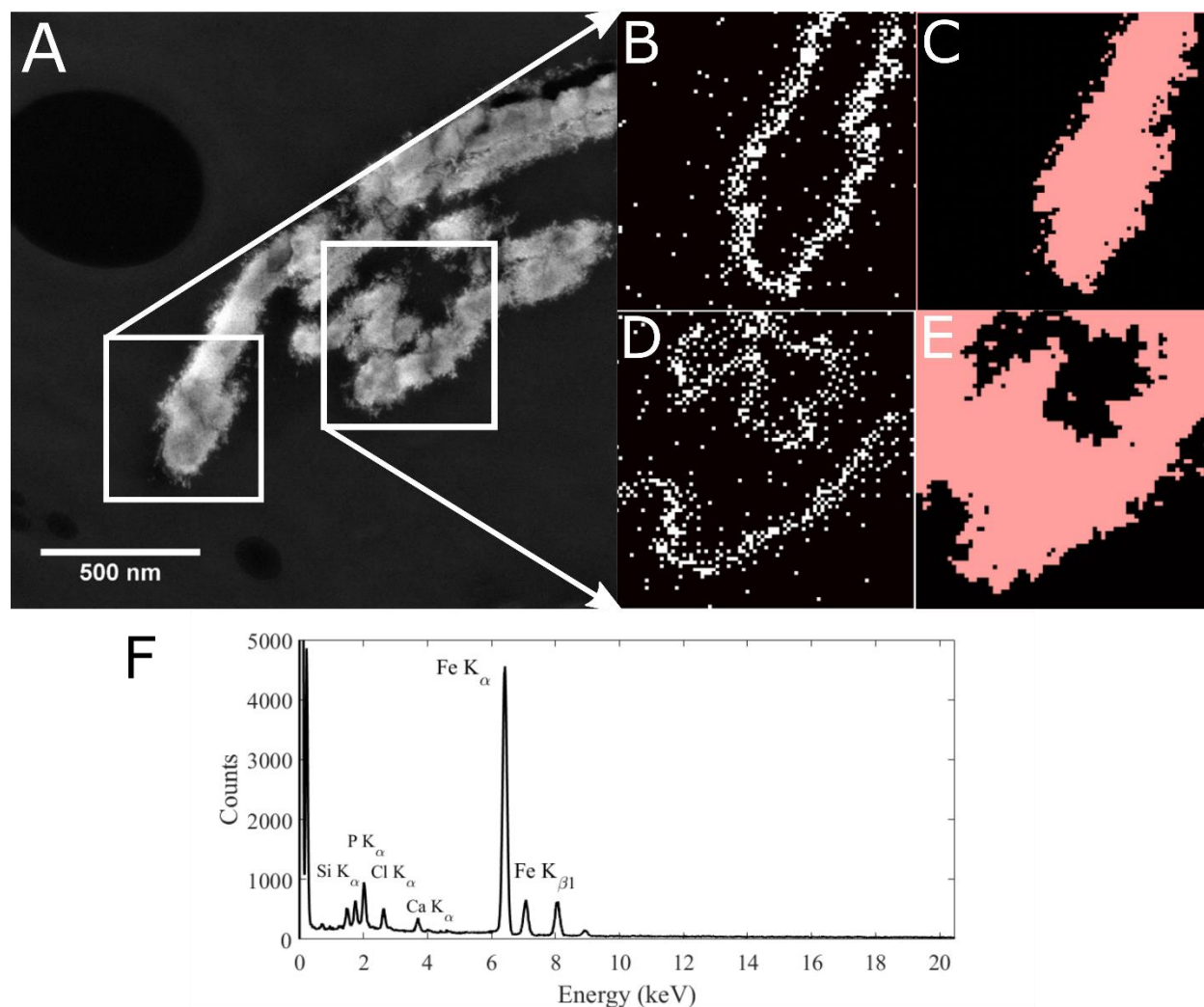
Figure 3.9 Autonomously collected dynamic EDS spectrum images of Gallionella bacterial residue, resin embedded and sectioned to 20nm. A. HAADF image collected on FEI Titan in

STEM mode at 300kV with a 150 µm C2 aperture, spot-size 6, and 10µs dwell time. B. Scanning mask sampled by the microscope tracking the Fe K_α peak as feedback from a Gatan controlled EDAX EDS (1024 channels at 10 eV width) detector of the leftmost inset in image A. 10% of the pixels in the 80x80 image were collected with a one second dwell time per pixel, resulting in a total collection time of 23.6 minutes vs. a conventional full SI acquisition of 2.7 hours. An initial 1% of the pixels was collected randomly.   C. Reconstructed discretized spectrum image of the elemental distribution of iron from the scan mask in B. D. Scanning mask collected from the rightmost inset in image A, again tracking the Fe Kα with an 80x80 grid and 10% sampling.   E. Reconstructed discretized spectrum image from the mask sampled in D. F. Representative spectrum collected with a 30 second dwell time showing the strong Fe K_α peak that was used for the mapping (2048 channels at 10 eV width).

As seen in Figure 3.9, even at a low sampling percentage (10%) both spectrum maps of the insets of the HAADF image closely mirror the expected iron distribution in these materials.   Strong agreement was reached with conventional fully sampled spectrum images, but at dramatically lower acquisition times and area doses. Notably, these EDS experiments were performed on a microscope with a single detector. Microscopes with additional and more efficient detectors can still enjoy an order of magnitude improvement of the total mapping time, while benefiting from a reduced individual measurement time.

As was the case for the boron nitride sample, *'weakly informative'* training images were supplied to the algorithm before performing experimental imaging. No information about the ellipsoid cross section or spindle-like planar distribution of the residue was employed to accelerate imaging. In the case of extraordinarily dose sensitive materials or very high-fidelity spectrum images, several low dose HAADF images may be used as the training database to further reduce the necessary sampling percentages.

One can also use the dynamic spectrum imaging framework to do high speed spectrum imaging of features other than pure elemental signatures in spectra. A titanium deficient region in a sample of titanium-aluminum, details of which can be found in previous publications [180], was identified using HAADF imaging and point-and-shoot EDS spectra. Utilizing the coefficients trained from the simple straight-line training database employed for the boron nitride flakes, the spectrum imaging was performed on a small inset of the HAADF image, shown in Figure 3.10.
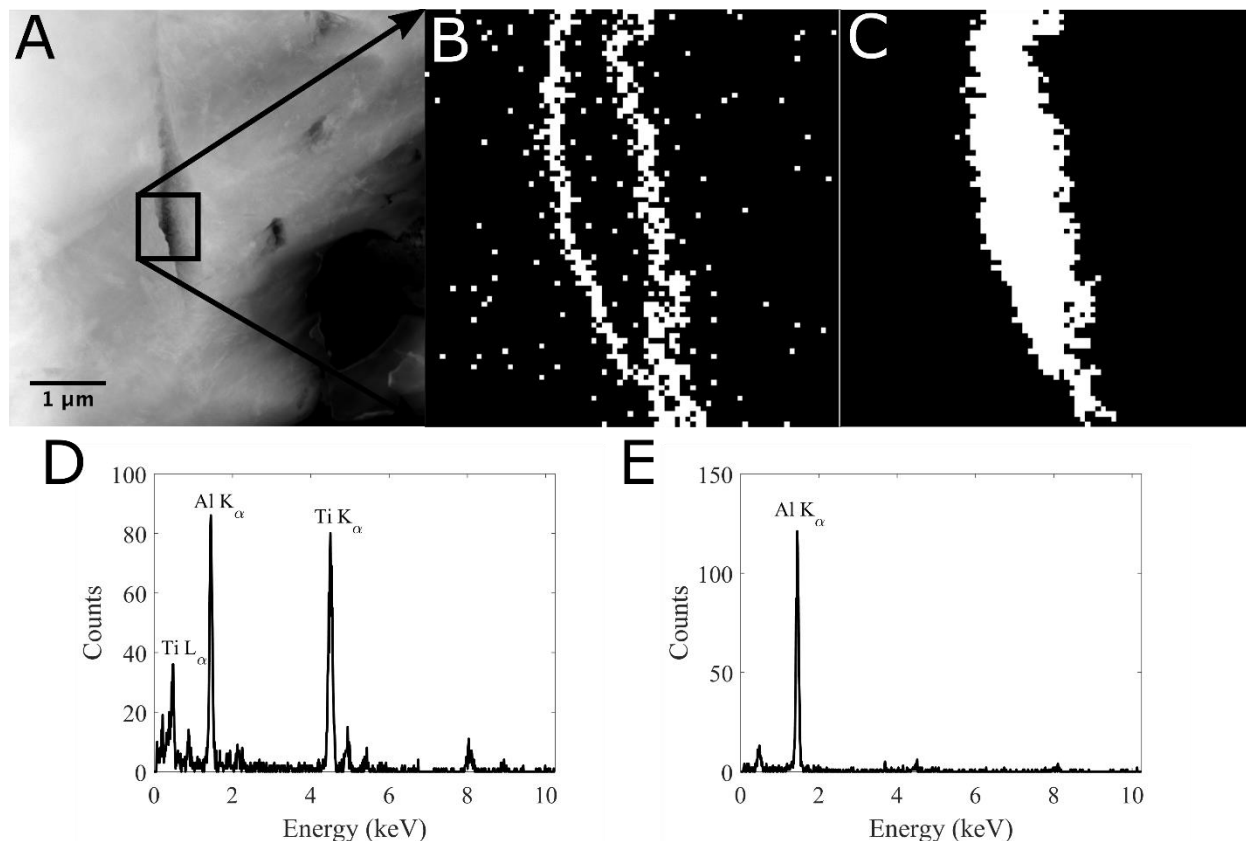
Figure 3.10 MOADS EDS mapping of a titanium deficient region in an annealed Ti 48 at. % Al alloy. Experimental details regarding material and sample preparation can be found in previous publications [180]. A. A HAADF image collected on an FEI Titan at 300 kV with 150 μm C2 aperture, spot-size 6 with 10μs dwell time equipped with Gatan controlled EDAX EDS detector. A one second dwell time per spectra with 1024 channels and a 10 eV width was used during autonomous collection. B. Final sampling mask after an initial 1% of the points were randomly sampled up to 7% maximum sampling of the 80x80 grid of pixels in the spectrum image. C. The discrete reconstructed image of the titanium deficient region, which tracks the dark feature in the

inset of the HAADF image. D. Representative EDS spectrum collected from the light matrix in the image in A, showing strong signal from both the Al K_α peak and the Ti K_α peaks (dwell time 30 seconds). E. A second spectrum collected in the dark region of the inset in A showing the disappearance of the titanium peak (1024 channels with 10 eV width).

The mapping signal was defined as a discrete version of the ratio between the Al K_α peak and the Ti K_α peaks, where a Boolean one represents a ratio of greater than two (titanium deficient region) and Boolean zero represents a ratio of less than two. In Figure 3.10A, the region of interest is defined over a HAADF image and a spectrum mask collected from the mask of sampled pixels in 3.10B. Using the ratio between the Al K_α and Ti K_α, the algorithm was quickly and autonomously able to map the spatial extent of this titanium deficient region using minimal prior information and mapping time. Other unique sample metrics may be chosen, such as the ratio of a plasmon peak to a core-loss edge in EELS, etc. in addition to producing independent maps. The ability to optimize a map for a specific signal (or combination of signals) is a novel ability of dynamic sampling. Although different signals may have different experimental resolutions, this should not affect the ability of the dynamic sampling algorithm. Lower resolution signals will be easier to approximate at smaller length scales with inpainting, so even with a small pixel size to accommodate another signal the algorithm will simply space measurements out to maximize the quality of the reconstruction. As established in the introduction, the resolution and contrast are intimately related, so basing sampling decisions on contrast inherently considers the varying

resolution due to the smearing of the signal due to the poor instrument/mechanistic (core loss vs. plasmon loss) resolution.

In this technique prior information about the type of images encountered is used to infer a set of coordinates which can map features in an undersampled image to the relative 'usefulness' of additional measurements. Thus, it is useful to compare the similarity between the training images and the experimental images to understand the strength of this prior information. As can be seen in Table 3.2 three metrics of similarity all show that the prior images give very little specific information regarding the nature of each experimental sample. Instead, generalizable information which is not specific to a particular location in the image or a specific configuration of contrast, such as the usefulness of an interface or gradient, are used.

	MoS_2-Fe_3O_4	Boron-Nitride	Gallionella	Iron Oxide Particles
PSNR	3.0633	3.7933	5.9028	8.2312
Cross-Correlation Coefficient	0.2375	0.3070	0.1855	0.0101
SSIM	8.2783e-04	0.3417	0.0358	0.0429

Table 3.2 Similarity metrics between training images (top row Figure 3.3) and experimental images. The Cross-Correlation Coefficient runs on a scale of zero to one, zero being no correlation

and one being complete correlation. None of the images are more than 30% similar. Additionally, the Structural Similarity Index Measure (SSIM) also runs on a scale from zero to one, zero being least similar and one being perfect similarity. For this reason, the training images used in this work (Figure 3.3) as referred to as weakly informative, as they have very little direct similarity with the experimental images.
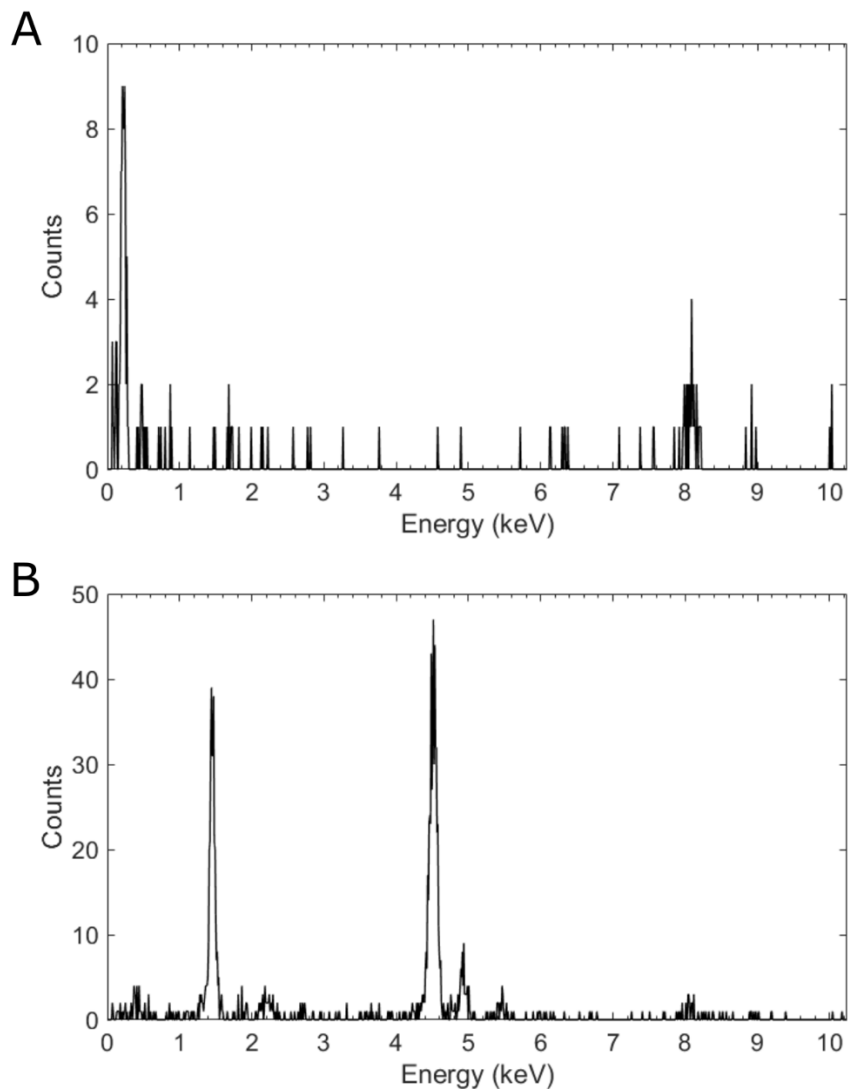
Figure 3.11 A comparison of the raw spectra collected during the MOADS experiments demonstrated in this work. A. Unprocessed spectrum from the Gallionella sample (Figure 3.9) and B. unprocessed spectrum from the Ti-Al sample (Figure 3.10). Both spectra were recorded with a one second exposure.

Figure 3.8	Fully Sampled Image	4% sampling
Pixel Density	80x80 pixels	80x80 pixels
Pixel size	9.2 nm	9.2 nm
Dwell time per pixel	0.5 sec (*2)	0.5 sec (*2)
Total time for map	4 hours	9.6 minutes

Table 3.3 Acquisition parameters for fully and dynamically sampled spectrum images in Figure 3.8.

Figure 3.9	Fully Sampled Image	10% sampling
Pixel Density	80x80 pixels	80x80 pixels
Pixel size	5.7 nm	5.7 nm
Dwell time per pixel	1 sec	1 sec
Total time for map	2.7 hours	23.6 min.

Table 3.4 Acquisition parameters for fully and dynamically sampled spectrum images in Figure 3.9.

Figure 3.10	Fully Sampled Image	7% sampling
Pixel Density	80x80 pixels	80x80 pixels
Pixel size	10 nm	10 nm
Dwell time per pixel	1 sec	1 sec
Total time for map	2.7 hours	16.5 min.

Table 3.5 Acquisition parameters for fully and dynamically sampled spectrum images in Figure 3.10.

Previously, it has been shown that for some samples random scanning can outperform other proposed scanning systems in image quality (such as spiral, Lissajous, and line skipping) [182]. However, since the mask is *a-priori* defined independently of the sample, it is difficult to achieve an order-of-magnitude reduction in dose and time. Even with state-of-the-art inpainting methods, it is unlikely that a static scanning mask will allow for sub 15% sampling rates with accurate reconstruction [135, 181], which is still much larger than dynamic sampling for comparably poorer image quality. For *under-sampled* imaging with a static mask, it has been suggested that denoising a fully sampled low exposure image with the same *prior* information may lead to higher quality images [151]. In the case of dynamic sampling, acquiring a comparable fully sampled low-dose spectrum image to Figure 3.8 would involve a total collection time of 9.6 minutes on 120x120 pixels, and consequently individual spectrum exposures of 40 ms (compared to 1s). Due to the extremely low sampling rates Dynamic Sampling achieves (5-10%), comparable fully-sampled spectrum images would often have individual measurement times below the detection limit for many EDS peaks or EELS edges. Therefore, dynamically sampled spectrum images could contain the same spatial information with the larger individual collection time necessary to resolve 'fine-structure' and crucially, without the need to directly process spectra with computational methods.

3.4.1   Limitations

In Figure 3.12, a situation which can challenge the performance of MOADS, and potentially lead to sub-optimal image reconstruction is illustrated.   At this field of view there are a considerable number of gallionella streaks and agglomerates scattered on the dark carbon support.   As such, during the initial 1% sampling, it is highly likely that the initial unguided scan mask will miss many of these isolated features.   The parameter c, which controls the width of the Gaussian heuristic used to calculate the ERD, controls the relative reward the algorithm receives for taking relatively safe bets vs allocating dose in unexplored regions of the image.   The parameter c controls the tradeoff between *exploration* and *exploitation.*
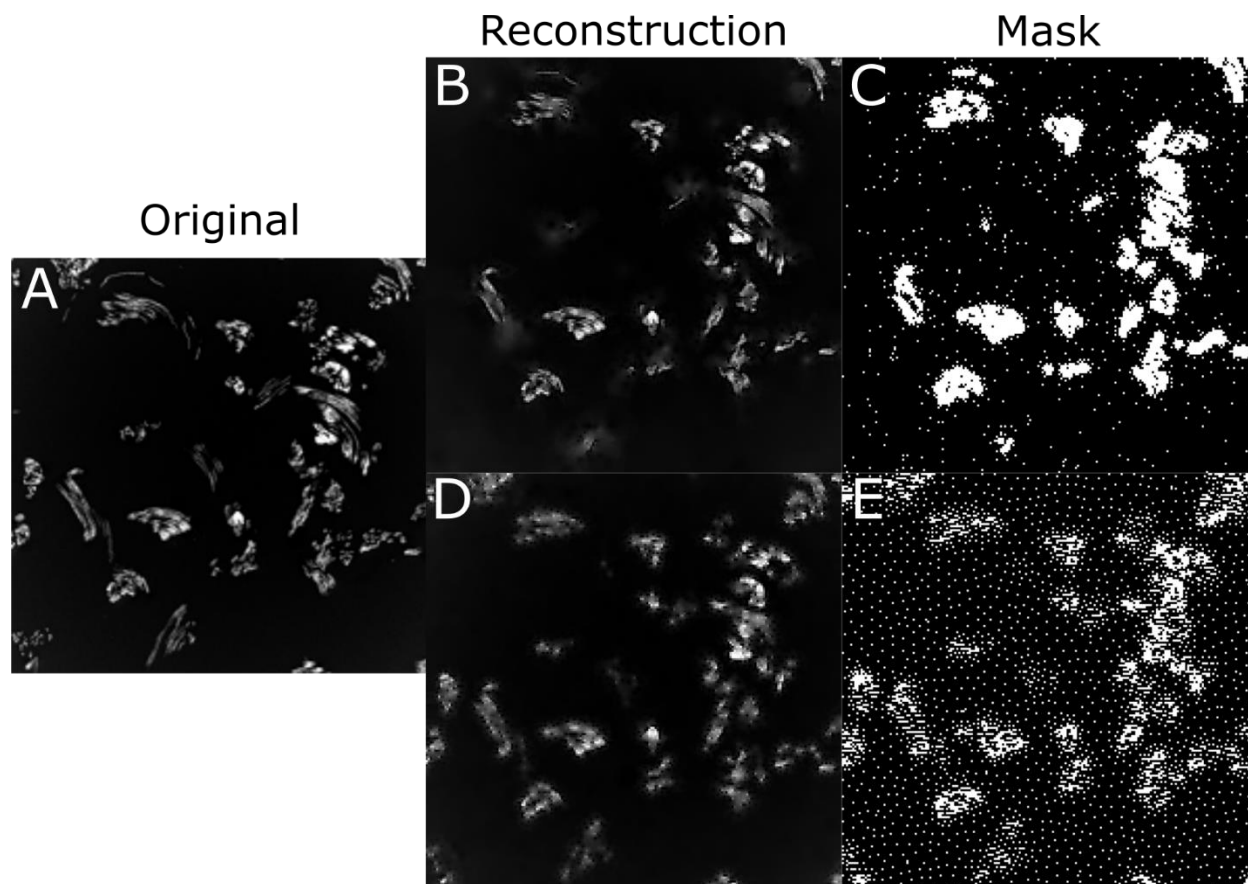
Figure 3.12 A. The ground-truth original image is a low magnification HAADF image of the Gallionella residue that has been down-sampled to only 200x200 pixels. At this pixel density and field of view, many isolated single or small groups of pixels have significant impact on the distortion in the image. B-C. Reconstruction and mask after sampling 10% of the pixels with c=32 (self-estimated from the training data – top row of 3.3). D-E. Reconstruction and mask, also after sampling 10%, with the c parameter set to 2.0.

In previous work, a method to self-estimate this c parameter has been developed using the training data. However, in this figure a worst-case series of training images have been used (the top row of Figure 3.3 - simple lines separating bright and dark contrast) and thus gives little information about the need to explore for smaller scale features. Thus, the self-estimation results in a very large c parameter (32).

For the c parameter set to a large value (32), Figure 3.12 B-C shows how the algorithm prefers sampling additional points on particle agglomerations it has already discovered. This results in only a small fraction of the total number of particle agglomerations being detected, but each is resolved at high detail. This is heavy *exploitation* of known information while avoiding *exploration*. For the opposite case with a small c value (2) in Figure 3.3 D-E, more points have been dedicated to the spaces between the Gallionella residue (heavy *exploration* and limited *exploitation*). As a result, fewer features are missing from the reconstruction, but the reconstruction quality of each individual structure is subjectively worse.

As shown in Figure 3.12 and 3.13, MOADS can often yield sub-optimal reconstructions when the magnification and pixel densities are set at such a level as each pixel becomes meaningfully important. Such images violate the assumption that most pixels do not carry significant information. Despite this, MOADS can often produce images with useful information, and does

not outright fail. The best way to understand this behavior is in the classical experimental design terminology of *exploration vs. exploitation*, in which a tradeoff must be made between sampling important pixels in a nearby area versus searching for new isolated structures in the image. The user has control over the behavior of the algorithm in this situation, by manually setting the c-parameter to either: **1.** Maximize the percentage of isolated structures identified, or **2.** Maximize the quality of a few isolated structures. The user also has the option of simply increasing the pixel sampling rates for a conservative setting of c. At worst case, the algorithm will simply continue sampling pixels until the image is fully sampled, and thus performing no worse than a conventional spectrum image collection.

Reconstruction

Mask
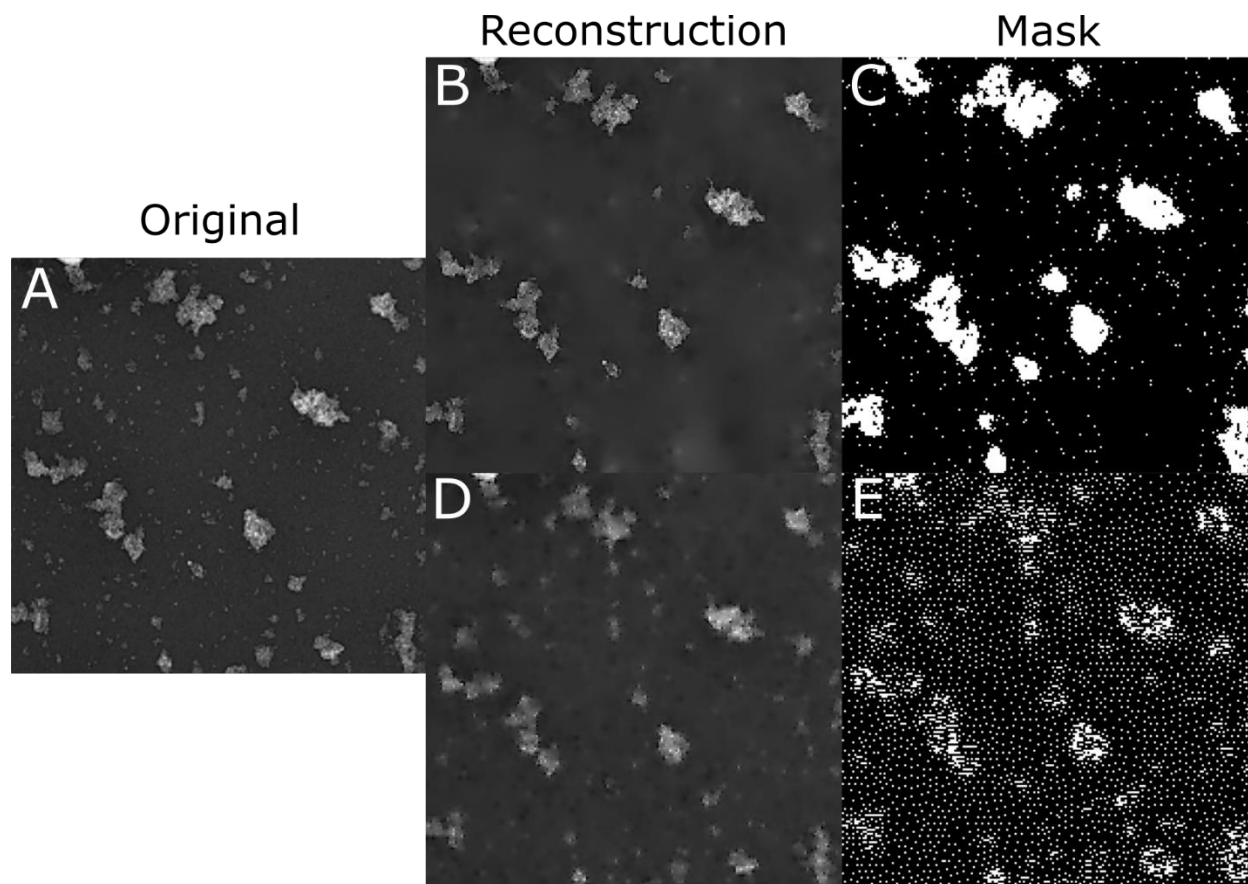
Original

Figure 3.13 Trade-off case #2. **A.** The ground-truth original image is a low magnification HAADF image of the iron oxide nanoparticles distributed on a carbon grid, which has also been down-sampled to only 200x200 pixels. Many agglomerations of particles are present, but also a significant number of isolated single or several pixel clusters. There are simply not enough pixels in the sampling budget at <10% sampling and such a coarse grid to search for all the small clusters, while resolving the large agglomerations with a sufficient level of detail. The tradeoff between exploration and exploitation cannot be avoided, and if the user cannot increase the pixel sampling

rate or decrease the field of view, the user should manually set the *c* parameter depending on his priority. Poor training images have also been used – the top row of Figure 3.3. **B-C.** Reconstruction and mask after sampling 10% of the pixels with c=32. As can be seen in the scanning mask, the algorithm has prioritized heavy sampling of a small number of large features and small clusters (heavy *exploitation* of known information) and has avoided taking new measurements elsewhere (limited *exploration* of unknowns). **D-E.** Reconstruction and mask, also after sampling 10%, with the c parameter set to 2.0. As can be seen in the mask, more points have been dedicated to searching for new clusters (heavy *exploration* and limited *exploitation*). As a result, fewer features are missing from the reconstruction, but the reconstruction quality of each individual structure is lower.

Although the calculation time to perform one loop of the dynamic sampling prediction is much less than the time to acquire a typical EELS or EDS signal, it is still much too large compared to dwell times for typical electron imaging (HAADF, Transmission, SE). In these modes, static scanning masks or low-exposure denoising will likely be the preferred mode of operation due the time cost (milliseconds for calculation and microseconds for collection). However, the advantages for analytical imaging are clear, and MOADS or other similar dynamic sampling approaches may open wide-field elemental imaging of materials not previously feasible.

We have highlighted MOADS as an area dose reducing technique, but it is important to emphasize that the fluence per pixel remains the same as fully sampled imaging. Thus, if damage occurs long before a single pixel signal is integrated, MOADS will offer no additional advantage over conventional fully sampled imaging. Especially in STEM, where we have a bevy of different signals and imaging modalities, we often would like to obtain multiple signals from the same region-of-interest (ROI). By reducing the area of the sample that experiences an interaction with the electron beam, it becomes possible to make additional measurements (such as high-res imaging or nano-diffraction) within the same ROI on pristine specimen. This would allow a user to get more from their sample by reducing the impact of multiple observations. In other cases, one could also imagine reducing the per-pixel fluence by using MOADS as an initial segmentation tool. After delineating the regions between domains of differing composition using a few dynamically selected points with long dwell time, the pixels contained within one domain could be recorded using a drastically lower acquisition time and integrated into one representative spectra. Future work will explore creative applications of MOADS to both reduce area dose and single pixel fluence.

3.5   Conclusions

We have developed an algorithmic platform for accelerated and low-dose experimental analytical imaging of materials that is applicable to arbitrary Scanning Transmission Electron Microscopes

using Digital Micrograph or other scriptable OEM software. In contrast to static sampling schemes or denoising, this method can produce spatially accurate spectrum maps at high speeds/low doses with *weakly informative prior* information, and no direct processing or manipulation of spectral data (no sparsity constraints). By maximizing the application of electron dose to areas with meaningful information or contrast on-the-fly, MOADS may allow for the efficient characterization of radically larger regions of interest or materials/interfaces that are sensitive to accumulated dose. It is expected that dynamic sampling approaches will impact many radiative, serially collected characterization methods currently in use, and may reduce the time of acquisition by over an order of magnitude for some samples.

CHAPTER 4: STAGE ROCKED ELECTRON CHANNELING FOR ORIENTATION MAPPING

ABSTRACT

Microstructural analysis by crystal orientation mapping of bulk functional materials is an essential and routine operation in the engineering of material properties. Far and away the most successfully employed technique, Electron Backscattered Diffraction (EBSD), provides high spatial resolution information at the cost of limited angular resolution and a distorted imaging condition. In this work, a stage-rocked electron channeling approach is developed as a low-cost orientation mapping alternative to EBSD. This is accomplished by automated electron channeling contrast imaging (ECCI) as the microscope stage physically tilts/rotates a sample through a reduced hemisphere of orientations followed by computational reconstruction of electron channeling patterns (ECP). Referred to as Orientation Mapping by Electron Channeling (OMEC), this method offers advantages in terms of local defect analysis, as it combines the advantages of selected area ECP (SACP) and ECCI. Dynamic or "adaptive" sampling schemes are illustrated to increase the throughput of the technique. Finally, the implications for sample analysis in which large 3D maps of ECCI images can be routinely constructed of challenging crystalline samples are discussed. As an electron channeling-based approach to orientation mapping, OMEC may open new routes to characterize crystalline materials with high angular and spatial resolution.

4.1 Crystal Orientation and Texture

A plethora of materials properties and phenomena revolve around the Neumann principle, which relates the innate crystal symmetry to the physical properties. Optimizing these properties relies on a physical exploration of the macro-scale properties simultaneously with the underlying crystal structure. Polycrystals are one of the most common forms of engineering materials, which have large numbers of interlocked areas of varying crystalline orientation. The innate underlying symmetry of the crystals results in anisotropic properties for each local domain, or grain. Thus, the macroscale performance of a particular system depends on the relative abundances of particular oriented grains. The wide-area fractions of different grains are referred to as the microstructural *texture*, which is often a function of the thermal and mechanical treatment of the material.

Texture is typically described using orientation distribution functions (ODFs) which quantify the relative fractions of orientations over the crystal. Thus for a particular orientation, g, with a volume fraction of grains in the material, $V(g)$, and a total volume, V_0, the ODF can be calculated as follows:

$$f(g) = \frac{1}{V_0}\frac{dV(g)}{dg}$$

(4.1)

Given an inherent material property which may depend on the orientation of the lattice, the ODF can be used to calculate an averaged macroscale property for a specific material by integrating over all present orientations and their volume fractions:

$$\langle \chi \rangle = \int_g \chi(g) f(g) dg \tag{4.2}$$

Mapping crystal orientation and texture across large areas (up to mm^2) of bulk samples with high spatial resolution (10's of nm) allows for this fundamental linkage between the underlying crystalline texture (and thus work history) and macroscale performance. Considerable work has been focused on developing techniques which can provide this understanding by directly visualizing orientation maps of bulk specimens to further engineer critical materials.

4.2 Mapping Orientation with Electrons

To determine the orientation of a crystal lattice with electrons, there are three key scattering mechanisms between an underlying lattice and an incident beam of electrons. Firstly, electrons may be elastically scattered (conservation of energy) coherently (conservation of phase) by Bragg scattering which results in small scattering angles. Bragg scattering leads to a periodic distribution of electrons inside the crystal and Bragg diffraction. Further, electrons may be phonon scattered or experience thermal diffuse scattering (TDS), in which the electrons lose a small amount of

energy incoherently (phase information is lost). Core-loss scattering, which has been discussed in the context of EELS and EDS, can also occur resulting in larger energy losses and the emittance of X-rays or secondary electrons. Repeated inelastic or phonon scattering can result in multiple scattering and a broad range of electron energies and large scattering angles. Electrons which experience a large change in angle due to Rutherford scattering and some which experienced multiple pseudo-elastic scattering can re-emerge from the sample as relatively high energy electrons (> 50 eV). This process is commonly used to model Backscattered electrons.
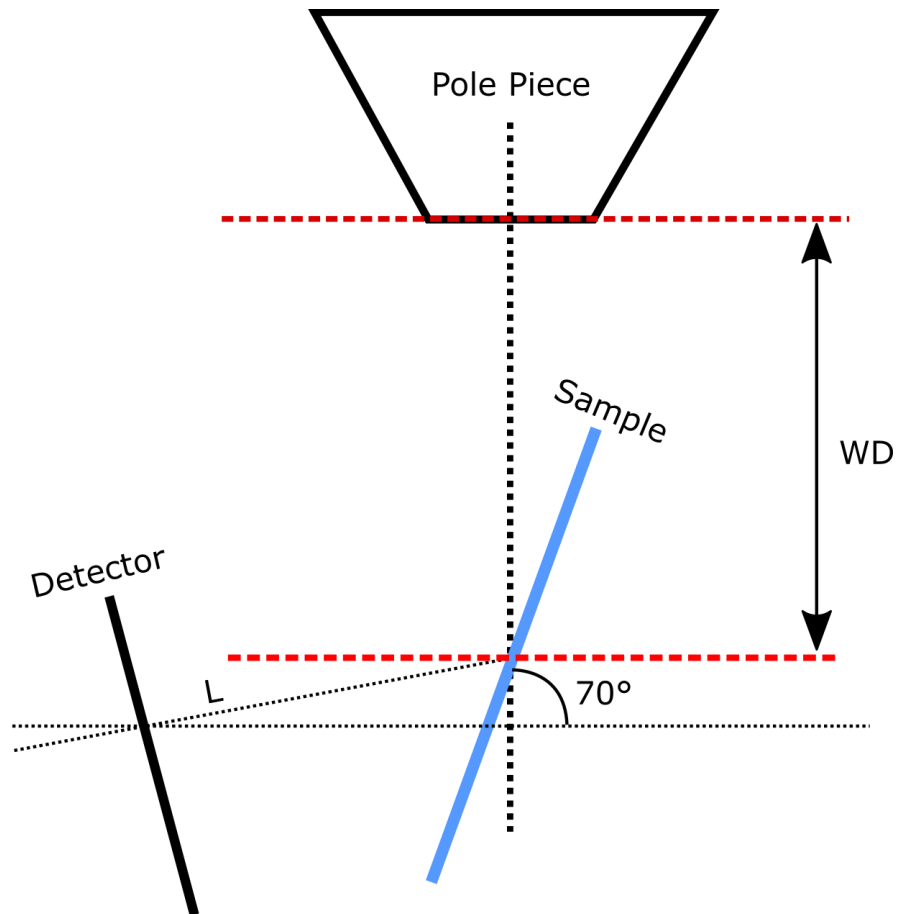
Figure 4.1 Schematic diagram of a typical EBSD set-up including an external camera. The sample is tilted to a high angle to promote the collection of diffracted backscattered electrons onto the inserted camera. The working distance, WD, is defined as the distance between the pole-piece of the microscope and the field-of-view on the specimen. A defined camera length, L, then describes the physical distance between the specimen and the detector. Note the oblique angle between the detector and the sample.

Electron backscatter diffraction (EBSD) has become the preeminent technique for performing routine orientation mapping in conventional scanning electron microscopes (SEMs)[183]. As seen in Figure 4.1, in EBSD an electron probe interacts with a highly tilted specimen. Psuedo-elastic and multiple scattering events result in a range of forescattered angles with may be further Bragg diffracted which results in the emergence of a coherent wavefield from the specimen. The beam is scanned across the sample surface and at each grid point over a region of interest, the 'cones' of Bragg diffracted electrons are intercepted by a 2D electron detector to form an electron backscatter pattern (EBSP). Leveraging advanced detectors and computation, modern EBSD systems allow the automated acquisition and indexing of EBSP's at speeds of more than 1500 patterns per second[184]. Nevertheless, EBSD requires a significant investment in additional hardware and suffers from limitations including image/scan distortion[185] due to the highly tilted (typically 70 degrees) sample. Spatial resolution in standard EBSD is non-uniform (i.e different in lateral and longitudinal directions)[186] and on the order of 20 nm while the precision of angular measurements is on the order of 1 degree[187-189].

Before interacting with the specimen, the incident beam of electrons is typically modeled as a plane wave. As the beam enters the sample and interacts with the underlying lattice, the resulting field can be modeled as a superposition of standing waves, referred to as Bloch waves. These waves are simply the solution of the time-independent Schrodinger equation for a high energy electron experiencing a periodic atomic potential.

$$\nabla^2 \Psi + \frac{2m}{\hbar^2}[E - \sum_h V_h \exp(2\pi i h \cdot r)]\Psi = 0 \tag{4.3}$$

Given the electron mass, m, accelerated with a particular kinetic energy E, experiencing a complex Fourier series potential, V, for a particular set of lattice vectors, h. The solution of this equation is given by the following linear combination of Bloch waves:

$$\Psi(r) = \sum_j \varepsilon^{(j)}\psi^{(j)}(r) = \sum_j \varepsilon^{(j)} \sum_g C_g^{(j)} \exp[2\pi i(k_0^{(j)} + g)\cdot r]\exp(-2\pi q^{(j)}z) \tag{4.4}$$

For a particular lattice at a specific orientation, a given number of Bloch waves are present at a time, j. This corresponds to a separate set of diffracted beams from the primary beam. Backscattering then occurs when electrons are incoherently removed from the primary Bloch wave field by atomic potentials. Certain Bloch waves have their maxima on atomic columns, while others are centered between the columns[190]. Thus, those that interact strongly with the atomic columns are more strongly damped and participate more often in backscattering. Since the relative amounts of backscattering depend on the fraction of electrons available to participate in scattering at a given depth, the population of different Bloch waves affects the incoherent intensity from the crystal, which can be detected. This results in an orientation dependent intensity that derives from the fundamental channeling of the primary beam onto other diffracted beams. In principle, such intensity changes are also measurable from other signals, such as secondary electrons (SE II& III).
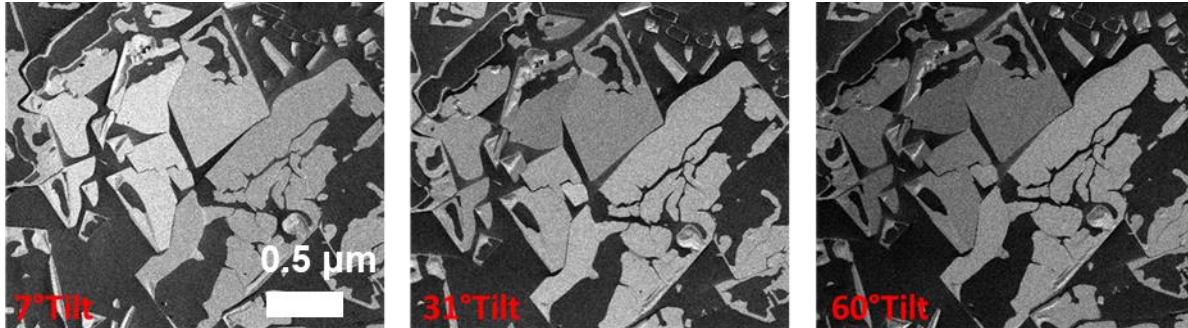
Figure 4.2 Tilt dependence of the BSE signal from an aluminum polycrystal specimen. As the angle between the incident beam and the lattice in each grain shifts, the beam comes off and on diffraction conditions. This results in a changing BSE yield and corresponding contrast change over stage motion that depends on the individual orientation of each grain.

Recording the BSE intensity as a function of beam-specimen angle results in the formation of Electron Channeling Patterns (ECP), which can give analogous information as EBSD about the underlying orientation of the specimen due to this orientation depend contrast. In practice, ECPs have been acquired by low magnification imaging of large single-crystal regions (beam rocking due to divergence in raster scan)[191], by stage rocking with a fixed beam[190], or by rocking the beam about a fixed point to generate a selected area electron channeling pattern (SACP)[192].

Compared to EBSD, ECPs provide the same orientation information without the geometric distortion that comes from intercepting a three-dimensional signal from a tilted specimen onto a

non-perpendicular plane[185]. Since the angles between bands are used to precisely calculate orientations, indexing can be limited by the accuracy of the forward geometric model used to account for this complex distortion. ECPs also provide high angular resolution information, provided a small beam convergence angle (< 3 mrad)[190]. They have also been shown to provide strain information *via* higher-order Laue zone (HOLZ) lines[193, 194]. Strain analysis by EBSD is ultimately limited by the pixel resolution of the detector, although high-resolution EBSD can provide improved angular resolution by including additional image post-processing steps[187, 195].

SACP is the most common method for ECP collection, but it requires specialized electron optics for beam rocking, which limits broad adoption of this technique. In addition, it suffers from poor spatial resolution (~500 nm) and limited angular field of view (FOV) (typically 10 degrees)[196] due to spherical aberration at large beam tilts[197]. Historically, individual ECPs were indexed by comparing them to physical ECP-maps. These maps were laboriously constructed by synthesizing hemi-spherical single-crystal samples[190], or fabricating dozens of uniquely oriented single crystal specimens and collecting many SACPs[198]. While useful for a limited number of simple crystal systems, these tasks were not practical for many material systems with lower symmetry or multiple phases. Methods to overcome the limited FOV and spatial resolution of SACPs, such as dictionary based indexing[199] and the use of spherical aberration correction[200], result in long computation times or large cost.

The related technique of electron channeling contrast imaging (ECCI) has been intensely explored for the imaging of local defects in the SEM. By mapping the local orientation and texture using EBSD (or less commonly SACP) the specimen can be tilted into a "two-beam" condition[201]. By capturing BSE images at several conditions, the Burger's vectors and other defect parameters can be calculated without the destructive sample preparation that would be required to generate equivalent information in Transmission Electron Microscopy[202]. Several reports have analyzed dislocation and twin structures in metallic films and surfaces using this method [203-205].

In early reports of electron channeling patterns, it was noted that a stage-rocked system with a fixed beam orientation could produce identical information to a beam-rocked ECP[206]. Early attempts at producing an accurate tilt/rotation stage were limited by the lack of computational control and could only maintain a consistent beam position within a micrometer at best[207]. More recently, techniques have been developed using ion channeling contrast in images taken at different beam-sample angles for orientation mapping by matching changes in contrast to theory/simulation[208-211]. While ion channeling contrast is extremely useful, the critical angles for ion channeling are quite large compared to electron channeling, potentially producing less accurate orientation indexing[212]. The recent electron channeling approach describe by Lafond, *et al* generates orientation maps based on ECCIs from multiple sample orientations[213]. However, their approach does not generate full ECPs and is likely limited to orientation mapping of high symmetry systems.
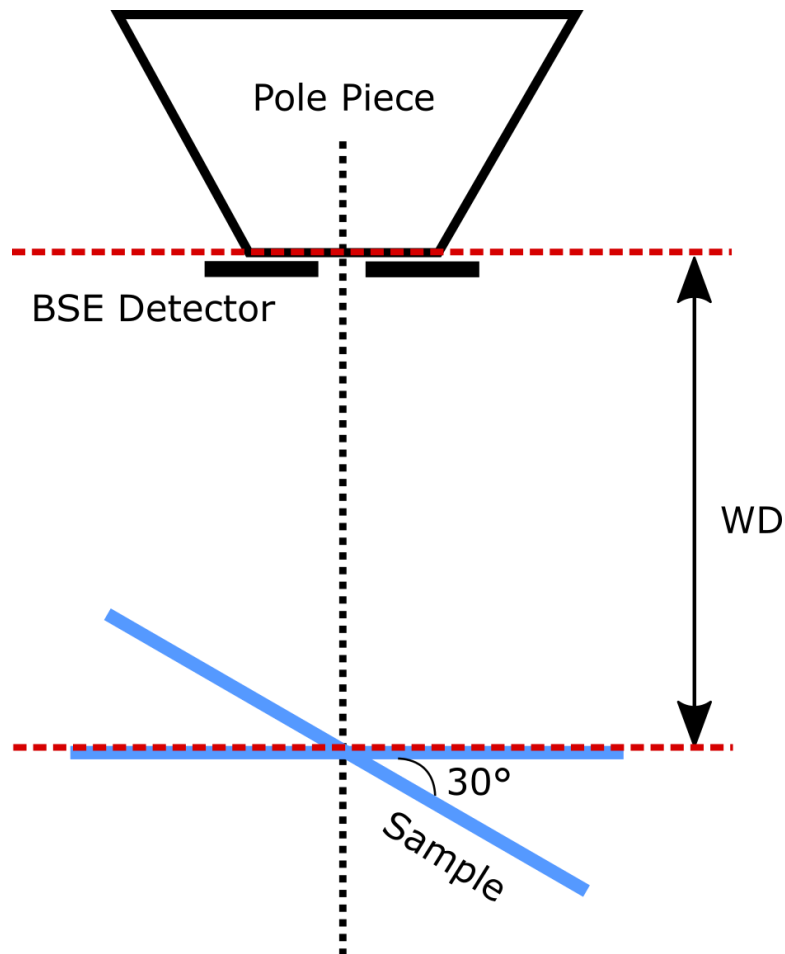
Figure 4.3 Schematic a stage-rocked ECP generation system, in which the sample physical tilts through a prescribed series of angles while the BSE signal is recorded on a conventional detector.

In the following, a system combining the advantages of ECCI and SACP which enables large area mapping of crystal orientation by recording full BSE ECCIs at many different stage orientations is demonstrated. This is accomplished by automated stage control and image acquisition followed

by computational image alignment. This alignment corrects for any image shift, rotation or distortion and generates an image stack from which spatially resolved channeling patterns are produced. The resulting ECPs have a high angular FOV, rendering them suitable for indexing by standard routines as conventionally applied in EBSD. The resulting technique, orientation mapping by electron channeling (OMEC), results in a very cost-effective orientation mapping solution with the high angular resolution and contrast of traditional ECP without any beam-tilt induced spherical aberration.

A

Automated Image Acquisition

Alignment and Segmentation

Construct Channeling Patterns

OMEC

Generate Orientation Map

Index Patterns

[1̄10]

[111]

[100]

B

ψ_y ψ_x

θ

x

y

ϕ
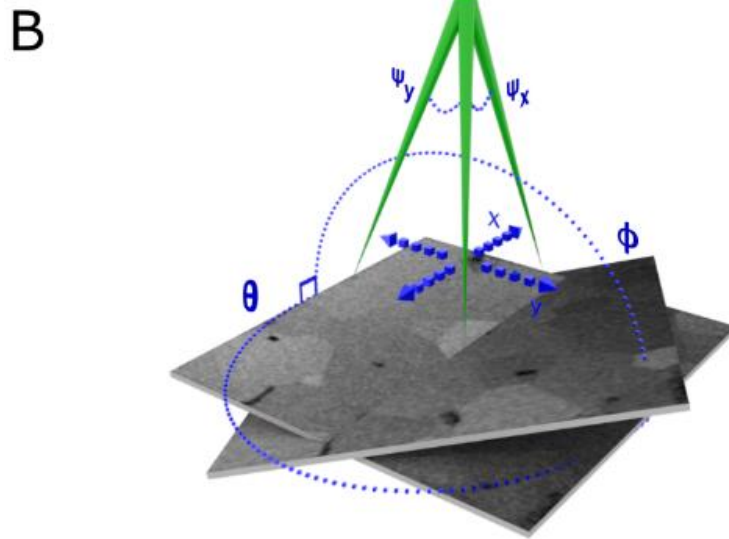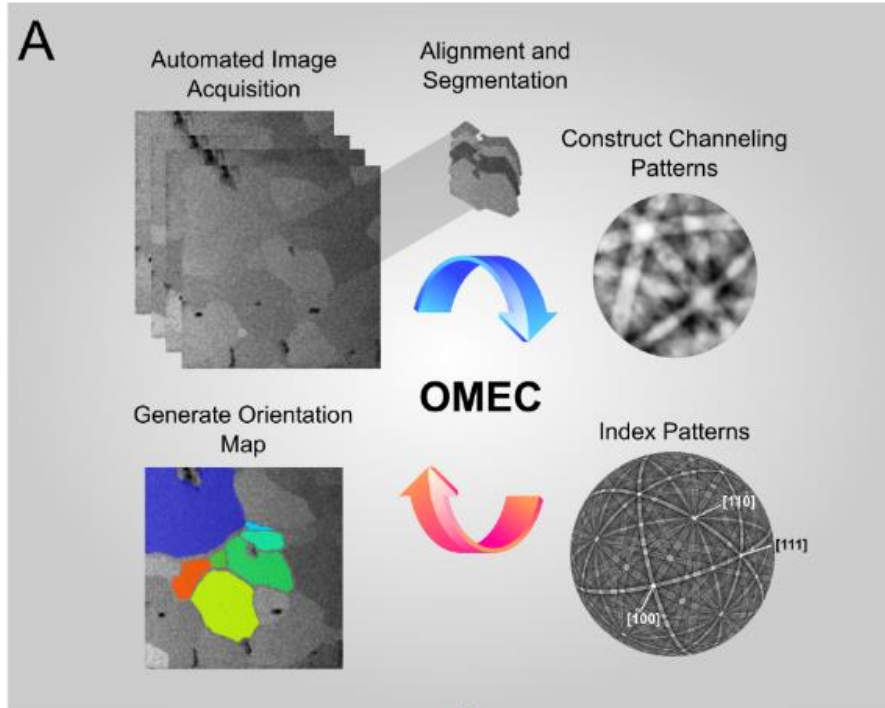
Figure 4.4 (A) Workflow of the proposed Orientation Mapping by Electron Channeling (OMEC) method. First, an automated image acquisition scheme acquires a tilt/rotation series of BSE images from the same relative sample area. This entire image stack is then aligned relative to each other, allowing a complete ECP to be extracted at each pixel. These channeling patterns can then be segmented or clustered (supervised vs unsupervised) into common orientations and then indexed through conventional methods. Finally, a full orientation map can be generated for the region of interest. (B) The variables describing various operations in the OMEC method are established, including the fixed tilt angle (φ) about a fixed axis and the in-plane rotation angle (θ). As the electron beam rasters across a fixed grid of pixels on a fixed plane defined by x,y it experiences a tilt along these axes parameterized by ψ_x and ψ_y.

In the first section of this chapter a single-crystal silicon (100) sample is examined and the hybrid stage/beam-rocking ECP that results due to the combination of stage rocking and beam rocking (due to raster scanning) is described. As no image alignment is necessary for a single-crystal sample, the angular range and accuracy of the stage-rocked channeling system is demonstrated. By taking advantage of the spatial information in each ECCI for a polycrystalline sample, precise image alignment can be used to correct spatial distortions that occur during stage tilt/rotation to produce a high quality ECP for each grain of a PbSe/GeSe thermoelectric material. The acquisition speed of the technique can also be improved by sampling a reduced set of critical tilts/rotations on-the-fly with dynamic sampling, using redundant information to "synthesize" less critical ECPs.

4.3 Developing a Stage-Rocked Orientation Mapping Technique

4.3.1 Sample preparation and data collection

To sample enough orientations to generate a reasonably high resolution ECP, automated imaging was employed. To accomplish this, a script was developed to capture images at a range of rotation and tilt steps on a commercial FIB/SEM (FEI Helios Nanolab) using the manufacturer's scripting interface. The standard instrument stage has eucentric tilting and rotation capabilities, which were accurate enough for this application. A typical experiment included 0.5 degree tilt steps from 0 to 34.5 degrees (69 degrees angular range) and 2 degrees rotation steps from 0 to 358 degrees, resulting in a 12,600 image data set (512×442 px) over approximately 10 hours. Imaging was accomplished with a 2-5 kV accelerating voltage, high beam current (1.4-22nA) and the TLD in BSE mode. Silicon samples were imaged without any surface preparation, but the mechanically polished PbSe/GeSe sample was cleaned *in situ* with a plasma cleaner to remove organics (iBss GV10x) followed by a 5 kV Ga ion beam to remove surface oxidation.

4.3.2 Single crystal silicon data processing
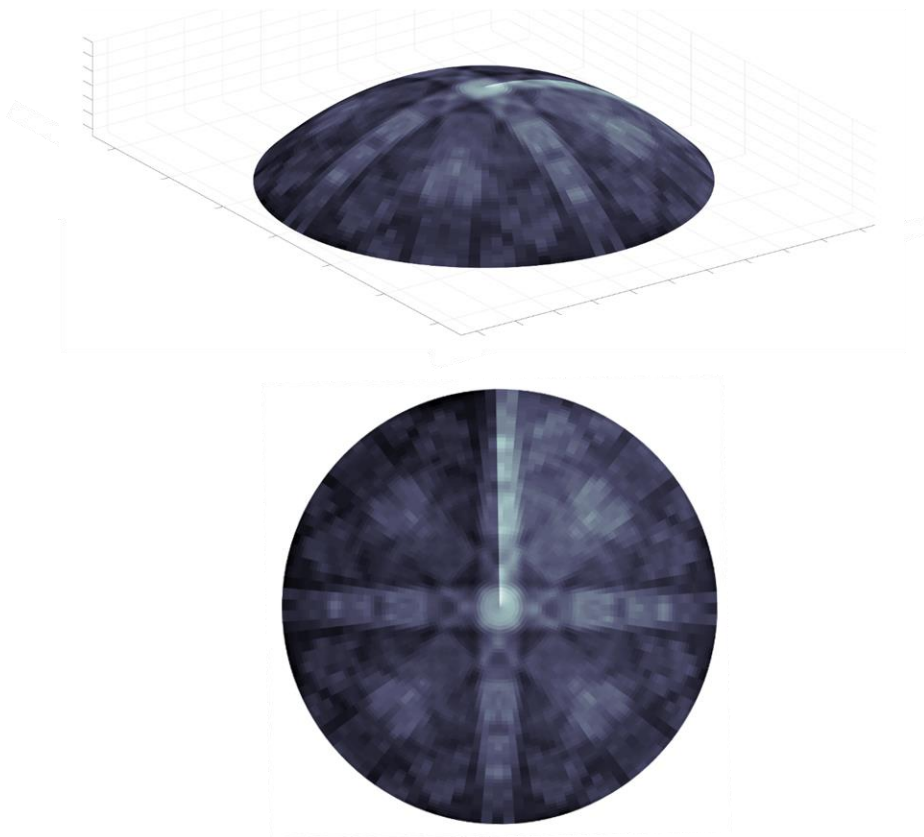
Figure 4.5 Channeling contrast recorded as the stage moves around is a true spherical representation of orientation space and can be mapped to a sphere digitally. This sphere can then be projected in any of the well-known geometric projection operations. Here, a raw channeling contrast dataset from a silicon single crystal is plotted in both three and two dimensions using an equiangular projection.

ECP's are generated from the SEM images by plotting the average contrast of the entire image or a subset of the image (grain, etc.) as a spherical projection according to the beam-to-sample orientation. These data are displayed as an orthographic or stereographic projection but are manipulated in spherical coordinates. There is systematic contrast variation in these images according to the sample tilt condition which is corrected by a background subtraction at each tilt step based on the average contrast for all rotation steps. As the beam is deflected during raster scanning, the beam diverges from the nominal beam-to-sample orientation. This results in a different orientation condition for every pixel in the SEM image, which depends on the working distance, pixel position and sample tilt. For the silicon samples, the background-corrected 512×442 pixel images were cropped and binned to generate 16×16 pixel subsets and a divergence correction was applied to plot the average contrast value of each subset. This was accomplished by assigning a vector to each nominal orientation position and performing a Rodrigues rotation about that vector for the divergence associated with each subset. As the divergence angles during raster scanning are proprietary and not known to the authors, these angles were estimated empirically to improve ECP quality. The resulting data set was adjusted for contrast variation due to beam contamination by subtracting the intensity of a 3rd degree polynomial fitted to the data in order of collection. During the final display operation, overlapping data points at low tilts were handled by grid-cell averaging and gaps between data points at high tilts were interpolated.
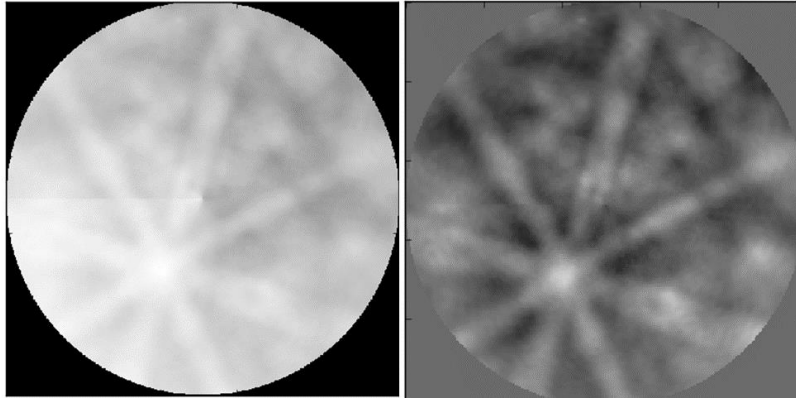
Figure 4.6 Left: Raw extracted channeling pattern from a single pixel of a PbSe-GeSe crystal showing strong angular dependent contrast. As you move clockwise around the pattern the intensity increases due to the accumulation of carbon contaminants and charging on the specimen surface. Since these images are taken with a TLD BSE detector, high currents and long dwell times are necessary for adequate signal-to-noise ratio. Systems with dedicated BSE detectors will likely not encounter this issue. Right: Contrast normalized and background signal subtracted by fitting a third order polynomial to remove time-dependent effects due to charging and mass accumulation.

4.3.3   Polycrystalline sample data processing

For polycrystalline samples, an image sequence of tilted/rotated BSE images was collected and then transferred offline to a processing computer for image alignment/correction. The image stack is composed of multiple tilted view of an approximately flat plane from a point illumination source.

The flat plane approximation is well satisfied for most specimens due to the need for extensive polishing to prevent the domination of surface related contrast. The goal will be to bring all different viewpoints on to a common coordinate frame to account for any errors in stage movement and to correct the projected distortion from acquiring a three-dimensional motion onto a two-dimensional grid. Thus, any individual pixel in one frame can easily be selected in all remaining as the object physical translates within the chamber.

Misalignments in the three-dimensional motion of the stage can cause unwanted rotations and translations if they occur in the two-dimensional plane perpendicular to the electron optics, or scaling/magnifications if they occur parallel to electron optics. In addition, since the plane over which the beam scans remains fixed relative to the stage, three-dimensional rotation of the sample around its eucentric point will cause distortion. To reconstruct a pixel-by-pixel or grain-by-grain orientation map, an alignment method must sufficiently correct for the artifacts while being contrast independent (since grain contrast inherently changes between angular frames).

Given a few accurate points of correspondence between two images of planar objects captured at different perspectives, define a homography matrix, H, can be defined to warp the remaining pixels onto a common coordinate frame. Algorithms to detect keypoint features of correspondence between images at different perspectives and illuminations, such as the Scale Invariant Feature Transform (SIFT)[214], can be used to define this set of corresponding points. Briefly, SIFT operates by creating a multi-scale edge and corner detector using Difference of Gaussians (DoG). The

image is blurred by Gaussian kernels of increasing width and their collated difference taken. Extrema in this image pyramid correspond to the maximum spatial extent of a certain edge or corner feature, which may be used as a particular keypoint. Keypoints are filtered by a series of contrast and edge sensitive filters in order to improve their quality. A vector describing the local space around a keypoint is created by taking a radial histogram over one full rotation, and additional vectors constructed for local windows around the keypoint. Here, normalization can be used in order to increase robustness to changes in illumination. Keypoints are matched using a brute-force nearest neighbor search and false positives rejected using the Lowe ratio test. Finally, an estimate for the homography matrix to align the images is constructed using robust regression from the matched keypoints (RANSAC: Random sample consensus).

For image sequences collected of polycrystalline specimens in OMEC, SIFT keypoint detection followed by a homography based image warp is sufficient to bring all orientations onto a common spatially correspondent coordinate frame with minimal parameter tuning. Once a common set of coordinates is established, an orientation map for each pixel can be produced exactly as described above in the case of the single crystal silicon specimen for arbitrary or defined subsets of pixels with shared orientations.
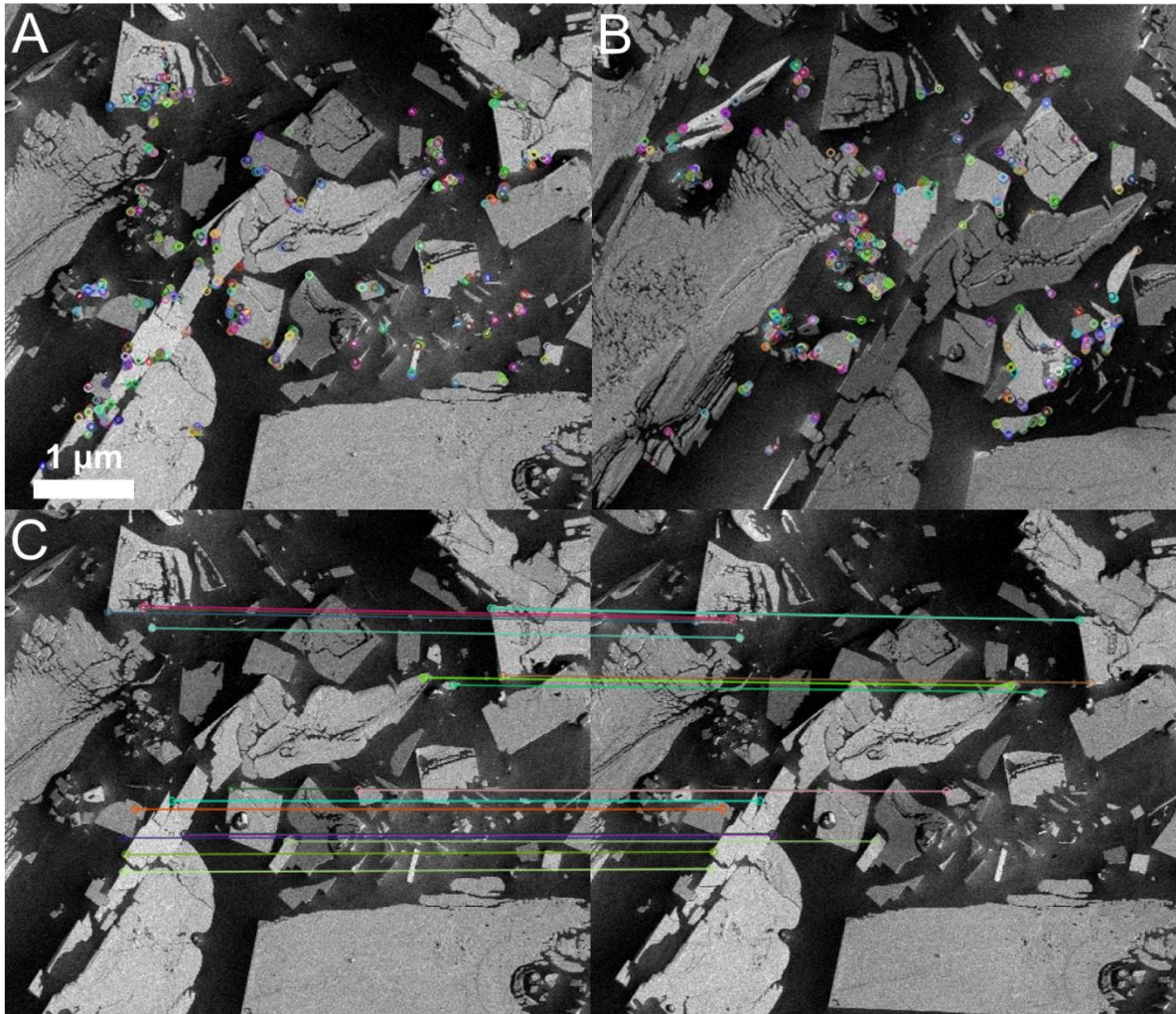
Figure 4.7 A series of BSE images collected from an aluminum polycrystal sample demonstrating the SIFT keypoint identification and matching process. **A.** Stage neutral BSE image with keypoint identified by SIFT highlighted with colored circles. Unique edge-like shapes and grain intersections are targeted. **B.** Thirty degree tilted image of the same crystal highlighting the drastic contrast change that can occur due to electron channeling. A unique set of keypoints is

generated and highlighted for this image independently. **C.** Top ten matched keypoints using a brute-force search and the Lowe ratio test to unique match points of correspondence between the images. These points can then be used in combination with robust regression to estimate a homography matrix to transform all images onto the stage-neutral image.

After image alignment, differences in illumination due to geometric variation in detection efficiency are subtracted using a rolling ball filter with a large radius or local contrast equalization. Finally, the entire dataset can be segmented into grains by either directly clustering the orientation space data at each pixel or by summing the contrast over the entire aligned dataset and applying an edge detector. Each set of pixels corresponding to a common orientation is then summed to produce a high signal-to-noise ratio (SNR) pattern. In microscopes with dedicated back-scatter detector with high detector efficiency, it's likely that this summation step will be unnecessary as each pattern will have sufficient SNR for interpretation. As the actual angular resolution is determined by the divergence angle of the beam interacting with the specimen and the stage steps are considerably more coarse, quantifying the ultimate resolution is left to future work.
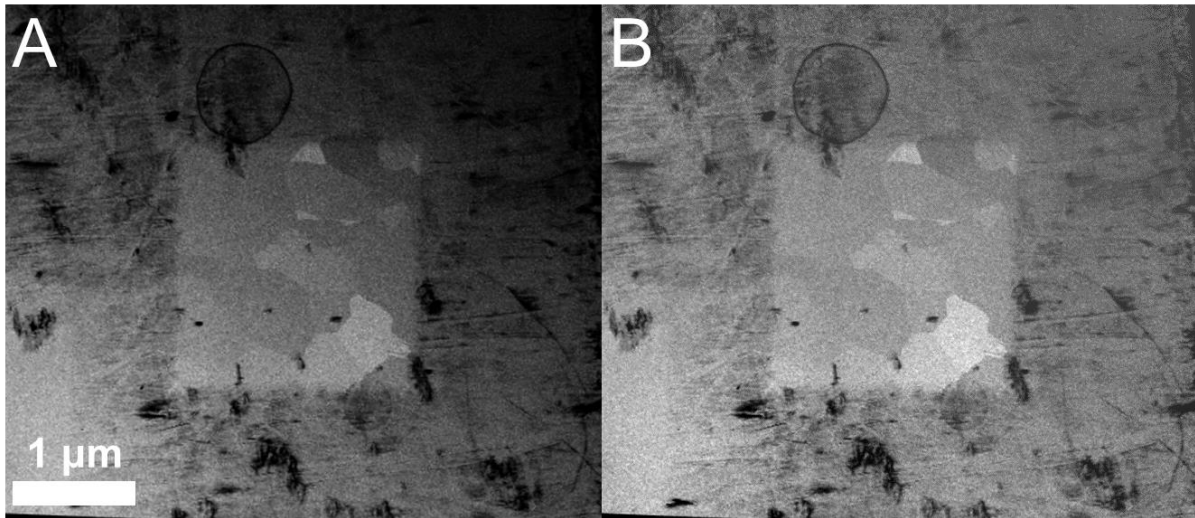
Figure 4.8 A. Raw BSE image collected from the TLD detector on FEI Nanolab from a PbSe-Gese polished specimen. Notice the large gradient in background intensity despite the flat surface due to positioning of the detector. Subtracting this artificial signal is critical in order to ensure that only contrast due to channeling is projected into the orientation space patterns. This background is tilt/rotation dependent and can therefore obscure the slight changes in contrast due to channeling. B. Same FOV after local contrast normalization with a large block-size to prevent removing contrast from within the grains. While not perfect, a large amount of the stray spatial signal is subtracted, allowing pixels to be subdivided and compared in orientation space.

EBSD analysis for reference was carried out on an FEI Quanta 650 FEG with an Oxford/HKL EBSD system. Maps were generated at 20 kV and EBSP collection was carried out at 5 kV to correspond more closely to the electron channeling data.

4.3.4 Dynamic Sampling

For each training experiment the algorithm under-samples the image, estimates the true image, and extracts features and utility estimates for each un-sampled pixel. A vector of coefficients then maps these features to a utility estimate, which is trained using many under-sampling conditions offline. These trained coefficients are used to iteratively predict the best measurement locations for the stage tilt/rotation commands for the crystal. To perform the simulation, each orientation map is divided into several sampling trajectories parameterized by tilt (φ) and rotation (θ). The algorithm makes a prediction and observes one pixel from the true image, from which it infers a future predicted "best" measurement. This proceeds until 10% of the total pixels have been measured. The dynamic sampling algorithm was implemented as described by Godaliyadda, et al [176]. Extending the single-objective dynamic sampling algorithm to multiple different mapping objectives (polycrystals) is trivial. Each grain is considered separately, and the total reduction in distortion for each point is taken as the mean reduction in distortion across all grains. For training data, a single ECP of Silicon (100) was used.

4.4 Results and Discussion

4.4.1 Single-Crystal Channeling Patterns

To construct an ECP by stage rocking, backscattered electron (BSE) images are acquired at a series of specified tilt (φ) and rotation (θ) positions as described in Figure 4.4b. These sample positions are relative to the sample surface normal and an arbitrary starting rotation position (typically registered to a relevant sample feature – in this case, the cleaved edge of the silicon wafer). A stage-rocking ECP can then be reconstructed by projecting the average contrast from each image onto a spherical surface as shown in Figure 4.5A for a single-crystal silicon (100) sample. This raw ECP clearly shows the Kikuchi-like bands indicating the nominal (100) sample orientation. These data are collected on a standard commercial instrument with the capability for both eucentric tilt and rotation. However, several compromises are made in order to produce these data on such an instrument. First, the through-the-lens detector (TLD) is operated in BSE mode without the immersion field due to the high tilt range required for data collection. The TLD operated in this condition has very low sensitivity, thus an electron beam current of 1.4 nA is required to achieve sufficient signal intensity. This high beam current and the short working distance for eucentric tilting result in a relatively large beam convergence angle, which likely limits the ultimate angular resolution for electron channeling in these experiments. Further, the high beam current and long data collection time result in surface contamination that produce the discontinuity in the ECP contrast in Figure 4.9A.
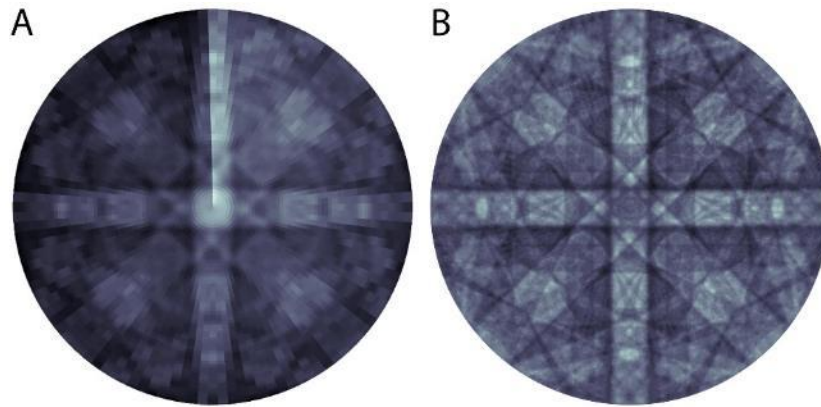
Figure 4.9 (A) Orthographic projection of a stage-rocked ECP reconstructed from the average contrast values in 7200 ECCIs at different orientations from a single-crystal silicon (100) sample. **(B)** Orthographic projection of a hybrid stage- and beam-rocked ECP reconstructed by binning each ECCI and correcting for beam divergence due to scanning. Corrections are also applied to adjust for systematic contrast variations (background subtraction and beam contamination correction).

Despite this, these issues can be ameliorated by a few key post-processing steps. First, a systematic background intensity distribution is removed in each image, which is presumably due to geometric factors influencing detection efficiency and is fixed for each instrument/sample stage combination. Second, beam divergence due to raster scanning is corrected, which lowers the angular resolution in the raw data. As the electron beam scans over the sample surface, its angle with respect to the

initial sample normal is modified by a divergence angle from the scan coils, parameterized by ψ_x and ψ_y. This divergence angle, and consequently the true sample-beam angle, depends on the beam position, working distance, and details of the specific electron-optical scanning system on the SEM. Thus, every pixel experiences a slightly modified angle as the scan coils tilt the beam to record a full rastered image, potentially improving the angular detail in the map. The actual details of the beam divergence during raster scanning is typically a trade secret for instrument manufacturers but can easily be determined by empirically varying an 'assumed' divergence and comparing the pattern quality. When the assumed divergence matches the divergence of the instrument used to collect the data the pattern will appear significantly clearer. This divergence value can then be used to correct future patterns collected off the same microscope. To accomplish this, each raw image is binned to 16×16 pixels, which are mapped to slightly shifted locations on the 3D orientation sphere according to the mean divergence angle for each region. This results in a 256-fold increase in the number of orientation values in the final data set – the optimal degree of binning is somewhat arbitrary and depends on collection conditions. Finally, sample contamination due to the high beam current is corrected by fitting a 3rd order polynomial according to the acquisition order. As the data after divergence correction overlap in some regions of the ECP, the final ECP is plotted using grid-cell averaging. By this method, the raw stage-rocked ECP (with 7200 orientation values) is expanded to a hybrid beam/stage-rocking ECP with more than 1.8 million orientation values as shown in Figure 4.9B. This results in a significant improvement in

the ECP angular resolution compared to the raw data, particularly visible at the higher tilt range where data are more sparsely acquired.

4.4.2 Polycrystalline Orientation Mapping

Next, consider the task of reconstructing ECPs and generating orientation maps for a polycrystalline sample. In such a sample, the crystal orientation can change abruptly at grain boundaries, leading to very different BSE yield between two potentially adjacent pixels. Therefore, it's crucial to ensure that pixels on either side of the boundary are correctly aligned over the course of thousands of images. For systems with many dozens of grains or where one wishes to study the change in orientation near an interface, this spatial correspondence between images becomes even more important. Briefly, contrast invariant points of correspondence are found using feature transforms. These points are then used to define a homography matrix, which accounts for the three-dimensional scaling/distortion that can occur as the object tilts around a eucentric point from a fixed perspective. This homography matrix is calculated and applied for each image in sequence, resulting in spatial correspondence through the ECCI BSE stack

To test this method, a polycrystalline PbSe-12%GeSe crystal was employed, a material family which has engendered much interest in the thermoelectric community[215]. Controlling microstructure and crystalline defects in these materials to reduce their thermal conductivity has

received much attention, as the thermoelectric figure of merit is inversely proportional to the thermal conductivity. A set of tilted and rotated BSE images was collected in the same fashion as for the silicon sample, with a maximum tilt angle of 35 degrees, a step size of 0.5 degrees, and a rotation step of 2 degrees. This resulted in 12,600 distinct BSE ECCI images, which were aligned and background corrected onto a common coordinate frame. ECPs were generated for each pixel in the aligned images as is standard practice in ECP or EBSD mapping. The patterns of each pixel contained in a grain were then integrated to form a very high contrast channeling pattern.
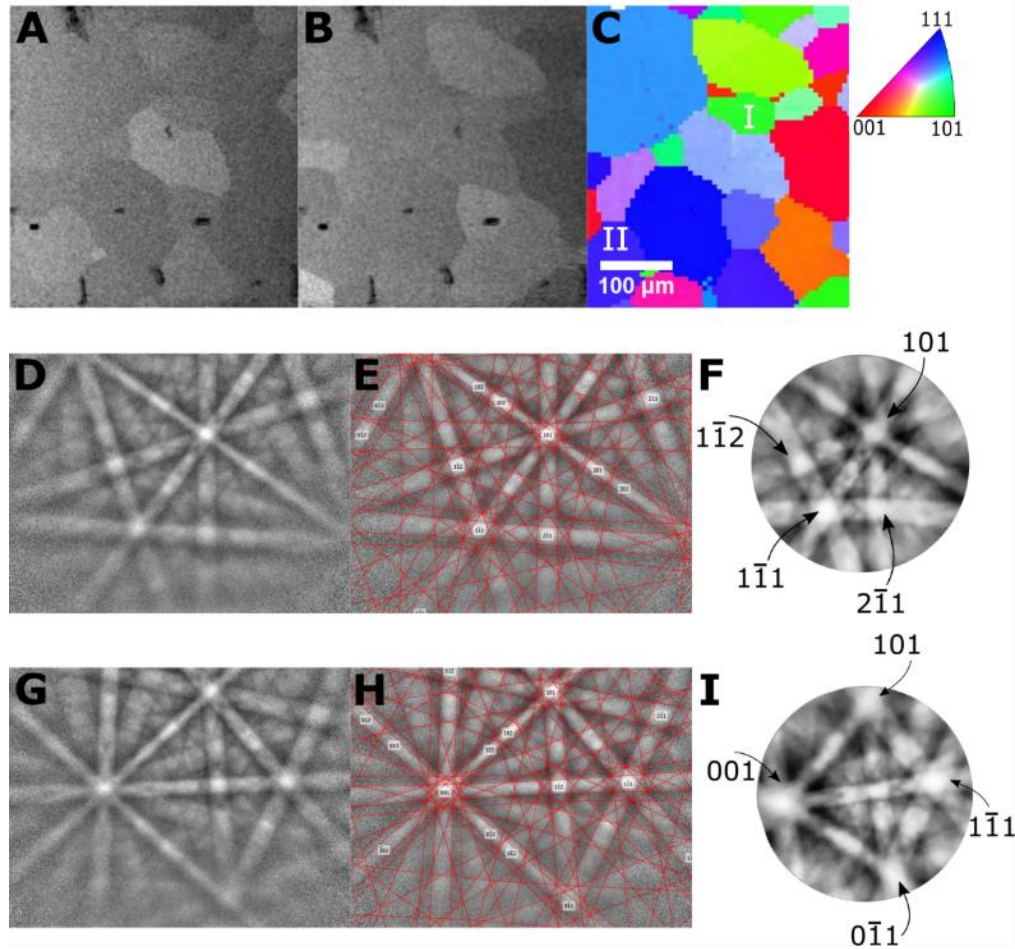
Figure 4.10 Comparison between conventional EBSD and OMEC ECPs on the same sample: (A-B) Aligned and perspective corrected BSE images of the same PbSe-GeSe crystal collected at two different orientations (A: 0 degree tilt, 0 degree rotation, B: 6 degree tilt and 0 degree rotation). (C) Z-axis-referenced inverse pole figure (IPFZ) map of the same area displaying the relative orientations of the member grains as indexed by EBSD. Grains I and II are labeled for the following two rows of the figure. (D-F) Representative EBSP, indexed pattern, and OMEC ECP from the

grain labeled I in the IPFZ map. (G-I) A second set of EBSP, indexed pattern, and OMEC ECP for the grain labeled II in the above IPFZ map. Strong agreement between the ECP and EBSP is seen. Note that to assist in identifying correlation between the EBSPs and the OMEC ECPs the ECPs have been projected stereographically (equiangular constructions).

Representative aligned BSE images from the total tilt series are displayed in Figure 4.10, along with an EBSD map collected from the same area. As can be seen in the two BSE images, different grains light up or fade according to the diffraction condition and the angle between the beam and crystal lattice. Orientation agreement between the electron backscatter patterns (EBSPs) and the OMEC ECPs can be seen in Figure 4.10, also showing the higher angular resolution and contrast inherent to channeling pattern imaging due to user control over the angular sampling with the tilt/rotation step size. The agreement between bands and their angles between the EBSPs and the ECPs is not surprising considering an *approximately* reciprocal mechanism[216] is responsible for generation of the signal in both imaging modalities. When indexing patterns, we are interested in the relative angles between bands, and the ability to project a true equiangular construction for the ECP enables simpler indexing as compared to indexing methods for EBSD, which must account for geometric distortion. Since the ECPs are intrinsically three-dimensional data, they can be projected in many different fashions to assist interpretation.
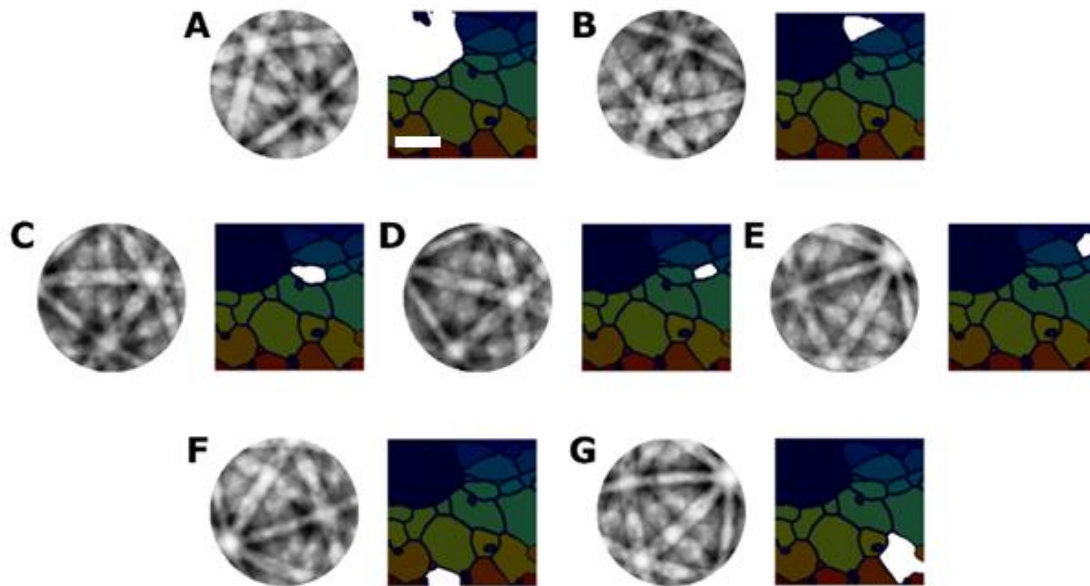
Figure 4.11 A set of orthographically projected channeling patterns for the grains displayed is shown. The true data for each grain is a real 3D dataset and thus has none of the distortion characteristic of EBSD. Thus, the data can be projected down to two dimensions in many ways depending on the purpose (stereographic for indexing, or orthographic for intuitive visualization). For small grains sufficient SNR is present to resolve many bands. In addition, the large field of view enabled by a stage-rocked channeling pattern means that every pattern has enough bands (>3) to enable an accurate indexing. Scale bar is 100 μm.

In this work pixels have only been grouped with common orientations into unique grains, but in principle arbitrary subsets of pixels down to the single pixel level can be also be analyzed depending on the length scale of a feature of interest (dislocations, strain, etc.). In addition, the same beam divergence correction for a single crystal sample could be applied here to further improve angular resolution. However, such a correction would be less effective for smaller grains at higher magnification and less uniform following spatial drift and distortion correction. In Figure 4.11 the segmented grain structure maps and several integrated ECPs for each grain is presented, where grain structures from the OMEC ECPs are identical to the segmentation performed using commercial software for EBSD maps. The spatial resolution in this system is limited by the stage accuracy and the ability to maintain a consistent FOV at high magnification. However, given a more precise stage and sufficient contrast (or fiducials) for image alignment, the OMEC ECP resolution should approach that of the BSE image.

As previously mentioned, stage-rocked electron channeling in OMEC allows for a higher angular field of view when compared to beam rocked channeling patterns (70 degrees in OMEC vs 5-10 degrees in beam-rocked ECPs). In fact, the technique should achieve a much higher angular range than demonstrated here, likely greater than 140 degrees given sufficient BSE signal. The large angular field of view allows OMEC ECPs to be directly indexed by traditional Hough-space band detection and triplet voting methods, since they generally have 4+ bands present in each pattern. This avoids the need for specialized indexing methods based on dynamical image simulations and dictionary pattern matching needed to accommodate the limited field of view in beam-rocked

ECPs. Also, no specialized distortion correction to account for the tilted gnomonic geometry of a standard EBSD pattern is necessary to correctly index the orientation. Since OMEC produces true three-dimensional orientation maps, the band angles can be compared directly in either stereographic projection, orthographic projection, or in three-dimensional space, potentially leading to more accurate indexing.

One limitation of OMEC is the low-throughput nature of imaging, since each mapping involves the recording of thousands of individual ECCI BSE images at different stage orientations. Although a higher sensitivity BSE detector could substantially reduce the total collection time, the sheer number of orientations that must be probed is a major complication. Certainly, data collected in this *brute force* manner is oversampled, as not every stage tilt/rotation contributes useful of orientation information. For example, space between the primary bands is effectively blank and is wasted sampling time. Ideally, a researcher would want to infer the tilts/rotations which contain information about major bands and their angles with respect to one another, since this is the primary information used for indexing a crystal's orientation. Fortunately, substantial progress has been reported on computationally efficient dynamic (adaptive) sampling methods[176, 217]. After each measurement, a crude estimation of the object's channeling pattern can be constructed, and areas of potentially useful content predicted from features of the crude pattern. Since bands have well defined patterns of contrast due to diffraction, it is not difficult to construct a library of typical features to train a supervised algorithm to make a prediction about the next best measurement.

Once trained, the algorithm can then construct crude estimates and make new predictions iteratively as it incorporates information obtained from the last measurement.
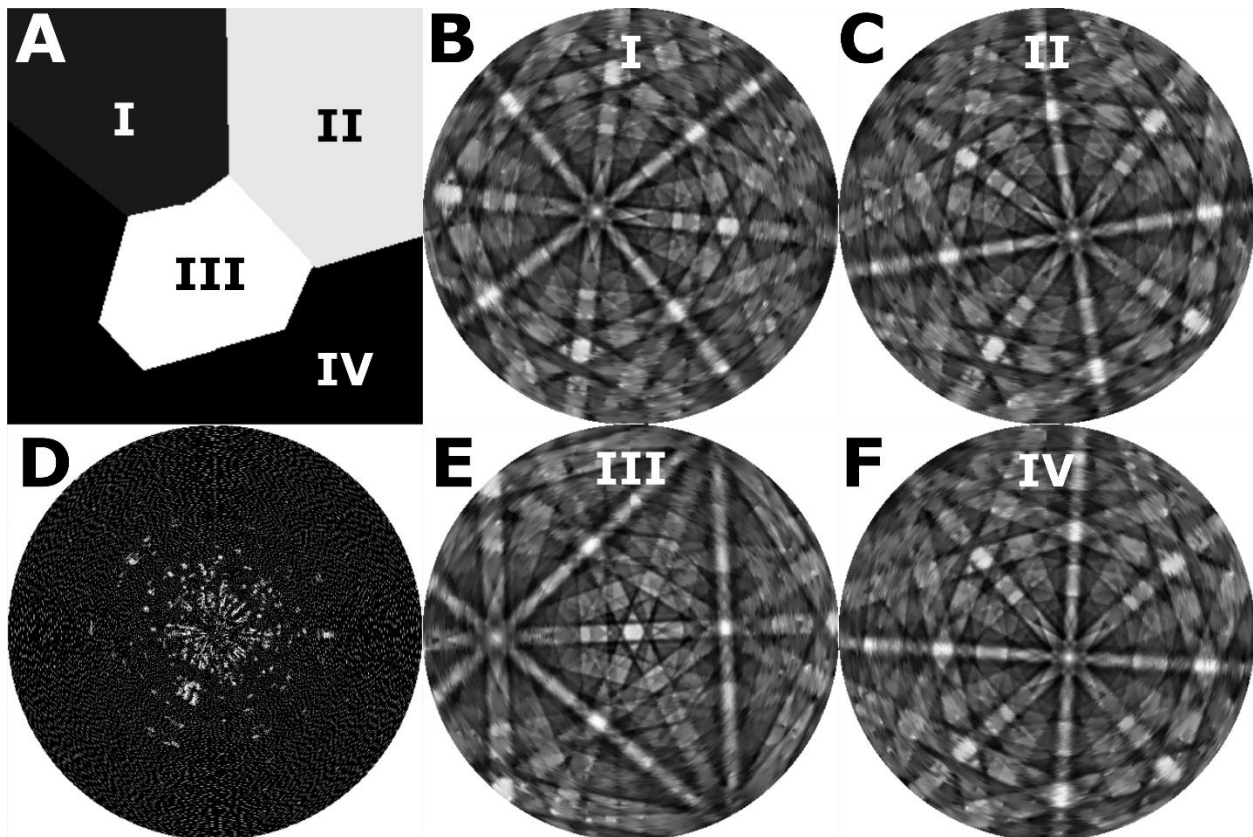
Figure 4.12 Simulated OMEC acquisition from calculated channeling patterns of Austenite. (A) Simulated BSE image at 0 degree tilt and 0 degree rotation for the four reconstructed orientations in (B),(C),(E),(F). When choosing which tilts/rotations to sample, the dynamic sampling approach chooses the point with the most benefit for all four grains simultaneously (multi-objective). (B,C,E,F) Reconstructed channeling patterns for four differently oriented Austenitic grains in a polycrystalline microstructure after sampling 10% of the possible tilts/rotations using dynamic

sampling. (D) Mask of selected tilts/rotations, white representing a sample position where a simulated BSE image was recorded, and black representing skipped.

Figure 4.12 shows a simulated example of how OMEC might benefit from using dynamic sampling. Using multi-beam electron simulations[216] a small four grain polycrystalline microstructure was simulated with several disparately oriented channeling patterns, parameterized by tilt (φ) and rotation (θ). After observing a measurement, the algorithm updates the estimation of the true pattern and proposes the next measurement which will have the largest positive effect on the pattern quality. At a sampling rate of only 10% for the simulated OMEC acquisition, the patterns are easily distinguishable, with many indexable bands well resolved. Particularly, prioritizing measurements on the edges of bands allows indexing to be performed very early on during the acquisition process, and balancing the acquisition of points between grains with differing orientation contrast is manageable A ~90% time savings for OMEC orientation mapping potentially brings the time to complete a map into the typical time range of an EBSD map.

Given the volume of data generated by a single OMEC experiment (thousands of spatially correlated ECCI BSE images), significant potential for data mining/engineering exists. For complicated specimens with multiple defects existing simultaneously, OMEC may facilitate disentanglement of multiple microstructural elements, since an ECCI has been collected at every possible orientation. Multiple two-beam-like conditions can be compared offline without the need

to identify an orientation on-the-fly using a correlative technique, as some defects may only be visible at specific orientations that would otherwise be missed. OMEC also certainly benefits from the potential of dynamic-sampling by prioritizing measurements at the intersection or edges of bands, thus oversampling the desirable information for ECCI analysis while 'synthesizing' the missing ECCIs based on redundant information (potentially taking advantage of both spatial and orientation space redundancies).

4.5   Summary & Conclusions

We have developed a new crystal orientation mapping method, OMEC, combining advantages of ECCI and SACP imaging, which enables orientation mapping over a large FOV with high angular range and distortion-free projection. The method has been demonstrated with up to seventy-degree angular imaging with micron-scale resolution, but much larger angular FOV and spatial resolution should be accessible with a more sensitive BSE detector and higher precision stage. In addition, this technique can be directly implemented on a commercial microscope (possessing adequate stage control) without any additional hardware. It is expected that difficulties due to the low-throughput nature of imaging may effectively be ameliorated by dynamic or "adaptive" stage control, where the collection of contrast-critical ECCIs is prioritized over orientations with relatively low contrast contribution to the channeling pattern. In addition, the large-data format and multiple interlinked contrast mechanisms characteristic of ECCIs may allow for the imaging

of multiple complicated defects simultaneously, opening the quantification of difficult to analyze specimens.

CHAPTER 5: FUTURE OUTLOOK AND CONCLUSIONS

5.1 Data mining large sets of OMEC patterns

As discussed earlier, EBSD can provide a turn-key technique to produce large scale orientation maps of samples. Electron channeling contrast images (ECCI) have also been used to investigate the nature of defect structures in surfaces non-destructively[218]. By tilting on and off two-beam conditions it becomes possible to solve for the Burgers vector of a dislocation given its visibility on certain orientations from the back scattered channeling contrast[219]. Conventionally, most people will identify the orientation of a certain region using EBSD. The sample will then be physically rotated back to the stage neutral position and tilted on to the Kikuchi line of interest using the EBSD pattern as a map. From this position, multiple backscattered ECCI images can be collected in order to understand the positioning of certain defects in the sample. This requires the user to have some intuition about which two-beam conditions are essential to understand a system of interest as well as a tool to accomplish the complex alignment between the EBSD scanning position and the stage neutral ECCI collections position[220].

In this implementation of OMEC, all of the available ECCI images in the accessible range of tilts and rotations from the stage neutral position are collected. Thus, in post-processing any desired

two-beam condition or ECCI image can be pulled out of the larger data set. This allows the user a much broader set of conditions with which explore defects that were not initially observable from the initial tilt rotation conditions. Instead of requiring the user to intuit the important conditions in which to collect ECCI images on a time-constrained and often expensive microscope, the user is allowed to explore the data naturally offline. For systems which have multiple complicated interrelated defect structures, this technique may allow for a more thorough understanding of their crystalline structure.

It may also be possible to leverage advances and statistical learning to automate the identification and understanding of defects structures in this extremely large data set. Since with high pixel densities (1024 or even 2048 pixel maps) it is possible for the total volume of data to exceed hundreds of gigabytes, it may quickly become impractical for an individual student or researcher to explore all possible ECCI conditions. Unsupervised learning techniques, such as clustering, may allow for the grouping of certain spatial locations by their behavior in orientation space. Already in this work we've made use of an extremely trivial clustering technique, K-means, which can effectively group different grains by their common orientations regardless of their spatial locations. More advanced clustering techniques which do not rely on manual setting of the number of clusters desired, such as Bayesian Dirichlet mixture models, may allow for the automatic identification and grouping of not only polycrystalline grain structures but also complex defect structures that may share a common Burgers vector[221].

Supervised learning techniques may also be trained to identify certain defects of interest in large data sets. Such techniques can leverage the structured nature of two-dimensional orientation maps and the three-dimensional spherical structure of the actual orientation patterns to achieve facile and high throughput identification of defects from the dense and high dimensional pattern spaces. In terms of process control and quality assurance, it may be of interest to industry where a particular set of certain maybe well-known defects creep in during certain processes and may be automatically examined and identified using an automatic method for substage and electron microscopy acquisition coupled with a supervised structured learning technique, such as a convolutional neural network.

5.2   Substage Collection

One of the major limiting factors this work on OMEC mapping of polycrystalline specimens was the need to use a through the lens detector (TLD) for the BSE electrons. Such detectors have extremely low collection efficiencies as compared to dedicated solid-state BSE detectors. This meant each pixel needed a very long dwell time to achieve a sufficient signal-to-noise ratio for a quality pattern. This detector was employed since the microscope equipped with a compucentric tilt/rotate stage was not equipped with a dedicated BSE detector. In principle, there's no reason

why a dedicated detector cannot be used to improve the collection efficiency and reduce the overall time to collect electron channeling maps should a suitable combination of scriptable compucentric stage and specific detector be available. However, an extremely precise substage can be placed within a commercial scanning electron microscope which is equipped with the necessary detector electronics. Commercially available substages have been produced for extremely precise ECCI, Transmission Kikuchi Diffraction (TKD), or volumetric imaging of specimens inside standard scanning electron microscopes[222]. This would considerably reduce the amount of time to collect full OMEC patterns by reducing the required dwell time.

In addition to saving time, a more sensitive detector would further increase the spatial and angular resolution by reducing the required beam current. Since the SNR was so poor on the instrument available, an extremely large probe current was needed to promote a sufficient number of BSE electrons. This resulted in a very large convergence angle which both increases the spatial spot size and 'blurs' the pattern in orientation space due to the simultaneous incidence of a wide array of angles.

By combining a dedicated substage with the reconstruction software, a complete product to produce stage rocked electron channeling patterns could be produced which would use the external command line into the commercial scanning electron microscope in place of an EDS controller to automate and coordinate the stage motion and electron beam scanning. This coordinated

movement could be controlled and automated by an external DAC controller with a standard programming language or through a graphical interface such as LabView. This is by no means an exceptionally complicated procedure as many third-party packages have been produced such as lithography systems like NPGS[223]. This would allow virtually any SEM to produce orientation maps of specimens at a considerably lower cost as compared to a full EBSD system.

This system would share many of the advantages of traditional selected area channeling patterns (SACP) and electron channeling contrast images (ECCI) such as sensitivity to superlattices and surface dislocations for understanding deformation transfer and fracture initiation. As compared to SACP, image and stage-optimized OMEC may actually be higher throughput, since the limited angular field of view in SACP means that a dedicated user must hand tune and collect multiple individual patterns which must be further stitched together to produce an interpretable map.

5.3   Unified Detector Sampling in STEM

One of the advantages of the multi objective dynamic sampling technique is the fact that it does not particularly care about the source of the spatially delineated signal. Earlier, MOADS was shown to be able to balance multiple mapping objectives, such as multiple EELS edges or multiple EDS Peaks (and potentially both EELS and EDS simultaneously). By sharing the information that

a particular point may contribute to multiple independent signals and maps, the technique was able to balance the application of electron dose and imaging time in order to produce a robust estimation of an arbitrary number of maps.

A key strength of scanning transmission electron microscopy is the bevy of signals which are available within the specimen chamber from the interaction and scattering (or lack thereof) between the specimen and incident beam. Two of these methods which focus on analytical mapping (EELS and EDS) have been highlighted, but other techniques such as pixelated STEM and even traditional annular or secondary imaging all contribute information regarding the local environment on the sample at a fixed beam position.

In principle, all of this information is constantly generated anytime the electron beam is incident on the sample, regardless of whether a detector is available to intercept it. Traditionally, only one detector is acquiring information from this volume of scattering events at any given time. This is because a user had to constantly evaluate the success rate of the experiment and interpret the results on-the-fly to maximize the amount of information generated for a given application of electron dose (dwell time and/or instrument time). However, this is a relatively inefficient way to sample information from the specimen, as often one technique or detector only provides a limited picture into all of the accessible information. Since the modular nature of dynamic sampling can easily accommodate fitting and interpreting other signals (spectral, image, or volumetric) and

parallelization has drastically reduced the penalty from adding additional objectives, it's possible that all of the available signals may be jointly optimized to maximize information from a specimen simultaneously. It's been shown in the previous chapter that signals which contribute relatively low informational content (low ERD) due to a flat or relatively easily approximately structure are 'filtered out' by the algorithm using the joint optimization approach. Therefore, sampling all signals simultaneously should not induce a penalty on the sampling performance and speed of the algorithm since it's expected that not all channels are useful for certain specimens (prioritization). A user rarely employs all techniques anyway, so there would be a benefit in reducing the chance of a missed 'useful' observation. The potential for a large volume of data by activating all detectors simultaneously is somewhat reduced by the order of magnitude reduction in the number of points required to sample. Thus, there seems to be little downside from employing all detectors simultaneously.

One reason MOADS was not employed other signals such as HAADF, SE, or the transmitted beam is that the time-scale of the measurement is much smaller than the time to process a single iteration. However, at extremely low beam currents, dwell times may quickly approach the computation time of a single iteration, making them accessible. There would be still no disadvantage from recording all signals which operate on a faster time scale than the slowest detector currently active.

More interestingly, since the majority of the signals emerging from the STEM share complementary information, it may be interesting to consider unifying their shared information into one abstract mapping objective directly. Since EELS and EDS maps are usually converted or quantified into atomic percent maps it would make more sense to optimize the quality of such a post-processed map rather than the individual quality of both maps separately. The modular nature of dynamic sampling would simply require an accurate forward/inverse model to convert the raw data coming from each detector into a unifiable parameter that can be expressed on a single map. Consider EELS, which has sensitivity for light elements, and EDS, which carries heavier elements, being directly interpreted into a shared atomic scale map which is then used to predict the optimal sampling pattern for atomic scale information. Other detectors, such as HAADF or SE, could be used to further optimize the sampling pattern by providing additional information where peaks are difficult to separate or edges may be obscured by other stronger nearby tails. Each additional detector or signal could then provide a slight informational edge and further improve the performance of the technique, while ensuring that no regions with useful texture will be ignored.

Converting from an image space with arbitrary units ('counts' for EELS and EDS) to a material specific space (atomic % or thickness) it may be possible to exploit prior information about material structure directly. In the image space it is much more difficult to express generalizable prior information without altering the types of images one would expect to generate. In the material space it may be much more practical to express powerful prior information, such as the range of

possible Atomic packing preferences, diffusion limitations, or a known series of surface configurations. Such prior information may allow for extremely low sampling rates that are superior to the low sampling rate generated by exploiting simple facts about image structure while still being computationally facile and computable in the time scale the measurements. These priors will have to be applied somewhat cautiously, as they may restrict the space of possible solutions in unexpected ways. Certainly in a research environment where the entire point is to study new phenomena not previously recorded, these priors may be more useful to 'screen out' uninteresting or well understood areas of the specimen.

Advances in computation, particularly the linking of servers and distributed computational nodes directly with microscope support computers in order to handle large volumes of data may also be used in a more dynamic fashion. Such clusters may directly interpret the information in a live format as it streams off the microscope and return requested coordinates and measurements directly back to electron scan coils. This may allow for more complicated fitting procedures or predictive models to be performed dynamically to achieve extremely low sampling rates at still reasonable time-scales.

The parallelization afforded by such nodes may also allow for the computation of much more complicated forward and inverse models for mapping raw signals to a material specific parameter. As discussed in the discussion section in chapter 4, the point-spread-function for EELS has

theoretically been suggested to extend beyond the region of primary energy deposition for some edges[173]. Since at any point a user has either an experimental spectrum or a predicted spectrum, the algorithm can predict both the expected information gain and the expected region of energy deposition. Thus, it can choose points which maximize the information while minimizing the overlap of deposited energy. This should directly mitigate damage associated with integrated dose in a direct way, instead of penalizing measurements in pixel space.

This will incorporate an explicit materials specific damage model which may be minimized while dually maximizing the quality of a particular map. For some materials, particularly hybrid soft/hard systems, multiple components of the structure have varying sensitivity to incident dose. Thus instead of minimizing the number of measurements required to maximize the quality of a map, MOADS will be able to balance the relative dose sensitivities of heterogeneous regions and exploit that to image materials in a stable fashion which were not analytically mappable previously.

5.4 Compressed Multi-Beam EDS

This thesis has been somewhat pessimistic about the application of compressive sensing to electron microscopy, however there are certainly areas in multi-beam scanning electron microscopy where it could be applied should the ability to blank individual beams become available. Briefly, in

multi-beam SEM multiple beams are created from a single primary beam, each of which scans the sample independently[224]. Strategically positioned detectors allow the collection of secondary or backscattered electrons independently from each beam position. Each beam then scans in parallel, producing a unique image over an area of a specimen. These images can then be stitched together to provide an extremely wide field of view at unprecedently low collection times, since measurements are made in parallel. Systems using dozens, and even approaching one hundred, individually addressable beams have been employed to rapidly accelerate wide field mapping of neuronal and other biological tissues.

The key enabling discovery was the configuration of charged gates and detectors which can pull off electrons from each beam-sample interaction area independently. However, there are many other signals and imaging modes in SEM for which it is impractical to develop a series of detectors which can discriminate between the different incident beams. As discussed in previous chapters, EDS allows for the wide area elemental mapping and has become a widely accepted, relatively 'turn-key' technique to understand compositional configurations at scale. However, it does suffer from relatively long dwell times due to limited detector cross sections and the need to operate at high currents to promote x-ray emission (from ionization events). The dynamic sampling technique discussed in Chapter 3 is one way to overcome this challenge by avoiding sampling redundant information. Using multiple beams would be an additional way to overcome this challenge and would potentially scale with the number of available beams, becoming a

considerably more effective method for wide field mapping. This would require specialized x-ray optics which could redirect the emitted x-rays from each individual beam position on to a separate detector, which would be completely impractical.

Instead, let's consider the addition of addressability to the incident electron beams themselves and use a single conventional EDS detector. This would likely require a fast electrostatic blanker which could blank individual beams without affecting the remaining (the practicality of which will be left to future work). A user will initially set up all the beam positions as normal and keep the scanning coils fixed such that the beams will be static. An automatic controller will then blank a random combination of beams and collect the emitted x-rays on to a single detector. Taking several of these acquisitions yields a set of spectra, the number of which is still much less than the total number of beams. Each beam will then step in unison to the next set of pixels and we'll integrate several random acquisitions. Thus, each set of fixed beam positions forms its own compressive sensing acquisition which can be solved individually. This inversion is well studied in the literature for other hyperspectral imaging techniques. The potential time-savings from performing a compressed acquisition aside, there is no practical way currently to perform EDS in a multi-beam SEM without turning off all but one beam.

5.5   Collaborative Hybrid User-Software Control

Many phenomena of interest which occur at high magnification occur in the sub micro-second time scale. As a result, relying on human reaction times, which barely reach into the milliseconds, to react to and identify processes using electron microscopes is unlikely to produce fruitful results. Some typical tasks required involve adjusting the beam shift in order to keep an object in the field of view, adjusting the focus to keep an object at a controlled defocus, or modifying the exposure conditions (dwell times, beam current, etc.) in order to maintain an appropriate signal-to-noise ratio. In principle, all these tasks could be classified as 'reactive' and are likely easily automatable using simple control algorithms. Instead of blindly collecting at the highest possible framerate and hoping that a particular reaction or phenomena was observed by manually sifting through terabytes of data off the microscope, such a system could prioritize the collection of the key frames of interest which would both reduce data management issues as well as the laborious hand sorting process post-collection. Already, simple metrics from image compression have been used to monitor the process of dendrite growth, and to identify quantitatively from a large dataset of images the onset of formation[225].

These are potentially no less reliable than an army of overcaffeinated students examining each frame by hand and may improve reproducibility by removing the chance for human bias. Operators are comfortable allowing software to tune higher order aberrations on state-of-the-art microscopes, since humans are often poor at tasks which require a high degree of attentiveness

over long periods of time. These tasks are ripe for the addition of computation in the operator decision loop.

Increasingly, electron microscopes are also being used as a fabrication tool, making use of the reducing power of the incident beam. Atom by atom manipulation has previously been attempted using laborious manual control of the beam position and incident current[226]. Next-generation methods make use of coupled algorithmic control of the scanning coils and incident current with a system that can monitor signals out of the microscope to directly fabricate rows of atomic positions in a crystal[227]. The fact that the microscope can be operated simultaneously as both a high-sensitivity imaging system and a fabrication tool means that the fabricated result can be monitored and adjusted on-the-fly using an imaging signal as 'feedback'. This is a major advantage over relatively 'blind' electron beam patterning techniques in the scanning electron microscope which must be extensively calibrated with dose arrays. This feedback assisted control has only included relatively basic measures, such as the 1D Fourier Transform of HAADF intensity, thus far[227]. However, when combined with pixelated STEM detectors, which in principle contain all of the scattering information from a specimen, much more fine control over atomic scale fabrication and manipulation may be possible. Although such images are difficult to interpret without simulating more palatable imaging modalities with artificial apertures, unsupervised learning techniques have previously been shown promise in understanding these large high dimensional datasets[228]. A coupled statistical learning technique to interpret pixelated STEM images with a feed-back control system to adjust the application of electron dose in response may

achieve facile and precise atomic scale patterning not currently possible through any other method without extensive manual control or calibration.

5.6   Concluding Comments

It's the goal of this thesis to highlight some of the incredible challenges and great opportunities facing the characterization of materials today. As our theoretical understanding and ability to computationally model phenomena inside the electron column improves, we are closer than ever to a true 'electron scattering experiment' model of the microscope. New phenomena enabled by improvements in hardware are being observed daily. However, to truly leverage these microscopes to understand materials and structure function relationships will require equal focus on the computational side. We are quickly moving from a world where we need to 'see' images to understand our samples, to one where the information coming off the microscope is abstract high dimensional 'data'. Software and theory will play the role of putting this information in context, as the volume of data is beyond the capability of a single expert to interpret. Removing the user an additional step from the microscope will be painful, but as users at high end facilities are increasingly forced out of the operating room, the opportunity to rethink the way data is collected will increasingly present itself to entrepreneurial researchers.

References:

1.   Androulakis, J.; Todorov, I.; He, J.; Chung, D. Y.; Dravid, V.; Kanatzidis, M., Thermoelectrics from abundant chemical elements: high-performance nanostructured PbSe-PbS. *J Am Chem Soc* **2011,** *133* (28), 10920-7.

2.   Ji, L.; Lin, Z.; Alcoutlabi, M.; Zhang, X., Recent developments in nanostructured anode materials for rechargeable lithium-ion batteries. *Energy & Environmental Science* **2011,** *4* (8), 18.

3.   Friedrich, H.; de Jongh, P. E.; Verkleij, A. J.; de Jong, K. P., Electron tomography for heterogeneous catalysts and related nanostructured materials. *Chemical reviews* **2009,** *109* (5), 1613-1629.

4.   Xin, H. L.; Mundy, J. A.; Liu, Z.; Cabezas, R.; Hovden, R.; Kourkoutis, L. F.; Zhang, J.; Subramanian, N. P.; Makharia, R.; Wagner, F. T.; Muller, D. A., Atomic-resolution spectroscopic imaging of ensembles of nanocatalyst particles across the life of a fuel cell. *Nano Lett* **2012,** *12* (1), 490-7.

5.   Horcajada, P.; Chalati, T.; Serre, C.; Gillet, B.; Sebrie, C.; Baati, T.; Eubank, J. F.; Heurtaux, D.; Clayette, P.; Kreuz, C. J. N. m., Porous metal–organic-framework nanoscale carriers as a potential platform for drug delivery and imaging. **2010,** *9* (2), 172.

6.   Chou, S. S.; De, M.; Luo, J.; Rotello, V. M.; Huang, J.; Dravid, V. P. J. J. o. t. A. C. S., Nanoscale graphene oxide (nGO) as artificial receptors: implications for biomolecular interactions and sensing. **2012,** *134* (40), 16725-16733.

7.   Williams, D. B.; Carter, C. B., *Transmission electron microscopy : a textbook for materials science*. 2nd ed.; Springer: New York, 2008.

8.   Wang, P.; Behan, G.; Kirkland, A. I.; Nellist, P. D.; Cosgriff, E. C.; D'Alfonso, A. J.; Morgan, A. J.; Allen, L. J.; Hashimoto, A.; Takeguchi, M.; Mitsuishi, K.; Shimojo, M., Bright-field scanning confocal electron microscopy using a double aberration-corrected transmission electron microscope. *Ultramicroscopy* **2011,** *111* (7), 877-86.

9.   Crewe, A. V. J. J. o. m., Scanning transmission electron microscopy. **1974,** *100* (3), 247-259.

10.   Batson, P. E.; Dellby, N.; Krivanek, O. L. J. N., Sub-ångstrom resolution using aberration corrected electron optics. **2002,** *418* (6898), 617.

11.   Weyland, M.; Midgley, P. A.; Thomas, J. M. J. T. J. o. P. C. B., Electron tomography of nanoparticle catalysts on porous supports: A new technique based on Rutherford scattering. **2001,** *105* (33), 7882-7886.

12.   Midgley, P.; Weyland, M. J. U., 3D electron microscopy in the physical sciences: the development of Z-contrast and EFTEM tomography. **2003,** *96* (3-4), 413-431.

13.   Egerton, R. F., *Electron energy-loss spectroscopy in the electron microscope*. Springer Science & Business Media: 2011.

14.   Cueva, P.; Hovden, R.; Mundy, J. A.; Xin, H. L.; Muller, D. A. J. M.; Microanalysis, Data processing for atomic resolution electron energy loss spectroscopy. **2012,** *18* (4), 667-675.

15.   Friel, J. J.; Lyman, C. E. J. M.; Microanalysis, Tutorial review: X-ray mapping in electron-beam instruments. **2006,** *12* (1), 2-25.

16.   Auger, P. J. C. A. S., Sur les rayons β secondaires produits dans un gaz par des rayons X. **1923,** *177*, 169.

17.   Chen, Z.; Weyland, M.; Sang, X.; Xu, W.; Dycus, J.; LeBeau, J.; d'Alfonso, A.; Allen, L.; Findlay, S. J. U., Quantitative atomic resolution elemental mapping via absolute-scale energy dispersive X-ray spectroscopy. **2016,** *168*, 7-16.

18.   Muller, D.; Kourkoutis, L. F.; Murfitt, M.; Song, J.; Hwang, H.; Silcox, J.; Dellby, N.; Krivanek, O. J. S., Atomic-scale chemical imaging of composition and bonding by aberration-corrected microscopy. **2008,** *319* (5866), 1073-1076.

19.   Li, W.; Wang, Z.; Deschler, F.; Gao, S.; Friend, R. H.; Cheetham, A. K. J. N. R. M., Chemically diverse and multifunctional hybrid organic–inorganic perovskites. **2017,** *2* (3), 16099.

20.   Gramm, F.; Baerlocher, C.; McCusker, L. B.; Warrender, S. J.; Wright, P. A.; Han, B.; Hong, S. B.; Liu, Z.; Ohsuna, T.; Terasaki, O. J. N., Complex zeolite structure solved by combining powder diffraction and electron microscopy. **2006,** *444* (7115), 79.

21.   Smit, B.; Maesen, T. L. J. C. r., Molecular simulations of zeolites: adsorption, diffusion, and shape selectivity. **2008,** *108* (10), 4125-4184.

22.	Myers, B. D.; Lin, Q.; O'Brien, M.; Mirkin, C. A.; Dravid, V. P. J. M.; Microanalysis, Temperature-Controlled Fluidic-Cell Scanning Electron Microscopy. **2016,** *22* (S3), 764-765.

23.	Kübel, C.; Voigt, A.; Schoenmakers, R.; Otten, M.; Su, D.; Lee, T.-C.; Carlsson, A.; Bradley, J. J. M.; Microanalysis, Recent advances in electron tomography: TEM and HAADF-STEM tomography for materials science and semiconductor applications. **2005,** *11* (5), 378-400.

24.	Sousa, A. A.; Azari, A. A.; Zhang, G.; Leapman, R. D. J. J. o. s. b., Dual-axis electron tomography of biological specimens: Extending the limits of specimen thickness with bright-field STEM imaging. **2011,** *174* (1), 107-114.

25.	Jinschek, J. R.; Batenburg, K. J.; Calderon, H. A.; Kilaas, R.; Radmilovic, V.; Kisielowski, C. J. U., 3-D reconstruction of the atomic positions in a simulated gold nanocrystal based on discrete tomography: Prospects of atomic resolution electron tomography. **2008,** *108* (6), 589-604.

26.	Midgley, P. A.; Dunin-Borkowski, R. E. J. N. m., Electron tomography and holography in materials science. **2009,** *8* (4), 271.

27.	Yakushevska, A.; Lebbink, M.; Geerts, W.; Spek, L.; Van Donselaar, E.; Jansen, K.; Humbel, B.; Post, J.; Verkleij, A.; Koster, A. J. J. o. s. b., STEM tomography in cell biology. **2007,** *159* (3), 381-391.

28.	Zheng, H.; Smith, R. K.; Jun, Y.-w.; Kisielowski, C.; Dahmen, U.; Alivisatos, A. P. J. S., Observation of single colloidal platinum nanocrystal growth trajectories. **2009,** *324* (5932), 1309-1312.

29.	Egerton, R.; Li, P.; Malac, M. J. M., Radiation damage in the TEM and SEM. **2004,** *35* (6), 399-409.

30.	Egerton, R. J. U., Choice of operating voltage for a transmission electron microscope. **2014,** *145*, 85-93.

31.	Henderson, R. J. Q. r. o. b., The potential and limitations of neutrons, electrons and X-rays for atomic resolution microscopy of unstained biological molecules. **1995,** *28* (2), 171-193.

32.	Thomas, A. J. A. C. I. E., Functional materials: from hard to soft porous frameworks. **2010,** *49* (45), 8328-8344.

33.	Čejka, J. J. A. C. I. E., Metal-Organic Frameworks. Applications from Catalysis to Gas Storage. Edited by David Farrusseng. **2012,** *51* (20), 4782-4783.

34.   Tsao, C.-S.; Yu, M.-S.; Wang, C.-Y.; Liao, P.-Y.; Chen, H.-L.; Jeng, U.-S.; Tzeng, Y.-R.; Chung, T.-Y.; Wu, H.-C. J. J. o. t. A. C. S., Nanostructure and hydrogen spillover of bridged metal-organic frameworks. **2009,** *131* (4), 1404-1406.

35.   Jones, M. R.; Seeman, N. C.; Mirkin, C. A. J. S., Programmable materials and the nature of the DNA bond. **2015,** *347* (6224), 1260901.

36.   Zhang, C.; Macfarlane, R. J.; Young, K. L.; Choi, C. H. J.; Hao, L.; Auyeung, E.; Liu, G.; Zhou, X.; Mirkin, C. A. J. N. m., A general approach to DNA-programmable atom equivalents. **2013,** *12* (8), 741.

37.   Lin, Q.-Y.; Li, Z.; Brown, K. A.; O'Brien, M. N.; Ross, M. B.; Zhou, Y.; Butun, S.; Chen, P.-C.; Schatz, G. C.; Dravid, V. P. J. N. l., Strong coupling between plasmonic gap modes and photonic lattice modes in DNA-assembled gold nanocube arrays. **2015,** *15* (7), 4699-4703.

38.   Ross, M. B.; Ku, J. C.; Vaccarezza, V. M.; Schatz, G. C.; Mirkin, C. A. J. N. n., Nanoscale form dictates mesoscale function in plasmonic DNA–nanoparticle superlattices. **2015,** *10* (5), 453.

39.   Koerner, H.; Drummy, L. F.; Benicewicz, B.; Li, Y.; Vaia, R. A. J. A. M. L., Nonisotropic self-organization of single-component hairy nanoparticle assemblies. **2013,** *2* (8), 670-676.

40.   Bacon, N.; Corbin, G.; Dellby, N.; Hrncirik, P.; Krivanek, O.; McManama-Smith, A.; Murfitt, M.; Szilagyi, Z. J. M.; Microanalysis, Nion UltraSTEM: an aberration-corrected STEM for imaging and analysis. **2005,** *11* (S02), 1422-1423.

41.   Cliffe, M. J.; Wan, W.; Zou, X.; Chater, P. A.; Kleppe, A. K.; Tucker, M. G.; Wilhelm, H.; Funnell, N. P.; Coudert, F.-X.; Goodwin, A. L. J. N. c., Correlated defect nanoregions in a metal–organic framework. **2014,** *5*, 4176.

42.   Nicolosi, V.; Chhowalla, M.; Kanatzidis, M. G.; Strano, M. S.; Coleman, J. N. J. S., Liquid exfoliation of layered materials. **2013,** *340* (6139), 1226419.

43.   Egerton, R. J. M.; Microanalysis, Beam-induced motion of adatoms in the transmission electron microscope. **2013,** *19* (2), 479-486.

44.   Bradley, C. *Calculations of atomic sputtering and displacement cross-sections in solid elements by electrons with energies from threshold to 1.5 MV*; Argonne National Lab.: 1988.

45.   McKinley Jr, W. A.; Feshbach, H. J. P. R., The Coulomb scattering of relativistic electrons by nuclei. **1948,** *74* (12), 1759.

46.   Glaeser, R. M. J. J. o. u. r., Limitations to significant information in biological electron microscopy as a result of radiation damage. **1971,** *36* (3-4), 466-482.

47.   Howie, A. J. R. d. P. A., Radiation damage problems in electron microscopy. **1980,** *15* (2), 291-295.

48.   Siegel, B. M.; Beaman, D. R., *Physical aspects of electron microscopy and microbeam analysis*. Wiley: 1975; Vol. 58.

49.   Rose, A., Television pickup tubes and the problem of vision. In *Advances in Electronics and electron Physics*, Elsevier: 1948; Vol. 1, pp 131-166.

50.   Cazaux, J. J. U., Correlations between ionization radiation damage and charging effects in transmission electron microscopy. **1995,** *60* (3), 411-425.

51.   Salisbury, I.; Timsit, R.; Berger, S.; Humphreys, C. J. A. P. L., Nanometer scale electron beam lithography in inorganic materials. **1984,** *45* (12), 1289-1291.

52.   Hayashida, M.; Kawasaki, T.; Kimura, Y.; Takai, Y. J. N. I.; Materials, M. i. P. R. S. B. B. I. w.; Atoms, Estimation of suitable condition for observing copper–phthalocyanine crystalline film by transmission electron microscopy. **2006,** *248* (2), 273-278.

53.   Egerton, R. J. M., RF Egerton, S. Lazar, and M. Libera, Micron 43, 2 (2012). **2012,** *43*, 2.

54.   Egerton, R. F. J. A. s.; imaging, c., Outrun radiation damage with electrons? **2015,** *1* (1), 5.

55.   Howells, M. R.; Beetz, T.; Chapman, H. N.; Cui, C.; Holton, J.; Jacobsen, C.; Kirz, J.; Lima, E.; Marchesini, S.; Miao, H. J. J. o. e. s.; phenomena, r., An assessment of the resolution limitation due to radiation-damage in x-ray diffraction microscopy. **2009,** *170* (1-3), 4-12.

56.   Bogner, A.; Jouneau, P.-H.; Thollet, G.; Basset, D.; Gauthier, C. J. M., A history of scanning electron microscopy developments: towards "wet-STEM" imaging. **2007,** *38* (4), 390-401.

57.   Scherzer, O. J. Z. f. P., Über einige fehler von elektronenlinsen. **1936,** *101* (9-10), 593-603.

58.   Hawkes, P. W.; Spence, J. C., *Science of microscopy*. Springer Science & Business Media: 2008.

59.   Erni, R., *Aberration-Corrected Imaging in Transmission Electron Microscopy: An Introduction Second Edition*. World Scientific Publishing Company: 2015.

60.   Rose, H. H. J. J. o. e. m., Historical aspects of aberration correction. **2009,** *58* (3), 77-85.

61.   Haider, M.; Uhlemann, S.; Schwan, E.; Rose, H.; Kabius, B.; Urban, K. J. N., Electron microscopy image enhanced. **1998,** *392* (6678), 768.

62.   Haider, M.; Rose, H.; Uhlemann, S.; Schwan, E.; Kabius, B.; Urban, K. J. U., A spherical-aberration-corrected 200 kV transmission electron microscope. **1998,** *75* (1), 53-60.

63.   Spence, J.; Zuo, J. J. R. o. s. i., Large dynamic range, parallel detection system for electron diffraction and imaging. **1988,** *59* (9), 2102-2105.

64.   Aikens, R.; Agard, D.; Sedat, J., Solid-state imagers for microscopy. In *Methods in cell biology*, Elsevier: 1988; Vol. 29, pp 291-313.

65.   Krivanek, O.; Mooney, P.; Fan, G.; Leber, M.; Sugimoto, Y. In *SLOW-SCAN CCD CAMERA FOR TRANSMISSION ELECTRON-MICROSCOPY*, Journal of Electron Microscopy, JAPANESE SOC ELECTRON MICRO BUS CENTER ACAD SOC JAPAN 16-9 HONKOMAGOME, 5-CHOME BUNKYO-KU, TOKYO 113, JAPAN: 1991; pp 290-290.

66.   Fan, G.; Ellisman, M. J. J. o. m., Digital imaging in transmission electron microscopy. **2000,** *200* (1), 1-13.

67.   Roberts, P.; Chapman, J.; MacLeod, A. J. U., A CCD-based image recording system for the CTEM. **1982,** *8* (4), 385-396.

68.   Faruqi, A.; Andrews, H. J. N. I.; Methods in Physics Research Section A: Accelerators, S., Detectors; Equipment, A., Cooled CCD camera with tapered fibre optics for electron microscopy. **1997,** *392* (1-3), 233-236.

69.   Faruqi, A.; Henderson, R.; Pryddetch, M.; Allport, P.; Evans, A. J. N. I.; Methods in Physics Research Section A: Accelerators, S., Detectors; Equipment, A., Direct single electron detection with a CMOS detector for electron microscopy. **2005,** *546* (1-2), 170-175.

70.   Ruskin, R. S.; Yu, Z.; Grigorieff, N. J. J. o. s. b., Quantitative characterization of electron detectors for transmission electron microscopy. **2013,** *184* (3), 385-393.

71.   Bai, X.-C.; McMullan, G.; Scheres, S. H. J. T. i. b. s., How cryo-EM is revolutionizing structural biology. **2015,** *40* (1), 49-57.

72.   Hart, J. L.; Lang, A. C.; Leff, A. C.; Longo, P.; Trevor, C.; Twesten, R. D.; Taheri, M. L. J. S. r., Direct detection electron energy-loss spectroscopy: a method to push the limits of resolution and sensitivity. **2017,** *7* (1), 8243.

73.   Krivanek, O. L.; Dellby, N.; Lovejoy, T. C.; Egerton, R. F.; Rez, P. J. M.; Microanalysis, Advances in Atomic-resolution and Molecular-detection EELS. **2017,** *23* (S1), 1028-1029.

74.   Williams, D. B.; Carter, C. B., The transmission electron microscope. In *Transmission electron microscopy*, Springer: 1996; pp 3-17.

75.   Tam, D. Facebook processes more than 500 TB of data daily. https://www.cnet.com/news/facebook-processes-more-than-500-tb-of-data-daily/#.

76.   Venkatakrishnan, S. V.; Bouman, C. A.; Wohlberg, B. In *Plug-and-play priors for model based reconstruction*, Global Conference on Signal and Information Processing (GlobalSIP), 2013 IEEE, IEEE: 2013; pp 945-948.

77.   Venkatakrishnan, S.; Drummy, L.; Jackson, M.; Bouman, C.; Simmons, J.; De Graef, M. J. U., A phantom-based forward projection approach in support of model-based iterative reconstructions for HAADF-STEM tomography. **2016,** *160*, 7-17.

78.   Venkatakrishnan, S. V.; Drummy, L. F.; De Graef, M.; Simmons, J. P.; Bouman, C. A. In *Model based iterative reconstruction for bright field electron tomography*, Computational Imaging XI, International Society for Optics and Photonics: 2013; p 86570A.

79.   Venkatakrishnan, S. V.; Hsiao, M.-S.; Garvin, N.; Jackson, M. A.; De Graef, M.; Simmons, J.; Bouman, C. A.; Drummy, L. F. J. M.; Microanalysis, Model-based Iterative Reconstruction for Low-dose Electron Tomography. **2014,** *20* (S3), 802-803.

80.   Sang, X.; LeBeau, J. M. J. U., Revolving scanning transmission electron microscopy: Correcting sample drift distortion without prior knowledge. **2014,** *138*, 28-35.

81.   Berkels, B.; Sharpley, R.; Binev, P.; Yankovich, A.; Shi, F.; Voyles, P.; Dahmen, W. J. M.; Microanalysis, High precision STEM imaging by non-rigid alignment and averaging of a series of short exposures. **2012,** *18* (S2), 300-301.

82.   Sreehari, S.; Venkatakrishnan, S.; Simmons, J.; Drummy, L.; Bouman, C. A. J. M.; Microanalysis, Library-Based Sparse Interpolation and Super-Resolution of S/TEM Images of Biological and Material Nano-Structures. **2016,** *22* (S3), 1446-1447.

83.   Sreehari, S. Advanced Prior Modeling for Nano-scale Imaging. Purdue University, 2017.

84.   Baraniuk, R. G. J. I. s. p. m., Compressive sensing [lecture notes]. **2007,** *24* (4), 118-121.

85.   Mamaghanian, H.; Khaled, N.; Atienza, D.; Vandergheynst, P. J. I. T. o. B. E., Compressed sensing for real-time energy-efficient ECG compression on wireless body sensor nodes. **2011,** *58* (9), 2456-2466.

86.   Jerri, A. J. J. P. o. t. I., The Shannon sampling theorem—Its various extensions and applications: A tutorial review. **1977,** *65* (11), 1565-1596.

87.   Foucart, S.; Rauhut, H., *A mathematical introduction to compressive sensing*. Birkhäuser Basel: 2013; Vol. 1.

88.   Candes, E. J.; Romberg, J. K.; Tao, T. J. C. o. P.; Sciences, A. M. A. J. I. b. t. C. I. o. M., Stable signal recovery from incomplete and inaccurate measurements. **2006,** *59* (8), 1207-1223.

89.   Candès, E. J.; Wakin, M. B. J. I. s. p. m., An introduction to compressive sampling. **2008,** *25* (2), 21-30.

90.   Candes, E.; Romberg, J. J. I. p., Sparsity and incoherence in compressive sampling. **2007,** *23* (3), 969.

91.   Chartrand, R.; Yin, W. *Iterative Reweighted Algorithms for Compressive Sensing*; 2008.

92.   Yin, W.; Osher, S.; Goldfarb, D.; Darbon, J. J. S. J. o. I. s., Bregman iterative algorithms for \ell_1-minimization with applications to compressed sensing. **2008,** *1* (1), 143-168.

93.   Ji, S.; Xue, Y.; Carin, L. J. I. T. o. S. P., Bayesian compressive sensing. **2008,** *56* (6), 2346.

94.   Candes, E. J. J. C. r. m., The restricted isometry property and its implications for compressed sensing. **2008,** *346* (9-10), 589-592.

95.   Chi, Y.; Scharf, L. L.; Pezeshki, A.; Calderbank, A. R. J. I. T. o. S. P., Sensitivity to basis mismatch in compressed sensing. **2011,** *59* (5), 2182-2195.

96.   Carin, L.; Liu, D.; Guo, B. J. I. A.; Magazine, P., Coherence, compressive sensing, and random sensor arrays. **2011,** *53* (4), 28-39.

97.   Candes, E. J.; Tao, T. J. I. t. o. i. t., Near-optimal signal recovery from random projections: Universal encoding strategies? **2006,** *52* (12), 5406-5425.

98.   Kashin, B. S. J. I. R. A. N. S. M., Diameters of some finite-dimensional sets and classes of smooth functions. **1977,** *41* (2), 334-351.

99.   Kashin, B. S.; Temlyakov, V. N. J. M. n., A remark on compressed sensing. **2007,** *82* (5-6), 748-755.

100.   Willett, R. M.; Marcia, R. F.; Nichols, J. M. J. O. E., Compressed sensing for practical optical imaging systems: a tutorial. **2011,** *50* (7), 072601.

101.   Choi, K.; Wang, J.; Zhu, L.; Suh, T. S.; Boyd, S.; Xing, L. J. M. p., Compressed sensing based cone-beam computed tomography reconstruction with a first-order method a. **2010,** *37* (9), 5113-5125.

102.   Lustig, M.; Donoho, D.; Pauly, J. M. J. M. R. i. M. A. O. J. o. t. I. S. f. M. R. i. M., Sparse MRI: The application of compressed sensing for rapid MR imaging. **2007,** *58* (6), 1182-1195.

103.   Binev, P.; Dahmen, W.; DeVore, R.; Lamby, P.; Savu, D.; Sharpley, R., Compressed sensing and electron microscopy. In *Modeling Nanoscale Imaging in Electron Microscopy*, Springer: 2012; pp 73-126.

104.   Reed, B. W., System and method for compressive scanning electron microscopy. Google Patents: 2015.

105.   Duarte, M. F.; Davenport, M. A.; Takhar, D.; Laska, J. N.; Sun, T.; Kelly, K. F.; Baraniuk, R. G. J. I. s. p. m., Single-pixel imaging via compressive sampling. **2008,** *25* (2), 83-91.

106.   Candes, E. J.; Eldar, Y. C.; Needell, D.; Randall, P. J. A.; Analysis, C. H., Compressed sensing with coherent and redundant dictionaries. **2011,** *31* (1), 59-73.

107.   Stevens, A.; Kovarik, L.; Abellan, P.; Yuan, X.; Carin, L.; Browning, N. D. J. A. S.; Imaging, C., Applying compressive sensing to TEM video: a substantial frame rate increase on any camera. **2015,** *1* (1), 10.

108. Stevens, A. J.; Kovarik, L.; Browning, N. D.; Liyu, A. V., Electron beam masks for compressive sensors. Google Patents: 2018.

109. d'Alfonso, A.; Freitag, B.; Klenov, D.; Allen, L., Atomic-resolution chemical mapping using energy-dispersive x-ray spectroscopy. *Physical Review B* **2010,** *81* (10), 100101.

110. Kimoto, K.; Asaka, T.; Nagai, T.; Saito, M.; Matsui, Y.; Ishizuka, K., Element-selective imaging of atomic columns in a crystal using STEM and EELS. *Nature* **2007,** *450* (7168).

111. de Jonge, N.; Ross, F. M., Electron microscopy of specimens in liquid. *Nature nanotechnology* **2011,** *6* (11), 695-704.

112. Kotakoski, J.; Jin, C.; Lehtinen, O.; Suenaga, K.; Krasheninnikov, A., Electron knock-on damage in hexagonal boron nitride monolayers. *Physical Review B* **2010,** *82* (11), 113404.

113. Talmon, Y., Transmission electron microscopy of complex fluids: the state of the art. *Berichte der Bunsengesellschaft für physikalische Chemie* **1996,** *100* (3), 364-372.

114. Teweldebrhan, D.; Balandin, A., Modification of graphene properties due to electron-beam irradiation. *Applied Physics Letters* **2009,** *94* (1), 013101.

115. Egerton, R.; Li, P.; Malac, M., Radiation damage in the TEM and SEM. *Micron* **2004,** *35* (6), 399-409.

116. Williams, J.; Elliman, R.; Brown, W.; Seidel, T., Dominant influence of beam-induced interface rearrangement on solid-phase epitaxial crystallization of amorphous silicon. *Physical review letters* **1985,** *55* (14), 1482.

117. Isaacson, M.; Johnson, D.; Crewe, A., Electron beam excitation and damage of biological molecules; its implications for specimen damage in electron microscopy. *Radiation research* **1973,** *55* (2), 205-224.

118. Glaeser, R. M.; Taylor, K. A., Radiation damage relative to transmission electron microscopy of biological specimens at low temperature: a review. *Journal of Microscopy* **1978,** *112* (1), 127-138.

119. Cosslett, V., Radiation damage in the high resolution electron microscopy of biological materials: A review*. *Journal of microscopy* **1978,** *113* (2), 113-129.

120.   Hofmann, S.; Sharma, R.; Ducati, C.; Du, G.; Mattevi, C.; Cepek, C.; Cantoro, M.; Pisana, S.; Parvez, A.; Cervantes-Sodi, F., In situ observations of catalyst dynamics during surface-bound carbon nanotube nucleation. *Nano letters* **2007,** *7* (3), 602-608.

121.   De Jonge, N.; Peckys, D. B.; Kremers, G.; Piston, D., Electron microscopy of whole cells in liquid with nanometer resolution. *Proceedings of the National Academy of Sciences* **2009,** *106* (7), 2159-2164.

122.   Yuk, J. M.; Park, J.; Ercius, P.; Kim, K.; Hellebusch, D. J.; Crommie, M. F.; Lee, J. Y.; Zettl, A.; Alivisatos, A. P., High-resolution EM of colloidal nanocrystal growth using graphene liquid cells. *Science* **2012,** *336* (6077), 61-64.

123.   Woehl, T. J.; Jungjohann, K. L.; Evans, J. E.; Arslan, I.; Ristenpart, W. D.; Browning, N. D., Experimental procedures to mitigate electron beam induced artifacts during in situ fluid imaging of nanomaterials. *Ultramicroscopy* **2013,** *127*, 53-63.

124.   Mohammadi-Gheidari, A.; Kruit, P. J. N. I.; Methods in Physics Research Section A: Accelerators, S., Detectors; Equipment, A., Electron optics of multi-beam scanning electron microscope. **2011,** *645* (1), 60-67.

125.   Anderson, H. S.; Ilic-Helms, J.; Rohrer, B.; Wheeler, J.; Larson, K. In *Sparse imaging for fast electron microscopy*, Computational Imaging XI, International Society for Optics and Photonics: 2013; p 86570C.

126.   Candès, E. J.; Romberg, J.; Tao, T., Robust uncertainty principles: Exact signal reconstruction from highly incomplete frequency information. *Information Theory, IEEE Transactions on* **2006,** *52* (2), 489-509.

127.   Donoho, D. L., Compressed sensing. *Information Theory, IEEE Transactions on* **2006,** *52* (4), 1289-1306.

128.   Baraniuk, R. G., Compressive sensing. *IEEE signal processing magazine* **2007,** *24* (4).

129.   Saghi, Z.; Benning, M.; Leary, R.; Macias-Montero, M.; Borras, A.; Midgley, P. A., Reduced-dose and high-speed acquisition strategies for multi-dimensional electron microscopy. *Advanced Structural and Chemical Imaging* **2015,** *1* (1), 1-10.

130.   Anderson, H. S.; Ilic-Helms, J.; Rohrer, B.; Wheeler, J.; Larson, K. In *Sparse imaging for fast electron microscopy*, IS&T/SPIE Electronic Imaging, International Society for Optics and Photonics: 2013; pp 86570C-86570C-12.

131.   Binev, P.; Dahmen, W.; DeVore, R.; Lamby, P.; Savu, D.; Sharpley, R., *Compressed sensing and electron microscopy*. Springer: 2012.

132.   Stevens, A.; Yang, H.; Carin, L.; Arslan, I.; Browning, N. D., The potential for Bayesian compressive sensing to significantly reduce electron dose in high-resolution STEM images. *Microscopy* **2014,** *63* (1), 41-51.

133.   Candes, E.; Romberg, J., Sparsity and incoherence in compressive sampling. *Inverse problems* **2007,** *23* (3), 969.

134.   Duarte, M. F.; Davenport, M. A.; Takhar, D.; Laska, J. N.; Sun, T.; Kelly, K. E.; Baraniuk, R. G., Single-pixel imaging via compressive sampling. *IEEE Signal Processing Magazine* **2008,** *25* (2), 83.

135.   Zhou, M.; Chen, H.; Ren, L.; Sapiro, G.; Carin, L.; Paisley, J. W. In *Non-parametric Bayesian dictionary learning for sparse image representations*, Advances in neural information processing systems, 2009; pp 2295-2303.

136.   Zhou, M.; Chen, H.; Paisley, J.; Ren, L.; Li, L.; Xing, Z.; Dunson, D.; Sapiro, G.; Carin, L., Nonparametric Bayesian dictionary learning for analysis of noisy and incomplete images. *Image Processing, IEEE Transactions on* **2012,** *21* (1), 130-144.

137.   Youngseon Lee, K. L., Kwangmin Lee, Jaeyong Lee, Jinwook Seo, Introduction to the Indian Buffet Process: Theory and Applications. *Korean Journal of Applied Statistics* **04/2015,** *28* (2), 17.

138.   Paisley, J.; Carin, L. In *Nonparametric factor analysis with beta process priors*, Proceedings of the 26th Annual International Conference on Machine Learning, ACM: 2009; pp 777-784.

139.   Griffiths, T. L.; Ghahramani, Z., The indian buffet process: An introduction and review. *The Journal of Machine Learning Research* **2011,** *12*, 1185-1224.

140.   Shen, H.; Li, X.; Zhang, L.; Tao, D.; Zeng, C., Compressed sensing-based inpainting of Aqua moderate resolution imaging spectroradiometer band 6 using adaptive spectrum-weighted sparse Bayesian dictionary learning. *Geoscience and Remote Sensing, IEEE Transactions on* **2014,** *52* (2), 894-906.

141.   Luttun, A.; Tjwa, M.; Moons, L.; Wu, Y.; Angelillo-Scherrer, A.; Liao, F.; Nagy, J. A.; Hooper, A.; Priller, J.; De Klerck, B., Revascularization of ischemic tissues by PlGF

treatment, and inhibition of tumor angiogenesis, arthritis and atherosclerosis by anti-Flt1. *Nature medicine* **2002,** *8* (8), 831-840.

142.   Li, W.-J.; Mauck, R. L.; Cooper, J. A.; Yuan, X.; Tuan, R. S., Engineering controllable anisotropy in electrospun biodegradable nanofibrous scaffolds for musculoskeletal tissue engineering. *Journal of biomechanics* **2007,** *40* (8), 1686-1693.

143.   Park, S. Y.; Lytton-Jean, A. K.; Lee, B.; Weigand, S.; Schatz, G. C.; Mirkin, C. A., DNA-programmable nanoparticle crystallization. *Nature* **2008,** *451* (7178), 553-556.

144.   Liu, Y.; Lin, X.-M.; Sun, Y.; Rajh, T., In situ visualization of self-assembly of charged gold nanoparticles. *Journal of the American Chemical Society* **2013,** *135* (10), 3764-3767.

145.   Shih, T. K.; Chang, R.-C.; Lu, L.-C.; Ko, W.-C.; Wang, C.-C. In *Adaptive digital image inpainting*, Advanced Information Networking and Applications, 2004. AINA 2004. 18th International Conference on, IEEE: 2004; pp 71-76.

146.   Stanciu, S. G.; Hristu, R.; Stanciu, G. A., Digital image inpainting and microscopy imaging. *Microscopy research and technique* **2011,** *74* (11), 1049-1057.

147.   Wang, Z.; Bovik, A. C.; Sheikh, H. R.; Simoncelli, E. P., Image quality assessment: from error visibility to structural similarity. *Image Processing, IEEE Transactions on* **2004,** *13* (4), 600-612.

148.   Boudaïffa, B.; Cloutier, P.; Hunting, D.; Huels, M. A.; Sanche, L., Resonant formation of DNA strand breaks by low-energy (3 to 20 eV) electrons. *Science* **2000,** *287* (5458), 1658-1660.

149.   Bursill, L.; Thomas, J.; Rao, K.-J., Stability of zeolites under electron irradiation and imaging of heavy cations in silicates. **1981**.

150.   Coates, I. A.; Smith, D. K., Hierarchical assembly—dynamic gel–nanoparticle hybrid soft materials based on biologically derived building blocks. *Journal of Materials Chemistry* **2010,** *20* (32), 6696-6702.

151.   Reed, B. W.; Park, S. T.; Masiel, D. J. J. M.; Microanalysis, Quantifying the advantages of compressive sensing and sparse reconstruction for scanning transmission electron microscopy. **2016,** *22* (S3), 286-287.

152.   Sanders, T.; Dwyer, C. J. M.; Microanalysis, Inpainting Versus Denoising for Dose Reduction in STEM. **2018,** *24* (S1), 482-483.

153.   Erni, R.; Rossell, M. D.; Kisielowski, C.; Dahmen, U., Atomic-resolution imaging with a sub-50-pm electron probe. *Physical review letters* **2009,** *102* (9), 096101.

154.   Chu, M.-W.; Liou, S.; Chang, C.-P.; Choa, F.-S.; Chen, C., Emergent chemical mapping at atomic-column resolution by energy-dispersive X-ray spectroscopy in an aberration-corrected electron microscope. *Physical review letters* **2010,** *104* (19), 196101.

155.   Kelly, D.; Lewis, E.; Downie, H.; Lloyd, J.; Zaluzec, N.; Burke, M.; Haigh, S., Energy Dispersive X-Ray Spectroscopy in Liquids: Inorganic and Biological Applications. *Microscopy and Microanalysis* **2016,** *22* (S5), 72-73.

156.   Holtz, M. E.; Yu, Y.; Gao, J.; Abruña, H. D.; Muller, D. A., In situ electron energy-loss spectroscopy in liquids. *Microscopy and Microanalysis* **2013,** *19* (4), 1027-1035.

157.   Wu, J.; Kim, A.; Bleher, R.; Myers, B.; Marvin, R.; Inada, H.; Nakamura, K.; Zhang, X.; Roth, E.; Li, S., Imaging and elemental mapping of biological specimens with a dual-EDS dedicated scanning transmission electron microscope. *Ultramicroscopy* **2013,** *128*, 24-31.

158.   Que, E. L.; Duncan, F. E.; Bayer, A. R.; Philips, S. J.; Roth, E. W.; Bleher, R.; Gleber, S. C.; Vogt, S.; Woodruff, T. K.; O'Halloran, T. V., Zinc sparks induce physiochemical changes in the egg zona pellucida that prevent polyspermy. *Integrative Biology* **2017,** *9* (2), 135-144.

159.   Muller, D. A., Structure and bonding at the atomic scale by scanning transmission electron microscopy. *Nature materials* **2009,** *8* (4), 263-270.

160.   Leapman, R.; Ornberg, R., Quantitative electron energy loss spectroscopy in biology. *Ultramicroscopy* **1988,** *24* (2-3), 251-268.

161.   Watanabe, M.; Ackland, D.; Burrows, A.; Kiely, C.; Williams, D.; Krivanek, O.; Dellby, N.; Murfitt, M.; Szilagyi, Z., Improvements in the X-ray analytical capabilities of a scanning transmission electron microscope by spherical-aberration correction. *Microscopy and Microanalysis* **2006,** *12* (6), 515-526.

162.   Hutchison, J. L.; Titchmarsh, J. M.; Cockayne, D. J.; Doole, R. C.; Hetherington, C. J.; Kirkland, A. I.; Sawada, H., A versatile double aberration-corrected, energy filtered HREM/STEM for materials science. *Ultramicroscopy* **2005,** *103* (1), 7-15.

163.   McDowell, M. T.; Ryu, I.; Lee, S. W.; Wang, C.; Nix, W. D.; Cui, Y., Studying the kinetics of crystalline silicon nanoparticle lithiation with in situ transmission electron microscopy. *Advanced Materials* **2012,** *24* (45), 6034-6041.

164. Luo, L.; Wu, J.; Luo, J.; Huang, J.; Dravid, V. P., Dynamics of electrochemical lithiation/delithiation of graphene-encapsulated silicon nanoparticles studied by in-situ TEM. *Scientific reports* **2014,** *4.*

165. Lustig, M.; Donoho, D. L.; Santos, J. M.; Pauly, J. M., Compressed sensing MRI. *IEEE signal processing magazine* **2008,** *25* (2), 72-82.

166. Choi, K.; Wang, J.; Zhu, L.; Suh, T. S.; Boyd, S.; Xing, L., Compressed sensing based cone-beam computed tomography reconstruction with a first-order method. *Medical physics* **2010,** *37* (9), 5113-5125.

167. Stevens, A.; Yang, H.; Carin, L.; Arslan, I.; Browning, N. D., The potential for Bayesian compressive sensing to significantly reduce electron dose in high-resolution STEM images. *Microscopy* **2013,** *63* (1), 41-51.

168. Sang, X.; Lupini, A. R.; Unocic, R. R.; Chi, M.; Borisevich, A. Y.; Kalinin, S. V.; Endeve, E.; Archibald, R. K.; Jesse, S. J. A. S.; Imaging, C., Dynamic scan control in STEM: Spiral scans. **2017,** *2* (1), 6.

169. Kovarik, L.; Stevens, A.; Liyu, A.; Browning, N. D., Implementing an accurate and rapid sparse sampling approach for low-dose atomic resolution STEM imaging. *Applied Physics Letters* **2016,** *109* (16), 164102.

170. Candes, E. J.; Romberg, J. K.; Tao, T., Stable signal recovery from incomplete and inaccurate measurements. *Communications on pure and applied mathematics* **2006,** *59* (8), 1207-1223.

171. Anderson, H. S.; Ilic-Helms, J.; Rohrer, B.; Wheeler, J. W.; Larson, K. W. In *Sparse imaging for fast electron microscopy*, Computational Imaging, 2013; p 86570C.

172. Béché, A.; Goris, B.; Freitag, B.; Verbeeck, J., Development of a fast electromagnetic beam blanker for compressed sensing in scanning transmission electron microscopy. *Applied Physics Letters* **2016,** *108* (9), 093103.

173. Egerton, R. J. M., Calculation, consequences and measurement of the point spread function for low-loss inelastic scattering. **2017,** *67* (suppl_1), i52-i59.

174. Godaliyadda, G. D.; Buzzard, G. T.; Bouman, C. A. In *A model-based framework for fast dynamic image sampling*, Acoustics, Speech and Signal Processing (ICASSP), 2014 IEEE International Conference on, IEEE: 2014; pp 1822-1826.

175.   Scarborough, N. M.; Godaliyadda, G. D. P.; Ye, D. H.; Kissick, D. J.; Zhang, S.; Newman, J. A.; Sheedlo, M. J.; Chowdhury, A. U.; Fischetti, R. F.; Das, C. J. J. o. s. r., Dynamic X-ray diffraction sampling for protein crystal positioning. **2017,** *24* (1), 188-195.

176.   Godaliyadda, G.; Ye, D. H.; Uchic, M. D.; Groeber, M. A.; Buzzard, G. T.; Bouman, C. A., A supervised learning approach for dynamic sampling. *Electronic Imaging* **2016,** *2016* (19), 1-8.

177.   Godaliyadda, G.; Ye, D. H.; Uchic, M. D.; Groeber, M. A.; Buzzard, G. T.; Bouman, C. A. J. a. p. a., A framework for dynamic image sampling based on supervised learning (slads). **2017**.

178.   Zhang, Y.; Godaliyadda, G. D.; Ferrier, N.; Gulsoy, E. B.; Bouman, C. A.; Phatak, C. J. U., Reduced electron exposure for energy-dispersive spectroscopy using dynamic sampling. **2018,** *184*, 90-97.

179.   de la Peña, F.; Ostasevicius, T.; Fauske, V. T.; Burdet, P.; Jokubauskas, P.; Nord, M.; Sarahan, M.; Prestat, E.; Johnstone, D. N.; Taillon, J. J. M.; Microanalysis, Electron microscopy (Big and Small) data analysis with the open source software package HyperSpy. **2017,** *23* (S1), 214-215.

180.   Banerjee, R.; Swaminathan, S.; Wheeler, R.; Fraser, H. L., Phase evolution during crystallization of sputter-deposited amorphous titanium–aluminium alloy thin films: Dimensional and solute effects. *Philosophical Magazine A* **2000,** *80* (8), 1715-1727.

181.   Parameswaran, S.; Deledalle, C.-A.; Denis, L.; Nguyen, T. Q. J. a. p. a., Accelerating GMM-based patch priors for image restoration: Three ingredients for a 100$\times $ speed-up. **2017**.

182.   Hujsak, K.; Myers, B. D.; Roth, E.; Li, Y.; Dravid, V. P., Suppressing Electron Exposure Artifacts: An Electron Scanning Paradigm with Bayesian Machine Learning. *Microscopy and Microanalysis* **2016,** *22* (4), 778-788.

183.   Venables, J. A.; Harland, C. J., Electron back-scattering patterns—A new technique for obtaining crystallographic information in the scanning electron microscope. *Philosophical Magazine* **1973,** *27* (5), 1193-1200.

184.   Schwarzer, R. A.; Hjelen, J. In *High-speed orientation microscopy with offline solving sequences of EBSD patterns*, Solid State Phenomena, Trans Tech Publ: 2010; pp 295-300.

185. Nolze, G., Image distortions in SEM and their influences on EBSD measurements. *Ultramicroscopy* **2007,** *107* (2), 172-183.

186. Chen, D.; Kuo, J.-C.; Wu, W.-T., Effect of microscopic parameters on EBSD spatial resolution. *Ultramicroscopy* **2011,** *111* (9), 1488-1494.

187. Wilkinson, A. J.; Meaden, G.; Dingley, D. J., High-resolution elastic strain measurement from electron backscatter diffraction patterns: new levels of sensitivity. *Ultramicroscopy* **2006,** *106* (4), 307-313.

188. Keller, R. R.; Geiss, R. H., Transmission EBSD from 10 nm domains in a scanning electron microscope. *Journal of Microscopy* **2012,** *245* (3), 245-251.

189. Isabell, T. C.; Dravid, V. P., Resolution and sensitivity of electron backscattered diffraction in a cold field emission gun SEM. *Ultramicroscopy* **1997,** *67* (1-4), 59-68.

190. Joy, D. C.; Newbury, D. E.; Davidson, D. L., Electron channeling patterns in the scanning electron microscope. *Journal of Applied Physics* **1982,** *53* (8), R81-R122.

191. Booker, G.; Shaw, A.; Whelan, M.; Hirsch, P., Some comments on the interpretation of the 'kikuchi-like reflection patterns' observed by scanning electron microscopy. *Philosophical magazine* **1967,** *16* (144), 1185-1191.

192. Van Essen, C.; Schulson, E.; Donaghay, R., Electron channelling patterns from small (10 μm) selected areas in the scanning electron microscope. *Nature* **1970,** *225* (5235), 847-848.

193. Kozubowski, J.; Gerberich, W.; Stefanski, T., Measurement of small elastic strains in silicon using electron channeling patterns. *Journal of Materials Research* **1988,** *3* (4), 710-713.

194. Wilkinson, A. J., Methods for determining elastic strains from electron backscatter diffraction and electron channelling patterns. *Materials Science and Technology* **1997,** *13* (1), 79-84.

195. Wilkinson, A. J.; Meaden, G.; Dingley, D. J., High resolution mapping of strains and rotations using electron backscatter diffraction. *Materials Science and Technology* **2006,** *22* (11), 1271-1278.

196. Guyon, J.; Mansour, H.; Gey, N.; Crimp, M. A.; Chalal, S.; Maloufi, N., Sub-micron resolution selected area electron channeling patterns. *Ultramicroscopy* **2015,** *149*, 34-44.

197.   Van Essen, C.; Schulson, E.; Donaghay, R., The generation and identification of SEM channelling patterns from 10 μm selected areas. *Journal of Materials Science* **1971,** *6* (3), 213-217.

198.   Lloyd, G. E.; Ferguson, C. C.; Law, R. D., Discriminatory petrofabric analysis of quartz rocks using SEM electron channelling. *Tectonophysics* **1987,** *135* (1-3), 243-249.

199.   Singh, S.; De Graef, M., Orientation sampling for dictionary-based diffraction pattern indexing methods. *Modelling and Simulation in Materials Science and Engineering* **2016,** *24* (8), 085013.

200.   DLUHOŠ, J.; SEDLÁČEK, L.; MAN, J. In *Application of electron channeling contrast imaging in study of polycrystalline materials and visualization of crystal lattice defects*, 21st International Conference on Metallurgy and Materials, 2012.

201.   Gutierrez-Urrutia, I.; Zaefferer, S.; Raabe, D., The effect of grain size and grain orientation on deformation twinning in a Fe–22wt.% Mn–0.6 wt.% C TWIP steel. *Materials Science and Engineering: A* **2010,** *527* (15), 3552-3560.

202.   Gutierrez-Urrutia, I.; Raabe, D., Dislocation density measurement by electron channeling contrast imaging in a scanning electron microscope. *Scripta Materialia* **2012,** *66* (6), 343-346.

203.   Trager-Cowan, C.; Sweeney, F.; Trimby, P.; Day, A.; Gholinia, A.; Schmidt, N.-H.; Parbrook, P.; Wilkinson, A.; Watson, I., Electron backscatter diffraction and electron channeling contrast imaging of tilt and dislocations in nitride thin films. *Physical Review B* **2007,** *75* (8), 085301.

204.   Koyama, M.; Akiyama, E.; Tsuzaki, K.; Raabe, D., Hydrogen-assisted failure in a twinning-induced plasticity steel studied under in situ hydrogen charging by electron channeling contrast imaging. *Acta Materialia* **2013,** *61* (12), 4607-4618.

205.   Zhang, J.-l.; Zaefferer, S.; Raabe, D., A study on the geometry of dislocation patterns in the surrounding of nanoindents in a TWIP steel using electron channeling contrast imaging and discrete dislocation dynamics simulations. *Materials Science and Engineering: A* **2015,** *636*, 231-242.

206.   Coates, D. G., Kikuchi-like reflection patterns obtained with the scanning electron microscope. *Philosophical Magazine* **1967,** *16* (144), 1179-1184.

207.   Brunner, M.; Erlewein, P. In *Large angle electron channeling patterns—generation and applications*, Proceedings of the 9th International Congress on Electron microscopy (Imperial, Toronto), 1978; pp 562-3.

208.   Langlois, C.; Douillard, T.; Yuan, H.; Blanchard, N. P.; Descamps-Mandine, A.; Van de Moortèle, B.; Rigotti, C.; Epicier, T., Crystal orientation mapping via ion channeling: An alternative to EBSD. *Ultramicroscopy* **2015,** *157*, 65-72.

209.   Veligura, V.; Hlawacek, G.; van Gastel, R.; Zandvliet, H. J. W.; Poelsema, B., Channeling in helium ion microscopy: Mapping of crystal orientation. *Beilstein Journal of Nanotechnology* **2012,** *3*, 501-506.

210.   Silk, J. R.; Dashwood, R. J.; Chater, R. J., Determination of lattice orientation in aluminium alloy grains by low energy gallium ion-channelling. *Nuclear Instruments and Methods in Physics Research Section B: Beam Interactions with Materials and Atoms* **2010,** *268* (11), 2064-2068.

211.   Daudin, B.; Rouviere, J.; Arlery, M., Polarity determination of GaN films by ion channeling and convergent beam electron diffraction. *Applied Physics Letters* **1996,** *69* (17), 2480-2482.

212.   Giannuzzi, L. A.; Michael, J. R., Comparison of Channeling Contrast between Ion and Electron Images. *Microscopy and Microanalysis* **2013,** *19* (2), 344-349.

213.   Lafond, C.; Douillard, T.; Cazottes, S.; Steyer, P.; Langlois, C., Electron CHanneling ORientation Determination (eCHORD): An original approach to crystalline orientation mapping. *Ultramicroscopy* **2018,** *186*, 146-149.

214.   Lowe, D. G. In *Object recognition from local scale-invariant features*, Computer vision, 1999. The proceedings of the seventh IEEE international conference on, Ieee: 1999; pp 1150-1157.

215.   Wang, H.; Pei, Y.; LaLonde, A. D.; Snyder, G. J., Heavily Doped p-Type PbSe with High Thermoelectric Performance: An Alternative for PbTe. *Advanced Materials* **2011,** *23* (11), 1366-1370.

216.   Winkelmann, A.; Trager-Cowan, C.; Sweeney, F.; Day, A. P.; Parbrook, P., Many-beam dynamical simulation of electron backscatter diffraction patterns. *Ultramicroscopy* **2007,** *107* (4), 414-421.

217.   Godaliyadda, G.; Ye, D. H.; Uchic, M. D.; Groeber, M. A.; Buzzard, G. T.; Bouman, C. A., A Framework for Dynamic Image Sampling Based on Supervised Learning (SLADS). *arXiv preprint arXiv:1703.04653* **2017**.

218.   Kamaladasa, R. J.; Jiang, W.; Picard, Y. N. J. J. o. e. m., Imaging dislocations in single-crystal SrTiO3 substrates by electron channeling. **2011,** *40* (11), 2222.

219.   Kamaladasa, R.; Picard, Y. J. M. s., technology, applications; education, Basic principles and application of electron channeling in a scanning electron microscope for dislocation analysis. **2010,** *3*, 1583-1590.

220.   Zaefferer, S.; Kleindiek, S.; Schock, K.; Volbert, B. J. M.; Microanalysis, Combined Application of EBSD and ECCI Using a Versatile 5-Axes Goniometer in an SEM. **2013,** *19* (S2), 1306-1307.

221.   Socher, R.; Maas, A.; Manning, C. In *Spectral chinese restaurant processes: Nonparametric clustering based on similarities*, Proceedings of the Fourteenth International Conference on Artificial Intelligence and Statistics, 2011; pp 698-706.

222.   Trimby, P. W. J. U., Orientation mapping of nanostructured materials using transmission Kikuchi diffraction in the scanning electron microscope. **2012,** *120*, 16-24.

223.   Nabity, J., JC Nabity Lithography Systems.

224.   Keller, A. L.; Zeidler, D.; Kemen, T. In *High throughput data acquisition with a multi-beam SEM*, Scanning Microscopies 2014, International Society for Optics and Photonics: 2014; p 92360B.

225.   Browning, N.; Mehdi, B.; Stevens, A.; Gehm, M.; Kovarik, L.; Jiang, N.; Mehta, H.; Liyu, A.; Reehl, S.; Stanfill, B. J. M.; Microanalysis, Using Sub-Sampling/Inpainting to Control the Kinetics and Observation Efficiency of Dynamic Processes in Liquids. **2018,** *24* (S1), 242-243.

226.   Susi, T.; Meyer, J. C.; Kotakoski, J. J. U., Manipulating low-dimensional materials down to the level of single atoms with electron irradiation. **2017,** *180*, 163-172.

227.   Dyck, O.; Kim, S.; Lupini, A. R.; Kalinin, S. V.; Jesse, S. J. M.; Microanalysis, Automated Atom-by-Atom Assembly of Structures in Graphene: The Rise of STEM for Atomic Scale Control. **2018,** *24* (S1), 1594-1595.

228.   Jesse, S.; Chi, M.; Borisevich, A. Y.; Belianinov, A.; Kalinin, S. V.; Endeve, E.; Archibald, R. K.; Symons, C. T.; Lupini, A. R. J. M.; Microanalysis, Using Multivariate Analysis of Scanning-Rochigram Data to Reveal Material Functionality. **2016,** *22* (S3), 292-293.

Karl Hujsak

Curriculum Vitae

☎ *(847) 467 2651*
✉ *khujsak@u.northwestern.edu*
🖥 *khujsak.github.io*

*Computational Electron Microscopy for the Characterization
of Soft, Hard, and Hybrid Materials*

Education

2013-2018   **Ph.D. Materials Science and Engineering**, *McCormick Schoool of Engineering*,
Northwestern University, Advisor: Vinayak P. Dravid.
Thesis: Multi-Dimensional Methods for Imaging Soft/Hard Hybrid Materials

2009–2013   **B.S. NanoEngineering**, *The University of California*, San Diego, *Cum Laude*.
Advisor: Ratneshwar Lal

Research and Scholarly Interests

- Novel methods for interrogating next-generation Nanoscale and Hybrid materials.
- Enabling faster and less damaging imaging with Machine Learning and AI.
- State-of-the-art tomography for 3D understanding of hierarchical Nanostructures

---

Publications

Karl Hujsak, Benjamin D Myers, Jann Grovogui, and Vinayak P Dravid. Stage-rocked electron channeling for crystal orientation mapping. *Scientific reports*, 8(1):5175, 2018.

Karl Hujsak, Eric W. Roth, William Kellogg, Yue Li, and Vinayak P. Dravid. High speed/low dose analytical electron microscopy with dynamic sampling. *Micron*, 108:31 – 40, 2018.

Karl Hujsak, Ming-Siao Hsiao, William Kellogg, Vinayak P. Dravid, and Lawrence F. Drummy. Volumetric characterization of hairy nanoparticle hybrid composites with electron tomography and model-based reconstructions. *Macro Letters*, Submitted, 2018.

Gajendra S Shekhawat, Srinivasan Ramachandran, Hossein Jiryaei Sharahi, Souravi Sarkar, **Karl Hujsak**, Yuan Li, Karl Hagglund, Seonghwan Kim, Gary Aden, Ami Chand, et al. Micromachined chip scale thermal sensor for thermal imaging. *ACS nano*, 12(2):1760–1767, 2018.

Doğa Gürsoy, Young P Hong, Kuan He, **Karl Hujsak**, Seunghwan Yoo, Si Chen, Yue Li, Mingyuan Ge, Lisa M Miller, Yong S Chu, et al. Rapid alignment of nanotomography data using joint iterative reconstruction and reprojection. *Scientific reports*, 7(1):11818, 2017.

Yue Li, Di Zhang, Ilker Capoglu, **Karl Hujsak**, Dhwanil Damania, Lusik Cherkezyan, Eric Roth, Reiner Bleher, Jinsong S Wu, Hariharan Subramanian, et al. Measuring the autocorrelation function of nanoscale three-dimensional density distribution in individual cells using scanning transmission electron microscopy, atomic force microscopy, and a new deconvolution algorithm. *Microscopy and Microanalysis*, pages 1–7, 2017.

Yue Li, Luay M Almassalha, John E Chandler, Xiang Zhou, Yolanda E Stypula-Cyrus, **Karl Hujsak**, Eric W Roth, Reiner Bleher, Hariharan Subramanian, Igal Szleifer, et al. The effects of chemical fixation on the cellular nanostructure. *Experimental Cell Research*, 2017.

Magdalena Owczarek, **Karl Hujsak**, Daniel P Ferris, Aleksandrs Prokofjevs, Irena Majerz, Przemysław Szklarz, Huacheng Zhang, Amy A Sarjeant, Charlotte L Stern, Ryszard Jakubas, et al. Flexible ferroelectric organic crystals. *Nature communications*, 7, 2016.

Karl Hujsak, Benjamin D Myers, Eric Roth, Yue Li, and Vinayak P Dravid. Suppressing electron exposure artifacts: An electron scanning paradigm with bayesian machine learning. *Microscopy and Microanalysis*, pages 1–11, 2016.

Wangqiang Sun, Sumit Kewalramani, **Karl Hujsak**, Heng Zhang, Michael J Bedzyk, Vinayak P Dravid, and C Shad Thaxton. Mesophase in a thiolate-containing diacyl phospholipid self-assembled monolayer. *Langmuir*, 31(10):3232–3241, 2015.

Presentations

2018 **High-Speed/Low-Dose Analytical Electron Microscopy with Machine Learning and MultiObjective Dynamic Sampling**, *Platform Presentation*, Microscopy and Microanlaysis, Cambridge Univ Press, Baltimore, MA.

2018 **Orientation Mapping by Electron Channeling (OMEC) and Hybrid Stage/Beam-Rocked Electron Channeling Patterns**, *Platform Presentation*, Microscopy and Microanlaysis, Cambridge Univ Press, Baltimore, MA.

2018 **Increasing the Speed of EELS/EDS Mapping through Dynamic/Adaptive Sampling Methodologies**, *Platform Presentation*, Microscopy and Microanlaysis, Cambridge Univ Press, Baltimore, MA.

2018 **Mapping Orientation of Polycrystals Using a Stage-Rocked Big Data Approach**, *Poster Presentation*, Microscopy and Microanlaysis, Cambridge Univ Press, Baltimore, MA.

2017 **Smart Acquisitions for High Speed Analytical Imaging**, *Invited Speaker*, ER-C Invited Speaker Series - Ernst Ruska-Centre, Forschungszentrum Jülich, DE.

2017 **Materials Microscopy Meets Machine Learning**, *Invited Speaker*, Integrated Imaging Initiative Seminar Series, Center for Nanoscale Materials, Argonne National Laboratory, Lemont IL.

2016 **Sparse Imaging for *In-Situ* and Tomographic Imaging of Soft and Hybrid Materials**, *Invited Speaker*, Summer Seminar Series, Air Force Research Laboratory, Wright Patterson Air Force Base, Dayton OH.

2016 **Suppressing Electron Exposure Artifacts: An Electron Scanning Paradigm with Bayesian Machine Learning**, *Poster Presentation*, Microscopy and Microanalysis, Cambridge Univ Press, 1-11 , Columbus, OH.

2016 **Self–Organizing Neural Networks: Parallels Between "Big Imaging" and Sparse Imaging in Electron Microscopy**, *Platform Presentation*, Microscopy and Microanalysis, Cambridge Univ Press, 22, 534-535, Columbus, OH.

2012 **Characterization of Nanografted DNA Motors For Drug Delivery Applications**, *Platform Presentation*, Biomedical Engineering Society, Atlanta GA.

Patents

2017 **Flexible Ferroelectric Crystals**, *Owczarek, Magdalena, Hujsak, Karl A., Ferris, Daniel P., Hong, Seungbum, Dravid, Vinayak P., and Stoddart, Fraser D.* , U.S. Patent Application No. 027170.

2017 **Method for acquiring intentionally limited data and the machine learning approach to reconstruct it.**, *Hujsak, Karl A., Vinayak P. Dravid, and Benjamin D. Myers.*, U.S. Patent Application No. 15/332,573.

Research Experience

2012–Present **Ph.D. Candidate**, *VPD Group*, Northwestern University.
Advisor: Vinayak P. Dravid

- Developed computational methods for utilizing and learning from large volumes of materials data
- Experience with image, volume, hyperspectral, and 4D diffraction data for higher through-put experiments
- Lead group collaboration with external colleagues at National Laboratories, Department of Defense (DoD) Labs, and international partners at Universität Basel, ETH Zürich, and Forschungszentrum Jülich

2016 **Summer Researcher**, *Materials and Manufacturing Directorate*, Air Force Research Laboratory, Dayton OH.
Supervisor: Lawrence F. Drummy

- Authored software suite connecting scientific instruments to scikit-learn and OpenCV for intelligent sampling
- Oversaw team compliance with DoD regulations and organized monthly staff meetings

Leadership and Teamwork Experience

2015-2018 Initiated 4 group collaborations with colleagues at National Laboratories, DoD Labs, and international partners at Universität Basel, ETH Zürich, and Forschungszentrum Jülich

2016-2018 Planned monthly teleconferences with program managers and yearly program reviews

2017-2018 Organized and directed 15 laboratory classes for undergraduates and graduates as a teaching assistant on Analytical Electron Microscopy

Awards

2018 Northwestern Library Open Access Research Award
2015 National Science Foundation Graduate Research Fellow
2014 National Institute for Cancer: Physical-Science Oncology Center Fellow